

DISSERTATION

FORCE SPECTROSCOPY AND DYNAMICS IN BIOLOGICAL SYSTEMS

Submitted by

Bryce William Schroder

Graduate Degree Program in Bioengineering

In partial fulfillment of the requirements

For the Degree of Doctor of Philosophy

Colorado State University

Fort Collins, Colorado

Spring 2019

Doctoral Committee:

Advisor: Diego Krapf

David Bark

Ketul Popat

Jennifer DeLuca

Copyright by Bryce William Schroder 2019

All Rights Reserved

## ABSTRACT

### FORCE SPECTROSCOPY AND DYNAMICS IN BIOLOGICAL SYSTEMS

Communication is key to any process involving the transmission of information or some sort of signal. For communication to occur, a signal must be created that can be detected. Cells communicate through cues transmitted in the forms of chemical and mechanical signals. The most fundamental means for transmitting chemical cues is through the process of diffusion. A single particle undergoing diffusion is considered to undergo Brownian motion, which can be modelled as a random walk. The random walk behavior is characteristic of both the particles properties and the fields in which it is occurring. An unbiased walk will be completely random without outside influence. A biased walk will be random within the confines of a potential influencing its direction. Both are Stochastic processes characterized through probabilistic models with known solutions. The work herein presents the development of single molecule experiments and the associated particle tracking tools targeting particles undergoing biased random walks within a trapping potential on or near a cellular membrane. In the first set of experiments, the trapping potential, an optical tweezers setup, has been developed and employed in measuring cellular membrane biophysical properties as well as blebbing forces. The optical trap was also used to directly measure flow driven forces in live embryonic zebrafish, the first known measurements of this kind. In the second set of experiments, synthetic lipid bilayers provided a trapping potential in a single dimension for protein binding

experiments leading to exchanges between free, 3-dimensional diffusion and bound, or biased, 2-dimensional diffusion. In all cases, stochastic models have been used in conjunction with image-based particle tracking tools to better characterize the biophysical properties and forces associated with the cellular membrane and its means of signal transduction. These measurements are key to understanding both the chemical and mechanical signaling means by which the cellular membrane transduces an external signal into an internal response.

## ACKNOWLEDGEMENTS

Completion of this degree is a great personal accomplishment; however, it has not come without help and is a testament to the program and my personal support system. A sincere thank you goes out to the School of Biomedical Engineering, its staff and educators for accepting me as a student, and students past and present for receiving me as your peer. It has been a longer process for myself than others, and I am grateful to everyone for their time and patience. Specifically, a big debt of gratitude goes to Diego, my advisor, for taking me into his lab, helping me complete a very important personal goal for my family's and my future, and standing with me throughout this degree's completion. Moreover, thank you to my committee for their continued support and guidance throughout an unfamiliar process.

To my peers that have worked along with me throughout this degree, specifically those that worked in Diego's lab, I truly appreciate the continued support and comradery. I will cherish my time working with every one of you as Diego has guided us along our personal and career paths. May we all aspire to the goal of happiness and success as we all move forward in our different directions.

To my family, my friends, and my overall support system. I have leaned on many of you in more ways than I have ever intended. Your support has not gone unnoticed, and I am sincerely grateful for each of you whom have been there in my struggles and my triumphs. Specifically, I address my family, and my children, whom mean the world to me. Your love and support have been a constant reminder of the

importance of this accomplishment. Thank you for being my unending inspiration and the reasons behind my success.

## DEDICATION

I hereby dedicate this to my children,  
Ava Marie, Kayla Evette, Anthony  
Richard, and Cora May.

## TABLE OF CONTENTS

<b>ABSTRACT .....</b>	<b>ii</b>
<b>ACKNOWLEDGEMENTS.....</b>	<b>iv</b>
<b>DEDICATION.....</b>	<b>vi</b>
<b>TABLE OF CONTENTS .....</b>	<b>vii</b>
<b>1. CHAPTER 1: INTRODUCTION &amp; BACKGROUND .....</b>	<b>9</b>
1.1. <i>Particles within Their Environments.....</i>	<i>12</i>
1.2. <i>Molecular Cell Biology Background.....</i>	<i>35</i>
1.3. <i>Microscopy Background .....</i>	<i>50</i>
1.4. <i>Image Based Single Particle Tracking.....</i>	<i>66</i>
<b>2. CHAPTER 2: MEMBRANE FORCE SPECTROSCOPY ON LIVING HELA CELLS .....</b>	<b>71</b>
2.1. <i>Introduction.....</i>	<i>71</i>
2.2. <i>Materials &amp; Methods.....</i>	<i>75</i>
2.3. <i>Results .....</i>	<i>91s</i>
2.4. <i>Discussion &amp; Conclusions .....</i>	<i>103</i>
<b>3. CHAPTER 3: FORCE SPECTROSCOPY IN THE BLOODSTREAM OF LIVE EMBRYONIC ZEBRAFISH .....</b>	<b>107</b>
3.1. <i>Introduction.....</i>	<i>107</i>
3.2. <i>Materials &amp; Methods.....</i>	<i>111</i>
3.3. <i>Results .....</i>	<i>120</i>
3.4. <i>Discussion &amp; Conclusions .....</i>	<i>129</i>
<b>4. CHAPTER 4: SUPERDIFFUSIVE MOTION OF MEMBRANE-TARGETING C2 DOMAINS.....</b>	<b>131</b>
4.1. <i>Introduction.....</i>	<i>131</i>
4.2. <i>Methods .....</i>	<i>135</i>
4.3. <i>Results .....</i>	<i>138</i>
4.4. <i>Discussion.....</i>	<i>147</i>
<b>5. CHAPTER 5: CONCLUSION.....</b>	<b>152</b>
<b>WORKS CITED .....</b>	<b>154</b>
<b>APPENDICES .....</b>	<b>187</b>
<b>APPENDICES A-1. PROTOCOLS.....</b>	<b>187</b>
<i>APPENDIX A-1.1 Polystyrene Bead Cleaning Protocol .....</i>	<i>188</i>

<i>APPENDIX A-1.2</i>	<i>Cell Freeze Down Procedure .....</i>	<i>190</i>
<i>APPENDIX A-1.3</i>	<i>Cell Planting/Passage Procedure.....</i>	<i>192</i>
<i>APPENDIX A-1.4</i>	<i>Chamber Preparation for Lipid Bilayers.....</i>	<i>194</i>
<i>APPENDIX A-1.5</i>	<i>Preparation of Coverslip Surfaces .....</i>	<i>197</i>
<i>APPENDIX A-1.6</i>	<i>Surface Preparation for HeLa Cell Culture.....</i>	<i>199</i>
<i>APPENDIX A-1.7</i>	<i>Laser Alignment Protocol.....</i>	<i>201</i>
<i>APPENDIX A-1.8</i>	<i>Tracking Algorithm &amp; Image Enhancement Protocol.....</i>	<i>204</i>
<i>APPENDIX A-1.9</i>	<i>Zebrafish Preparation Protocol.....</i>	<i>210</i>
<b>APPENDICES A-2.</b>	<b>SOFTWARE CODES.....</b>	<b>212</b>
<i>APPENDIX A-2.1</i>	<i>3D Tracking Subvi.....</i>	<i>213</i>
<i>APPENDIX A-2.2</i>	<i>2D Autocorrelation Function Subvi.....</i>	<i>215</i>
<i>APPENDIX A-2.3</i>	<i>Compare Z Profile Subvi.....</i>	<i>217</i>
<i>APPENDIX A-2.4</i>	<i>Get Max of Autocorrelation Function Subvi.....</i>	<i>218</i>
<i>APPENDIX A-2.5</i>	<i>Get Z Index Subvi .....</i>	<i>219</i>
<i>APPENDIX A-2.6</i>	<i>Hough Circle Detection Subvi.....</i>	<i>220</i>
<i>APPENDIX A-2.7</i>	<i>Get Radial Z Profile Subvi.....</i>	<i>222</i>
<i>APPENDIX A-2.8</i>	<i>Create ZLUT VI .....</i>	<i>224</i>
<i>APPENDIX A-2.9</i>	<i>Smoluchowski Plot Creator VI.....</i>	<i>226</i>
<i>APPENDIX A-2.10</i>	<i>ST Plot Creator VI .....</i>	<i>227</i>
<i>APPENDIX A-2.11</i>	<i>ST Plot Overlay Lines on Image Subvi.....</i>	<i>229</i>
<i>APPENDIX A-2.12</i>	<i>Registration in 1-Dimension M File .....</i>	<i>232</i>

## 1. CHAPTER 1: INTRODUCTION & BACKGROUND

---

Communication could be described as an exchange of signals with a means of understanding, filtering, and providing feedback that can be continuous, discrete, and/or intermittent within our everyday world. Without defined communication as just described, there would be no means of understanding this document and the underlying principles I intend to prescribe. Furthermore, a lack of understanding communication techniques or defined signals, does not mean that communication is not occurring. It means that the devices or mechanisms have not been defined to comprehend the signals that are being transferred. Thus, we have not developed the means for understanding and filtering out the message that is being communicated.

In our modern world, there are very few means of communication that we feel we do not understand, which is why roughly 7,100 languages exist as well as means to encrypt these languages.<sup>1</sup> There are, however, nonverbal signals and means of communication happening around us and within us that allow us to function and maintain life that occurs on a scale the naked eye cannot see and therefore we may be unaware. To those of us who understand the general sciences, such as biology, chemistry, and physics, this comes as no surprise. We have been trained to understand chemical and environmental exchanges that generate signals interpreted via tool development. To this end, we now know that certain species create pheromones related to attraction<sup>2</sup>, microorganisms swim in directions driven by chemical gradients (chemotaxis)<sup>3,4</sup>, and our voluntary movements are driven by nerve

impulses sent from our brains to our muscles.<sup>5</sup> In all these cases, chemical signals are transferred to some sort of mechanical response that drives the way living organisms communicate and function within their world. We also know that these chemical signals drive our development as we grow from single cellular to multicellular organisms with a very complex and well defined hierarchal arrangement.<sup>6,7</sup> Thus, the understanding of chemical signaling and communication has become key to understanding a variety of mechanisms tied to normal development and maintenance of homeostasis thereby preventing disease.

As scientists have worked towards this end, a variety of tools have been developed that have increased our understanding of signaling down to sub-microscopic levels. Key to this cognizance is the development of microscopic tools and techniques that have allowed us to visually and mechanically characterize the cellular and sub-cellular environments. Furthermore, the development of microscopic tools has driven the expansion of biological and chemical techniques that have further elucidated sub-cellular architecture, interactions, and mechanisms for response to environmental cues. We have learned that such cues need not be purely chemical, but that also physical stimulation, i.e. mechanical and/or light induced changes, can induce specific responses leading to changes in cellular architecture.<sup>8-12</sup> Specifically, the study of Green Fluorescent Protein (GFP) and understanding its genetic coding have enabled us to identify/engineer a variety of other fluorescent molecules that have been key to fluorescence microscopy techniques that have further elucidated cellular structures and protein based interactions.<sup>13,14</sup> Moreover, it has been realized

that these protein interactions can lead to a cascade of other signaling events leading ultimately to changes that effect genetic regulation and protein expression in response. Thus, the signal is communicated through a variety of complex interactions leading to changes that can directly affect the cell turning genes on and off that code for a multitude of responses good or bad.

Central to the cellular signaling response are two key principles that we continue to study: 1) the cellular membrane as a barrier and its signal transport mechanisms, and 2) how particles interact within the extracellular and intracellular environments to transfer the signal. These particles can be a variety of things, such as proteins, chemical molecules, or engineered beads we have introduced. Furthermore, we can modify these particles to enhance or suppress a certain interaction. For example, we can introduce a fluorescent tag, such as GFP, onto a protein via a variety of mechanisms and visually follow the fluorescent tag using single molecule techniques, hence providing visual information on how the protein moves.<sup>15</sup> We can also introduce a specific chemical that inhibits the particle's interactions with its environment. Thus, we can manipulate exchanges to understand the ultimate effect on the cell as channeled through the cellular membrane. This enables us to further expand on disease processes and methods to prevent or repair these events at the cellular level.

The work I present here centers on development of tools and techniques to measure the mechanical properties and events that occur on a cell within its environment, thereby effecting its overall signaling. Central to this theme is the

movement, or diffusion, of particles, either beads, whole cells, or individual proteins, within a defined trapping potential through optical microscopy techniques. In this first chapter, I will initially develop the principles related to particle movement and confinement within a trapping potential, which are dictated by thermal molecular interactions. I will then discuss the basics of molecular cell biology with the cell architecture highlighted around the cellular membrane. In conjunction, a discussion of cell types and organismal hierarchical arrangement will follow with the mechanisms being tied to blood vessel development, a key principle for the work discussed in Chapter 3. After providing this background, the basics of the microscopy tools we used in this work will be discussed. Finally, a discussion of image-based particle tracking techniques will follow, which will lay the framework for understanding the modifications made to these techniques to improve tracking and overall results obtained within our work.

## **1.1. PARTICLES WITHIN THEIR ENVIRONMENTS**

---

To understand particle interactions within their environments, we must return to the Laws of Physics and Thermodynamics to understand that these principles transfer from the macroscopic to the microscopic environment. Although I will not directly define these laws, everything that occurs within these environments follows them. For example, much like we expect a collision between two billiard balls to cause a transfer of energy from one ball to the other and a change in direction and therefore a change in momentum, we expect the same thing to occur on the molecular level. We expect each force to be met with an equal and opposite force, and a body in

motion will remain in motion until an outside force acts upon it like the friction of tires on the pavement of braking vehicle. More importantly, we expect conservation of energy and conservation of matter to apply within the system. Obviously, there is more to this interaction than is being defined here, but the central theme that needs to be understood while reading this is that there is a consistent balance that exists within the nature of the system. Nothing is created, nor destroyed, but it can be transferred or exchanged in some manner maintaining the overall universal balance within that system.

In this work, this balance is better defined as an energy balance that manifests itself through forces. Everything that is happening to a microscopic particle is happening due to energy transfer and a balance of forces within that environment. These forces, however, are not forces that can be directly seen or felt. In other words, the signal cannot be processed with simple sensory perception tools. Furthermore, the magnitude is so low for each molecular collision that we must recognize that there is a multitude of thermally dependent, random collisions occurring simultaneously resulting in visualized motion. We can indirectly see this through larger particle movements under a microscope. This motion that we see is random and defined by the temperature and the molecular composition of the system. In other words, particles will move a lot differently in hot water as opposed to cold maple syrup as opposed to a crystal lattice, an obvious assertion. Nonetheless, this observable movement within a substrate is known as diffusion, from the Latin *diffundere*, meaning to spread out.<sup>16</sup>

### ***1.1.1. DIFFUSION: A BRIEF HISTORICAL ACCOUNT***

---

As already discussed, diffusion briefly can be described as a random particle motion driven by temperature dependent molecular collisions and the composition of the system. This can be seen in a variety of systems from gas to liquid to even solid state with drastic slowing in the particle movement rates from gas to solid. Diffusion is the fundamental method of particle movements for transmission of signals that can occur within a cellular environment.<sup>17</sup> Moreover, it can occur on, in, or around a cell with drastic differences between those environments.<sup>18-24</sup> Thus, the ability to track particle movements can give us information on the signaling process as well as the environment in which it is occurring. Hence, the fundamentals of diffusion are discussed here within a brief historical framework.

As the primary focus of this work occurs within the liquid state, it is rather fitting that this random motion was first described by a Scottish botanist, Robert Brown, through his study of pollen grains in water in 1827.<sup>25</sup> He found that the microscopic granules contained within the pollen would follow an incessant, random motion, now termed Brownian motion for his discovery. This random walk as we now describe it, however, was not recognized as a diffusion process, nor did it provide a physical understanding of the molecular processes that lead to the motion.

It was not until the work of Adolf Fick that diffusion began to have a mathematical framework and stronger understanding. Working off the studies initiated by Thomas Graham on the inter-dispersion of salt solutions<sup>26</sup>, an extension of his previous work with gaseous species, Fick applied similar principles to Graham's

data that Fourier and Ohm had used to describe thermal and electrical conductance, respectively. Using these methods, he obtained models for molecular diffusion.<sup>27</sup>

Fick postulated that the number of molecules diffusing across a certain point during a finite amount of time, or the flux, was directly proportionate to the concentration gradient. This has come to be known as Fick's first law:

$$j = -D \frac{\partial c}{\partial x} \quad (1.1)$$

where,  $j$  is particle flux,  $D$  is the diffusion coefficient,  $c$  is concentration, and  $x$  is relative distance. He also correctly asserted that the diffusion coefficient ( $D$ ) was "a constant dependent upon the nature of the substance".<sup>27-29</sup> Taking this a step further, Fick used conservation of matter to assert that the change in flux ( $j$ ) relative to distance ( $x$ ) was proportional to the change in concentration ( $c$ ) with respect to time ( $t$ ), otherwise known as the continuity equation.

$$\frac{\partial j}{\partial x} = -\frac{\partial c}{\partial t} \quad (1.2)$$

This is a key assertion that when combined with 1.1 gives us Fick's second law, or the diffusion equation:

$$\frac{\partial c}{\partial t} = D \frac{\partial^2 c}{\partial x^2} \quad (1.3)$$

This gives us a relation that tells us the change in particle number over time across a certain point is related to the gradient concentration driving force and the resistance to this force by the solution reflected in the diffusion coefficient. It mathematically defined the phenomenon of diffusion, or the transport of particles like the transport of heat but failed to give us an understanding of why diffusion occurs.

Furthermore, there was no reconciliation of Brownian motion as a diffusion-based process.

Many period physicists and scientists alike continued the study of Brownian motion. The work of Georges Guoy provided interesting insight when he found the motion to be independent of any external forces. Temperature and viscosity of the fluid, however, had drastic effects on the particles' movement. This lead him to correctly hypothesize that Brownian motion was "a weakened and remote testimony of thermal molecular motions."<sup>16,29,30</sup>As molecular/atomic theory was a rather new subject, this was a key observation supporting it. Yet, the understanding of Brownian motion from an atomic theory standpoint had lacked in reconciliation with Fick's laws. Thus, it was not known that Brownian motion was a diffusion-based process. This was primarily due to those working on this area were looking at Brownian motion using kinetic theory and a focus on particle velocities, which gave erratic results over the path lengths observable within a microscope at the time.<sup>16</sup> This makes sense, as the motion is erratic, non-continuous, and immeasurable over extremely short time periods that might reflect the appropriate particle velocities based on kinetic theory.

Spurred by the work of their predecessors, Albert Einstein and Marion Smoluchowski reconciled Brownian motion with diffusion and atomic theory using thermodynamics and molecular kinetics, respectively.<sup>16</sup> Independently, Einstein and Smoluchowski each treated Brownian motion as a random walk laying the framework for how we mathematically define free, unbiased particle movements today. Within

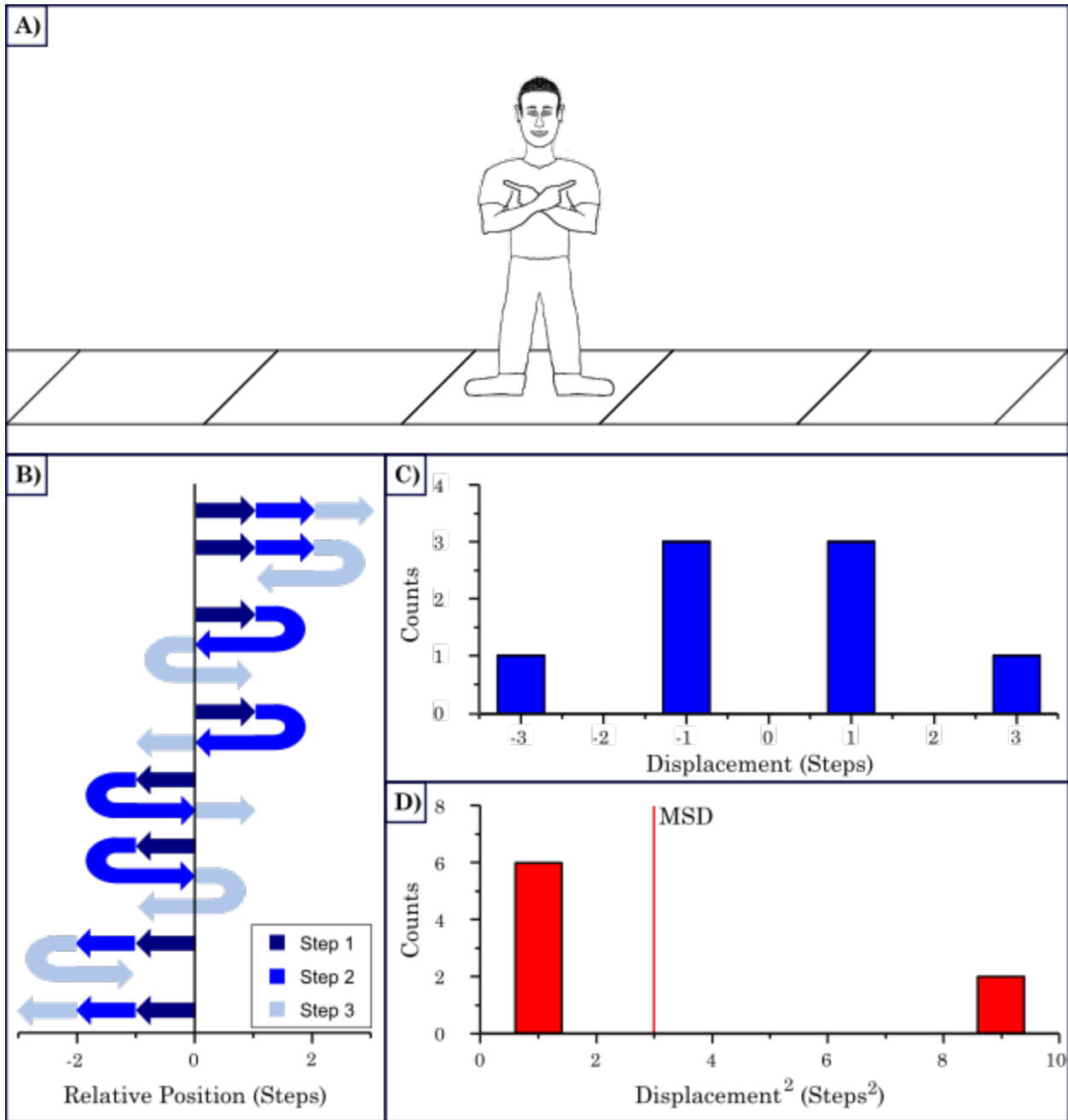


Figure 1.1 A) One dimensional random walk represented by a man on a sidewalk with an unbiased choice to move either direction. B) Illustration of possible paths with ending points on a three-step random walk. C) Distribution of displacements after three steps illustrating the lack of movement of the overall ensemble of steps. D) Distribution of squared displacements illustrating the positive displacement of the ensemble's mean squared displacements.

an unbiased random walk, a particle's movement is only dependent on its initial position and the probability that it will move to another position from that point. When truly unbiased, i.e. no drift or external forces, the probability of a step in any

direction is equal. One dimensionally, this can be represented as a man standing on sidewalk with the ability to move either left or right into the next square (Fig. 1.1A). Each step the man takes is of equal length ( $l$ ) within a defined constant time period ( $\tau$ ). His initial position ( $x_0$ ) determines where he can take his next step. The probability of taking his next step is unbiased towards either direction. Therefore, the probability of moving left or right is equal. Thus, after a single step ( $s$ ), the walker will be located at  $\pm l$ . From that position, the walker can make another unbiased step in either direction, hence continuing his movement either back to the initial position or further to a position at  $\pm 2l$ . The number of steps ( $n$ ) therefore determines how many potential locations the walker could end up. In the case of 2 steps, there are  $2^n$  possibilities, or 4 potential outcomes: two steps left, a step left and a step right, a step right and a step left, or two steps right. In terms of deviation from the initial position, this would be represented as  $-2l$ ,  $0$ ,  $0$ , and  $2l$ , respectively. Thus, there is a higher probability that he will end up back at the center than at either extreme, regardless of the path, or trajectory, the walker takes.

Mathematically, we can define the walker's ending position after  $n$  steps as a sum of each discrete step within the walk:

$$x_n = \sum_{i=1}^n s_i \tag{1.4}$$

Let's assume, however that there are multiple walkers, or an ensemble, each representing a possible path taken. Like described above, there are  $2^n$  possibilities of where each walker can end up. Assuming there were three steps taken on differing paths, there are eight possible paths (Fig. 1.1B). We can look at each path individually

and create a distribution of their potential end positions as seen in Fig. 1.1C. Thus, a statistical representation of position based on the number of steps and possible paths was created. We can therefore look at their average displacement  $\langle x_n \rangle$  and find:

$$\langle x_3 \rangle = \left\langle \sum_{i=1}^3 s_i \right\rangle = \sum_{i=1}^3 \langle s_i \rangle = \frac{-3l + 3(-l) + 3(l) + 3l}{8} = 0 \quad (1.5)$$

As an ensemble, there was no net movement from the initial position, although each individual walker provided a different trajectory with a resulting position. Regardless of the number of steps, this result will always be mathematically the same for an unbiased random walk ( $\langle x_n \rangle = 0$ ).

Although the distribution results statistically in no net movement, we know in the case described that each walker ended up in a different location than where they initially started. There was a net displacement of each walker, however the negative steps are equally as probably as the positive steps and therefore cancel each other out when looking at the distribution. If, however, we square the net displacement of each walker, we no longer have negative displacements to cancel out the positive displacements. Thus, the distribution is no longer centered about the initial position (Fig. 1.1D). The mean of the distribution is no longer zero. This is known as the mean squared displacement (MSD), and mathematically, the three-step distribution is represented by:

$$\langle x_3^2 \rangle = \left\langle \left( \sum_{i=1}^3 s_i \right)^2 \right\rangle = \sum_{i=1}^3 \langle s_i^2 \rangle = \frac{9l^2 + 3(l^2) + 3(l^2) + 9l^2}{8} = 3l^2 \quad (1.6)$$

Assuming there were  $n$  steps, the MSD becomes:

$$\langle x_n^2 \rangle = nl^2 \quad (1.7)$$

Therefore, the net displacement of the squared distribution is proportional to the number of steps taken and length of each step squared.

Earlier, each step ( $n$ ) was defined as the length of each step ( $l$ ) that occurred within a time ( $\tau$ ). Assuming multiple steps occurred within a time  $t$ , then the total number of steps taken can be represented as the total time over the time for each step length, or  $n = t/\tau$ . Thus, equation 1.7 becomes:

$$\langle x_t^2 \rangle = \frac{tl^2}{\tau} \quad (1.8)$$

The length ( $l$ ) and time ( $\tau$ ) parameters, however, are both constants depending on the system we have defined. Thus, we can replace this parameter with an arbitrary constant as well, which we select this to be  $2D = l^2/\tau$ , where  $D$  is our diffusion coefficient. The factor of 2 has been added to reconcile the equation with the processes described later in this text. Hence, equation 1.8 becomes:

$$\langle x_t^2 \rangle = 2Dt \quad (1.9)$$

This is the generalized equation for MSD in a single dimension that illustrates the time-based evolution of the MSD of an ensemble of particles within a defined system.

Taking this a step further and using Einstein's method treating the ensemble of particles within a volume dependent on position and time establishes a probability distribution law based on a concentration of particles between two theoretical planes  $x$  and  $x + dx$ :

$$c(x, t + \tau)dx = dx \cdot \int_{l=-\infty}^{l=\infty} c(x + l)P(l)dl \quad (1.10)$$

where  $x$  is position,  $t$  is time,  $\tau$  is a very small interval relative to  $t$ ,  $l$  is a small displacement value, and  $P(l)$  is the probability of the small displacement. As  $\tau$  is very small, the following equation can be substituted for the left-hand side of 1.10:

$$c(x, t + \tau) = c(x, t) + \tau \frac{\partial c}{\partial t} \quad (1.11)$$

In other words, the concentration at position  $x$  at time  $t + \tau$  is simply the concentration at  $x$  at the initial time  $t$  plus  $\tau$  times the rate of change of the concentration, or the flux. Furthermore, a second order Taylor series expansion can be applied to approximate the right-hand side of 1.10 about  $l$  to find:

$$c(x + l, t) = c(x, t) + l \frac{\partial c(x, t)}{\partial x} + \frac{l^2}{2!} \frac{\partial^2 c(x, t)}{\partial x^2} \quad (1.12)$$

Bringing this under the integral in 1.10 and applying 1.11 for  $c(x, t + \tau)$ , he achieved

$$c + \frac{\partial c}{\partial t} \cdot \tau = c \cdot \int_{-\infty}^{\infty} P(l) dl + \frac{\partial c}{\partial x} \int_{-\infty}^{\infty} l P(l) dl + \frac{\partial^2 c}{\partial x^2} \int_{-\infty}^{\infty} \frac{l^2}{2!} P(l) dl \quad (1.13)$$

Recognizing that the even terms cancel as  $P(l)=P(-l)$ , and the integral  $\int_{-\infty}^{\infty} P(l) dl = 1$ ,

i.e. a delta function, 1.13 became:

$$c + \frac{\partial c}{\partial t} \cdot \tau = c + \frac{\partial^2 c}{\partial x^2} \int_{-\infty}^{\infty} \frac{l^2}{2!} P(l) dl \quad (1.14)$$

$$\frac{\partial c}{\partial t} \cdot \tau = \frac{\partial^2 c}{\partial x^2} \int_{-\infty}^{\infty} \frac{l^2}{2!} P(l) dl \quad (1.15)$$

$$\frac{\partial c}{\partial t} = \frac{\partial^2 c}{\partial x^2} \cdot \frac{1}{\tau} \int_{-\infty}^{\infty} \frac{l^2}{2!} P(l) dl \quad (1.16)$$

Using unit analysis and assuming  $l$  is a constant, it can be seen from 1.16 that,

$$\frac{1}{\tau} \int_{-\infty}^{\infty} \frac{l^2}{2!} P(l) dl = \frac{l^2}{2\tau} \int_{-\infty}^{\infty} P(l) dl = \frac{l^2}{2\tau} = \left[ \frac{L^2}{T} \right] = D \quad (1.17)$$

Thus, we achieve the mathematical value for the diffusion coefficient that was used above to achieve 1.9. A final substitution of 1.17 into 1.16 achieves:

$$\frac{\partial c}{\partial t} = D \frac{\partial^2 c}{\partial x^2} \quad (1.3)$$

or Fick's second law, the diffusion equation. Hence, mathematically it has been proven that an ensemble of particles undergoing a random walk, i.e. Brownian motion, satisfies the diffusion equation. This is a very powerful result, as it illustrates that Brownian motion is the fundamental representation of particle diffusion.

More importantly, treating the probability distribution for concentration,  $c(x,t)$ , as a point source, and applying boundary conditions found a fundamental solution to 1.3 providing a normalized Gaussian distribution for the diffusion equation in 1D<sup>31</sup>:

$$c(x, t) = \frac{n}{\sqrt{4\pi Dt}} e^{-\frac{x^2}{4Dt}} \quad (1.1)$$

This has been translated to 2D and 3D by the multiplication rule for probabilities<sup>32</sup>:

$$c(x, y, t) = c(x, t) * c(y, t) = \frac{N}{4\pi Dt} e^{-\frac{(x^2+y^2)}{4Dt}} \quad (1.18)$$

$$c(x, y, z, t) = c(x, t) * c(y, t) * c(z, t) = \frac{N}{(4\pi Dt)^{3/2}} e^{-\frac{(x^2+y^2+z^2)}{4Dt}} \quad (1.19)$$

where,  $N$  is the total number of particles normalized over all dimensions. Furthermore, the solutions have also yielded the variance of the distribution, which in conjunction with statistical theory can be reconciled with the mean squared displacement achieving the same result we described earlier:

$$2\sigma^2 = 4Dt \quad (1.20)$$

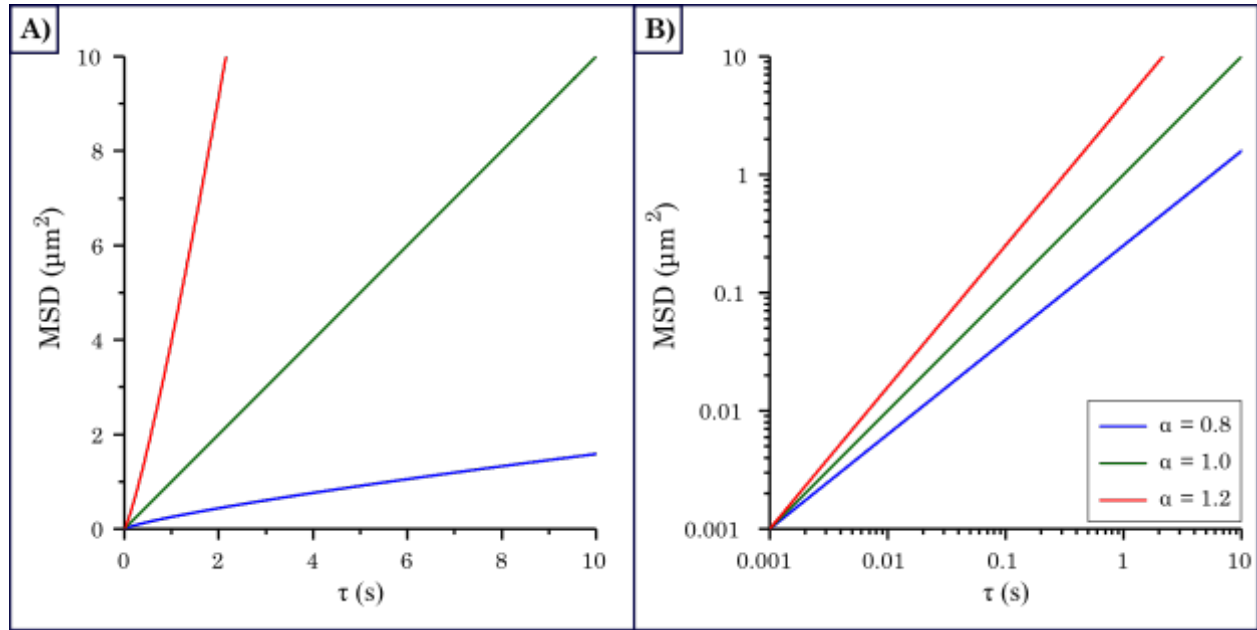


Figure 1.2 A) Time dependent evolution of normal and anomalous diffusing particle ensembles. Normal diffusion is represented by an alpha exponent of one (green). Sub- and super-anomalous diffusive motions are represented by exponents of below (blue) and above (red) one, respectively. B) A log log plot of the same diffusive particle ensembles illustrating the linearity based upon the exponents.

$$\sigma^2 = 2Dt = \langle (x - \langle x \rangle)^2 \rangle \quad (1.21)$$

Assuming the mean of the distribution,  $\langle x \rangle$ , is zero, then 1.26 becomes:

$$\langle x^2 \rangle \text{ or } \langle y^2 \rangle \text{ or } \langle z^2 \rangle = 2Dt \quad (1.22)$$

$$\langle r^2 \rangle_{2D} = \langle x^2 \rangle + \langle y^2 \rangle = 4Dt \quad (1.23)$$

$$\langle r^2 \rangle_{3D} = \langle x^2 \rangle + \langle y^2 \rangle + \langle z^2 \rangle = 6Dt \quad (1.24)$$

Thus, even though we may see no net displacement of the distribution, the mean squared displacement grows linearly with respect to time (Fig. 1.2). This provides a means to measure the displacement of a particle being tracked over time and reconcile it with its diffusion coefficient. This concept is key to the work described in Chapter 4 and provides us the means to calculate the diffusion coefficients of a particle through single particle tracking that is described later in this chapter.

The result just described was also independently found by Smoluchowski using probability theory on particle displacements. In fact, there are a multitude of ways to come to the same solution with different approaches since Einstein and Smoluchowski laid the framework. Nonetheless, Smoluchowski's approach was also from the standpoint of a random walk described by a series of arbitrary steps with dependence only on the location in the previous step<sup>16,29,33,34</sup>, which has become known as a Markovian process.<sup>33,35</sup> Thus, a step in any direction is equally as probable at any position or point in time and independent of momentum in any direction, i.e. there is no memory of where the particle has been to determine where it is going. Furthermore, by looking at the particle by step size as opposed to velocity eliminated the time and distance scale problem found in previous work. This was a key recognition that reconciled previous work based on displacements measured with a microscope with atomic theory. Moreover, it laid the framework for modern stochastic theory, or the use of probability theory to characterize random physical processes.

Although the equations described above fully defined Brownian motion as a diffusion-based process with a known constant, the dependency of that constant on temperature and viscosity was not well explained. Einstein established this relation using thermodynamics. He postulated that diffusion was related to a force driven process that was based on an osmotic, or entropic, pressure that had been well characterized in gases.<sup>36</sup> His hypothesis was based on the fact that a solid block immersed in water would create a force on the water in the form of pressure that caused the water level to rise. He correctly assumed that a group of particles of the

same material, i.e. same density, would create the same amount of force on the water assuming the same amount of mass was placed in the liquid. Thus, the sum of the particles forces would be equal to the total force applied by a single block on the solution.

He derived mathematically an equation to describe this pressure using thermodynamics and probability theory. The osmotic pressure was related to the number of particles present in the same manner that pressure was exerted by gases in the natural gas law:

$$p = \frac{R_G T}{N_A} c \quad (1.25)$$

Here,  $p$  is the osmotic pressure exerted by particles in a unit volume,  $R_G$  is the universal gas constant,  $T$  is absolute temperature,  $N_A$  is Avogadro's number, and  $c$  is particle concentration. Realizing that each particle exerted a certain pressure, or force per unit area, he recognized that the molecules of the solution would also apply a pressure and therefore a force to a suspended particle, i.e. Newton's third law. Asserting that this force would cause overall diffusion across a distance  $x$ , he used thermodynamic equilibrium to establish a balance between the forces on the particles and the osmotic pressure he had derived<sup>36</sup>:

$$\Delta FE = \Delta E - T\Delta S = 0 \quad , \text{ where} \quad (1.26)$$

$$\Delta E = - \int_0^l Fc \Delta x dx = -Fc \quad (1.27)$$

$$\Delta S = - \frac{R_G}{N_A} \int_0^l \frac{\partial c}{\partial x} \Delta x dx = - \frac{R_G}{N_A} \frac{\partial c}{\partial x} \quad (1.28)$$

Therefore

$$-Fc + \frac{R_G T}{N_A} \frac{\partial c}{\partial x} = 0 \quad (1.29)$$

$$Fc - \frac{\partial p}{\partial x} = 0 \quad (1.30)$$

In the equations just defined,  $\Delta FE$  is the Helmholtz free energy,  $\Delta E$  is energy,  $\Delta S$  is entropy, and  $F$  is force. It is important to note that the free energy, energy, and entropy were all found within the same volume and over the same distance, and hence the equations shown have been normalized over these values providing force density ( $\text{N}/\text{m}^3$ ) as opposed to energy ( $\text{N}\cdot\text{m}$  or Joules). Overall, the equation illustrates that the force applied to the concentration of particles is equivalent to the change in osmotic pressure with respect to the distance.

Using laws of mechanics, Einstein further established a force based velocity and flux based on Stokes' theory<sup>36</sup>:

$$u = \frac{F}{6\pi\eta R} \quad (1.31)$$

$$j = cu = \frac{cF}{6\pi\eta R} \quad (1.32)$$

where  $u$  is particle velocity,  $j$  is flux,  $\eta$  is viscosity, and  $R$  is the particle radius. Equating Fick's first law (1.1) to the flux just described and substituting a formula for  $\partial c/\partial x$  from 1.30, he calculated a numerical solution for the diffusion coefficient:

$$D = \frac{R_G T}{N_A} \cdot \frac{1}{6\pi\eta R} = \frac{k_b T}{\zeta} \quad (1.33)$$

This equation is known as the Stokes-Einstein Relation and established mathematically the temperature and viscosity dependence of the diffusion coefficient

related to Brownian motion that Guoy had described, further evidence that the process was indeed diffusion based.

Overall, the methods and equations described are still in use today for study of diffusive behaviors. Moreover, they are the foundation the work herein is based upon. Brownian motion is the most fundamental means of particle movement, which can be studied in any medium, assuming the particle, or ensemble of particles can be visually tracked in some manner. The motion itself is characteristic of the particle and the medium in which it is moving. Furthermore, it can be multidimensional, such as a particle diffusing freely in 3D or a protein moving essentially in 2D on a cellular membrane. The characteristics of the motion will define the properties. Thus, studying the motion gives information on the particle movement that can be related to a signaling/communication process.

### ***1.1.2. DIFFUSION IN THE PRESENCE OF AN EXTERNAL BIAS***

---

The discussion of diffusion described above is under the assumption that no external forces are acting on the particle. In other words, there is no drift or bias of the particle's movement, which does not occur in all systems. There are a variety of situations within a cell that lead to biased particle movements. These can be related to flows, transport by motor proteins, confinement, binding events, complex pathways acting as a fractal, etc. In these cases, Brownian motion is still occurring, however the forces/barriers bias the motion. These deviations from free Brownian motion are known as anomalous diffusion.<sup>33</sup> If the motion is slowed down or sped up, this is known as anomalous sub or super-diffusion, respectively.

In terms of the mean squared displacement, anomalous diffusion manifests itself in a non-linear fashion when plotted vs time (Fig. 1.2). This can be modeled with the following equation:

$$\langle r(\tau)^2 \rangle = D_\alpha \tau^\alpha \quad (1.34)$$

where,  $D_\alpha$  is the modified diffusion coefficient,  $\tau$  is time window of averaging, and  $\alpha$  is the anomalous exponent.<sup>37</sup> An  $\alpha$  of 1 indicates normal diffusion, whereas less or more than 1 indicates sub or super-diffusion, respectively. Dependent upon the exponent achieved, stochastic models can be applied to determine the best fit to the overall distribution. The model provides information on the environment causing the diffusive behavior seen.

The diffusive behavior illustrated may also be the result of multiple effectors. One such scenario is known as particle search and capture. In this event, a free moving particle experiences biasing events that cause a change in its diffusive behavior. This capture event results in confinement of the particle by some means. The particle becomes captive to the environment, which spatially can be from one to three-dimensional confinement. An example of one-dimensional confinement would be that of a protein diffusing freely in three dimensions and experiencing a binding to a lipid bilayer that limits its motion to two dimensions. An event such as this will change the particles behavior drastically as the particle is now limited to the friction caused by the lipid bilayer as well as being trapped in a single dimension. An example of three-dimensional confinement would be the use of an optical trap to capture a particle and limit its motion in all directions. In this case, however, the particle search

and capture are biased by the operator of the optical trap. Nonetheless, both cases described are illustrated in this work with different information being extracted from the particle displacements.

In the case of protein binding to a lipid bilayer, the information attained from the displacements illustrates the behavior of the particle on and off the lipid bilayer. Assuming we define the diffusion on the lipid bilayer as normal diffusive behavior, an unbound particle will then experience super diffusive behavior relative to the bound particle. Studying an ensemble of particles undergoing diffusion with binding and unbinding events will therefore give information on the particle's behavior in both environments. Understanding this behavior is key to understanding signal transduction mechanisms of a cell, as many signals across the membrane use this exact type of particle search and capture event to initiate a signaling cascade. Thus, we can achieve an understanding of the mechanical properties potentially effecting the signal transduction by particle search and capture. This type of behavior is further described in Chapter 4.

The other work described herein possesses the second type of particle search and capture described. In this case, however, we are only interested in the diffusive behavior seen while confined. This type of diffusive behavior occurs within an elastic potential that can best be equated to a spring on the macroscopic level. In terms of a random walk, it is like being placed in a belt tied to bungee cords in all directions (Fig. 1.3A) and being hit with tennis balls randomly driving you to displace from the center. Your displacement will always be biased back to the center based on the

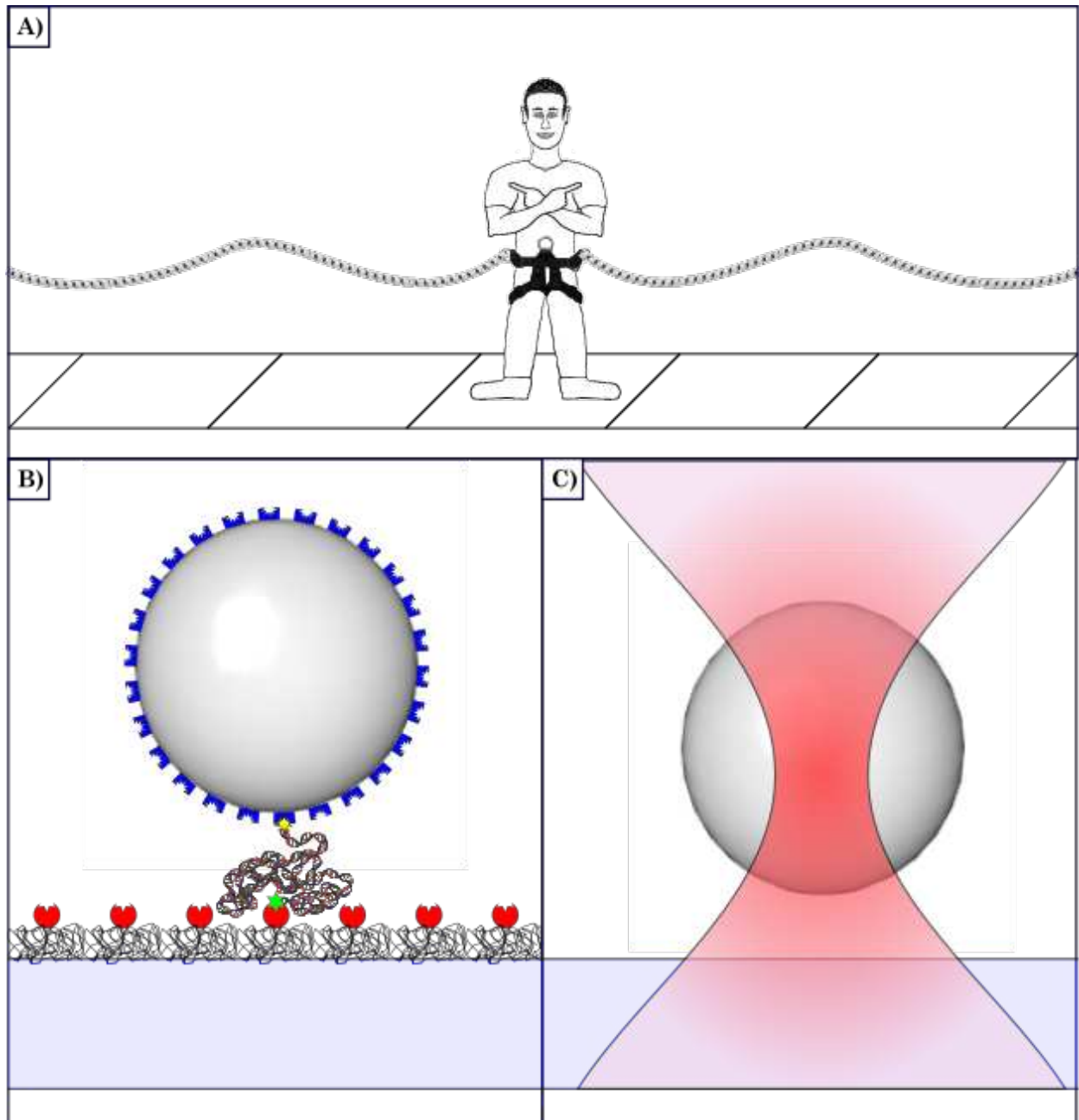


Figure 1.3 A) One dimensional biased random walk illustrated by a man on a sidewalk with bungees being biased back to the center by an elastic potential. B) A biased random walk of a bead attached to an elastomer, DNA. C) A biased random walk within a harmonic potential applied by an optical trap.

strength of the bungee cords. Your displacement from center will be dependent on the collisions occurring to push you in either direction. Furthermore, the further you displace, the stronger you will be pulled back. A balance exists between the bungee

forces and the forces of the tennis balls hitting you. The forces create an equilibrium state when put in terms of thermodynamics.

On the microscopic level, this is not much different. The tennis balls are the molecules of the medium, and the elastic force is applied externally. Some examples would be: 1) an elastic potential applied by a coiled piece of DNA attached to a bead on one end and a surface on the other<sup>38</sup> (Fig. 1.3B), and 2) an optical trapping potential utilizing light gradients focused through the particle to create a harmonic potential<sup>39,40</sup> (Fig. 1.3C ). Nonetheless, the particle experiences forces balanced between the thermal molecular collisions, the friction of the medium, and the elastic potential confining the particle.

The stochastic model describing a particle within a harmonic environment was first developed by Smoluchowski. The equation describing this is simply the diffusion equation (Fick's second law or Eq. 1.3) that balances the concentration changes ( $\partial c/\partial t$ ) with entropic forces reflected in the diffusion coefficient and the concentration gradient ( $\partial^2 c/\partial x^2$ ) and the harmonic forces of a trap ( $-k_{trap} * x$ ) dampened by the friction ( $\zeta$ ), as shown here:

$$\frac{\partial c}{\partial t} = D \frac{\partial^2 c}{\partial x^2} - \frac{1}{\zeta} \frac{\partial}{\partial x} k_{trap} c \quad (1.35)$$

This is known as the Smoluchowski equation for a 1D harmonic potential.<sup>41,42</sup>

Furthermore, this equation has an analytical solution in 1D<sup>43</sup>:

$$c(x, t|x_0, t_0) = \sqrt{\frac{k_{trap}}{2\pi k_b T [1 - e^{-4(t-t_0)/\tau}]}} \exp\left(-\frac{(x - x_0 e^{-2(t-t_0)/\tau})^2}{2k_b T [1 - e^{-4(t-t_0)/\tau}]/k_{trap}}\right) \quad (1.36)$$

where  $k_{trap}$  is the harmonic spring constant (aka trap stiffness),  $k_b$  is Boltzmann's constant,  $T$  is absolute temperature, and  $\tau$  is a characteristic time or relaxation constant equivalent to  $2k_bT/(k_{trap}D)$ . Thus, this equation provides the probability of a diffusing particle's position given an initial position and time within a trap dependent solely on the diffusion coefficient ( $D$ ), the trap stiffness ( $k_{trap}$ ), and the temperature of the system ( $T$ ). In other words, we need no *a priori* knowledge of the system other than that a particle is contained within a harmonic potential with no other external forces. Therefore, we can simply follow the particle's motion throughout time within a static trap and environment and use a distribution of displacements to derive the characteristic factors of the system, such as  $D$ ,  $k_{trap}$ , viscosity ( $\eta$ ), and particle radius ( $R$ ), which is very powerful for the work described in Chapter 3 utilizing an optical trap within a living zebrafish embryo. Without this equation/methodology, we would not have been able to calibrate out trap within the zebrafish without *a priori* knowledge of the blood cell radius and blood viscosity. Hence, it gave the critical information on our trap to accurately measure forces *in vivo* that are associated with flow and development. The measurement of such forces is critical to understanding the biomechanical signals necessary for natural development.

In both cases, a distribution of displacements is used to collect the information on a captured particle. The motion of the particle gives information on both the environment and the processes involved. The molecular dynamics are key to the different types of signaling that occur to affect the cells/tissues involved. Thus, the

study of diffusive behavior in terms of a random walk, or stochastic process, is powerful in multiple types of measurements.

### ***1.1.3. MOLECULAR INTERACTIONS***

---

Obviously, molecular interactions have been a key theme of this section. Moreover, they will continue to be a theme throughout later sections; however, the molecular interactions have solely focused on molecular collisions. Although this is a key concept to understanding force balanced relationships, other interactions do occur. For instance, two molecules can come together and bind, such as an enzyme binding to a substrate or inhibitor. The combination of two molecules can further lead to a chemical reaction, and a change in molecular composition while mass and energy are conserved. In general, this will affect the overall diffusion of the particles. The former will change the size of the particles and therefore the diffusion coefficient. The latter will change the concentration of the particles and therefore the entropic driving force that Einstein described as an osmotic pressure.

Although enzyme interactions and catalysis are of interest to us in future work, the primary interactions discussed in later sections are related to diffusion with molecular binding (particle search and capture). In our work, this is modeled by the dimerism of two of the same protein molecules each bound to a synthetic lipid bilayer thereby causing a change in their rate of diffusion on the membrane reflected in the diffusion coefficient. In such a case, the change being seen is a change in the total frictional component limiting the rate of diffusion on the membrane. Mathematically, the friction is additive<sup>44</sup>:

$$\zeta_{total} = \zeta_1 + \zeta_2 + \dots + \zeta_N \quad (1.37)$$

Assuming two particles dimerized and each bound to a lipid with equal friction, or viscous drag, then the total friction is  $\zeta_{total} = 2\zeta_{particle}$ . Thus, using the Stokes-Einstein Relation (1.12), the viscous drag, or friction, doubles, hence the diffusion coefficient is cut in half. Hence, a mathematical relationship takes shape:

$$\frac{D}{N} = \frac{k_b T}{N\zeta} \quad (1.38)$$

where  $N$  is the total number of particles bound and diffusing together. Assuming this is occurring in 2D, we expect a change in the mean squared displacement<sup>44</sup>:

$$\langle x^2 \rangle = \frac{4Dt}{N} \quad (1.39)$$

Thus, the linear relation will have a scaling factor of the slope related to the number of overall polymerized particles. Assuming a distribution of particles exists, i.e. a proportion of monomeric and dimeric molecules, then the net diffusion coefficient will reflect the overall distribution<sup>45</sup>:

$$D_{effective} = D_{monomer}F_{monomer} + D_{dimer}F_{dimer} \quad (1.40)$$

where,  $D$  is the diffusion coefficient, and  $F$  is the fraction of molecules. This will be reflected in the mean squared displacement as described above, simply providing a linear diffusion with a lower slope than expect in the monomeric state (Fig. 1.4). These types of interactions will be further described in Chapter 4.

The net effect of particle binding or chemical reactions changing particle concentration is to slow the signal transduction processes, assuming it is not part of that process. Thus, our study of diffusive motions helps us to further understand from

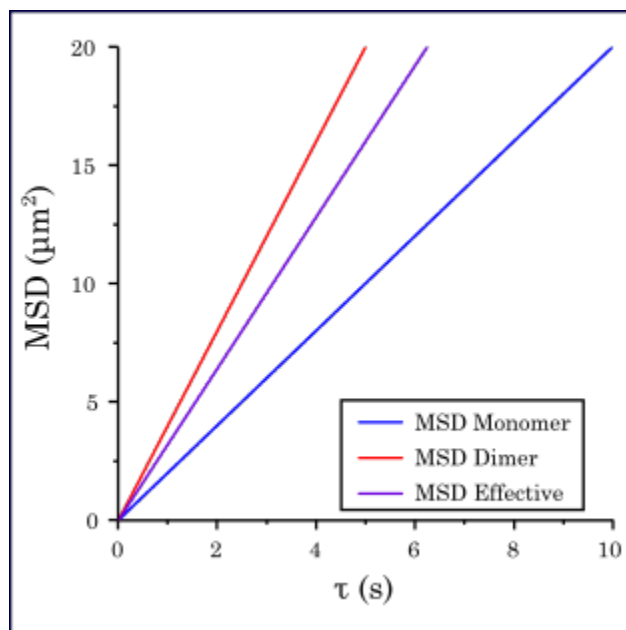


Figure 1.4: Time based evolution of mean squared displacement of an ensemble of both monomeric and dimeric particles. Each particle type has its own distribution that plays into the overall diffusion represented by the effective MSD.

a biomechanical standpoint how signaling can be affected by diffusion changes of the particles within, on, through, or outside the cell.

## 1.2. MOLECULAR CELL BIOLOGY BACKGROUND

---

Cells are the most basic unit of life. All living organisms are made up of cells falling into two classifications: prokaryotes and eukaryotes. Prokaryotes are the most basic of single cellular organisms. They include both bacteria and archaea, with archaea typically being single celled organisms found in extreme environments.<sup>46</sup> Prokarya lack membrane bound organelles, specifically a nucleus. Eukaryotes, the focus of this work, however, contain membrane bound organelles and are more complex (Fig 1.5). Eukaryotes also vary drastically in cell number dependent upon the organism. This is exemplified by the drastic differences between a single celled yeast comparative to multicellular organisms, such as humans or zebrafish.

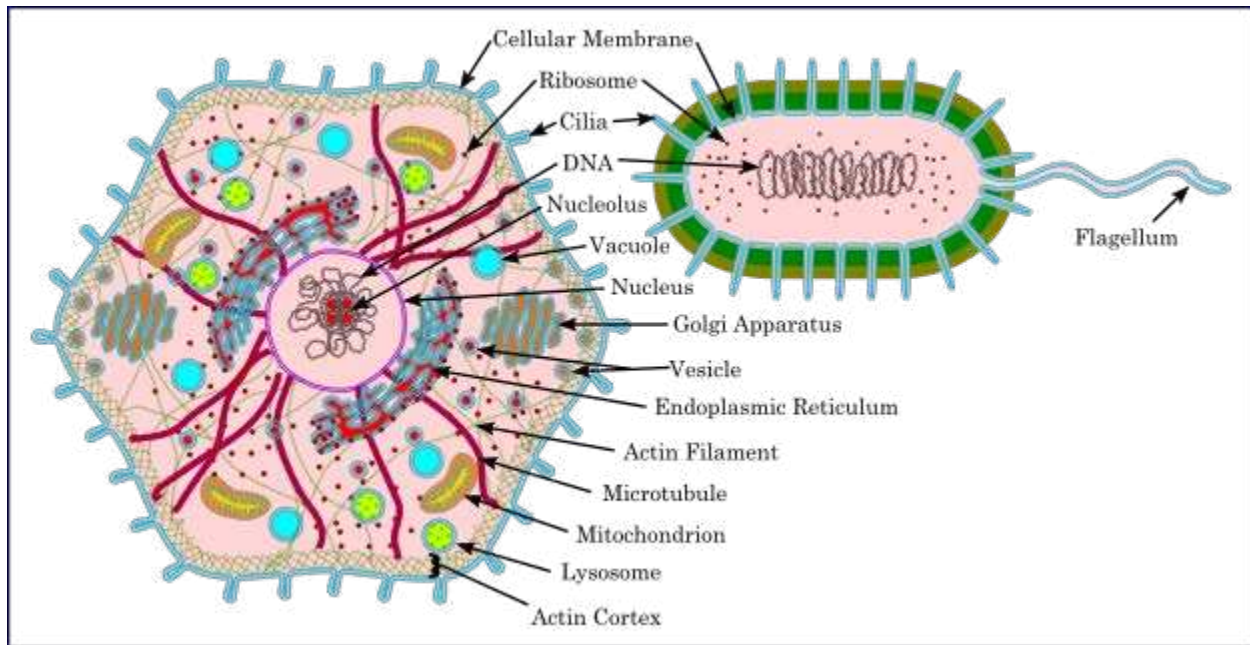


Figure 1.5: Comparative representation of a eukaryotic (left) and prokaryotic (right) cell illustrating the differences in complexity and cellular components.

Nonetheless, these two basic cell types each have a basic architecture classifiable on the microscopic level.

On the molecular level, conversely, there are drastic differences that exist amongst different eukaryotic cellular types that afford them the diversity of functions they perform. These molecular differences also manifest themselves in the biomechanical properties of the cell. In other words, two seemingly identical cells based on microscopic structures and organelles can have completely different shape and rigidity based on their molecular compositions. Thus, measuring the biomechanical/biophysical properties of the cell enables us to better understand cell type and function as well as properties effecting signals, such as the presence or absence of membrane receptors.

Cells vary their molecular composition based upon their genetic code, or the code contained within their deoxyribonucleic acid (DNA) sequence. DNA contains

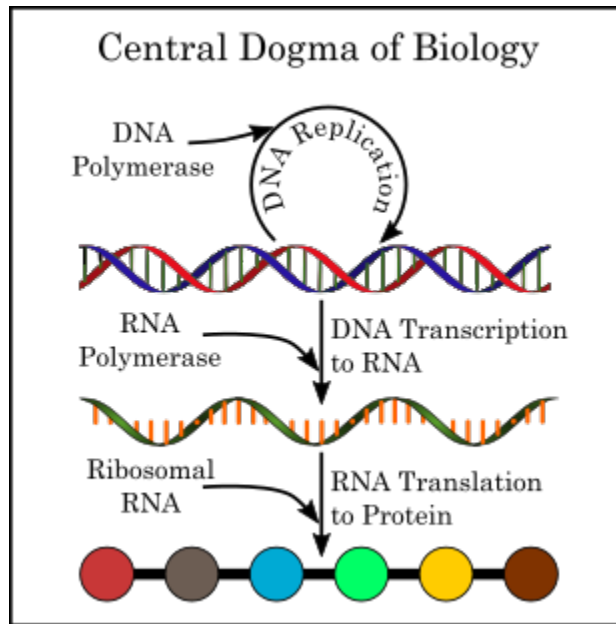


Figure 1.6: The central dogma of biology illustrating that the DNA sequence is replicated and transcribed into RNA that is translated into an amino acid sequence that makes up all proteins.

bases that can be recognized by specific enzymes, or catalytic proteins, known as polymerases to transcribe this sequence into a similar coding sequence, ribonucleic acid (RNA). The RNA is then recognized by another subset of enzymes known as ribosomes that translate it into a final coding sequence, an amino acid sequence. The amino acid sequence is what makes up all proteins, which are key to cellular processes and signaling. The overall process of DNA to RNA to protein is known as the Central Dogma of cellular biology (Fig. 1.6).<sup>46</sup> It is key to all cellular functions. Thus, understanding how communication occurs to affect this process is key to understanding how cells maintain normal cellular function, differentiate to produce a specific cell type, or modifications that produce a disease type such as cancer.

There are multiple ways to impact the function of the Central Dogma thereby effecting the overall composition of the cell. It can be effected on the DNA level by

molecular binding events enhancing or preventing transcription<sup>47</sup>, modification of the DNA itself causing modifications to the resulting pathway or protein<sup>48</sup>, or by the introduction of foreign DNA, typically a circular double stranded plasmid, to produce a non-native or modified protein.<sup>49</sup> On the RNA level, regulation can occur through enzymatic degradation<sup>50</sup>, introducing short RNA sequences to form a short double stranded area preventing translation (RNA silencing)<sup>51</sup>, introduction of rare codon sequences limiting translation<sup>52</sup>, or chemical modifications to the RNA directly effecting translation such as methylation.<sup>53,54</sup> Lastly, on the protein level, alterations can include the introduction of small molecules to bind and enhance/inhibit enzyme activity reversibly or irreversibly<sup>55-57</sup>, proteins can be unfolded by denaturation<sup>57</sup>, or by tagging proteins for cellular destruction.<sup>58</sup> Overall, the examples given are broad examples of molecular biological techniques. These techniques exist for modification of cellular function and how signals are processed potentially inducing disease type processes that can be studied to find basic functional problems and targeted solutions.

Modifications also exist that we can utilize purely for observation of cellular activities with minimal impact to cellular function. One of the most widely used modifications is the introduction of fluorescent tags for tracking protein activity and complexing as well as identifying subcellular structure. Since the discovery of green fluorescent protein (GFP) in 1962<sup>59</sup> and subsequently the identification of its coding sequence by Prasher *et al* in 1992<sup>60</sup>, a growing number of fluorescent protein molecules have been identified/engineered for molecular biological work. Furthermore, many chemical fluorophores have also been engineered for biological

work.<sup>61,62</sup> The means to fuse these fluorescent macromolecules to other molecules of interest such as other proteins, actin monomers, and DNA binding motifs have also been developed. Their overall movements and localization are microscopically imaged deducing cellular structures and functions.

### ***1.2.1. GENERAL CELL ARCHITECTURE & LIFE CYCLE***

---

As discussed in the previous section, all cells have a general architecture that can be seen in Fig. 1.5. Each component within this architecture has a specific function. Components of interest to this work primarily include the plasma and nuclear membranes, the cytoskeletal structure, and the cytosol, or general cellular interior composed primarily of water. The nucleus houses the genetic material, primarily DNA, as well as the enzymes to transcribe and replicate its structure. The nuclear envelope/membrane surrounds this and separates it from the other cytoplasmic structures protecting the genetic material.<sup>63</sup> Cytoskeletal components such as microtubules, actin, and intermediate filaments extend from the nucleus and different parts of the cell. They act as means for transport, structural support, and mechanotransduction, a process of conducting a mechanical signal from the membrane to the nucleus to produce a change in genetic expression.<sup>64</sup> The plasma membrane is a complex structure that houses many proteins and coordinates the connections between the intracellular and extracellular environments while acting as a barrier.<sup>65</sup> A dynamic interplay of communication exists between these structures that maintains the function and life cycle of the cell. These communications are

orchestrated by a variety of enzymes and other functional/structural proteins and signaling molecules.

The cellular life cycle is one of the most controlled and choreographed processes a cell undergoes. In general, this cycle is maintained by a variety of signaling mechanisms, both mechanical and chemical. Typically, the cellular life cycle is described by the means of cellular replication that occurs via mitosis or meiosis, depending upon cellular type.<sup>66</sup> Although cellular division and the passing of genetic material are important to the biological field in general, this work focuses on other more specific portions of the cellular life cycle: processes that cause membrane blebbing and cellular differentiation via mechanotransduction. In each, a response is occurring relative to a chemical or mechanical signal that herein we are developing the means to interpret.

Membrane blebbing is a protrusion from the membrane like a bubble. It occurs as a response to a local disruption of the cellular membrane with the underlying actin cytoskeletal cortex that results in a rapid, pressure driven expansion of the plasma membrane.<sup>67</sup> The expansion of the bleb occurs until the elasticity of the membrane applies a force in response equal and opposite to the pressure.<sup>68</sup> The bleb then remains static while actin polymerizes outwards to the membrane followed by a retraction of the bleb with activity of myosin II, a molecular motor protein, on the polymerized actin.<sup>69</sup> The membrane connection with the underlying cortical actin is then re-established. Blebbing is therefore a mechanical response to a stimulus. The

stimulus can be a variety of things such as chemicals inducing cellular death, uncontrolled actinomyosin activity, mechanical disruption of the membrane, etc.

The processes of the life cycle that induce membrane blebbing include apoptosis, cytokinesis, and cellular motility.<sup>67</sup> Apoptosis and cytokinesis, or programmed cellular death and division, respectively, are not two mutually exclusive cellular processes that occur within tissues. They are both involved in normal cell turnover, embryonic development, and the prevention of disease. Cellular motility also plays its role in these processes; however, motility can also be an indication of disease.<sup>70,71</sup> In the case of cancer, motility leads to metastasis and ultimately the death of the organism.<sup>70</sup> Thus, understanding membrane blebbing and the underlying biomechanical communication that happens in each of these processes is fundamental to understanding both normal and diseased cellular functions.

Cellular differentiation is also key to embryonic development, tissue maintenance, and the prevention of disease. It is one of the most studied processes, as cellular differentiation is what enables the production of specific cell types and tissues from pre-cursor cells more commonly known as stem cells, which is fundamental to the field of tissue engineering. Differentiation itself towards a specific cellular type happens in a variety of ways that include both chemical and mechanical cues.<sup>72</sup> Chemical cues are typically growth factors that stimulate specific genetic pathways to be turned on thereby producing specific proteins key to each cell type and function. Mechanical cues, however, have also been found that are key to the development of specific tissue architectures. In many cases during earlier embryonic

development, these mechanical cues are pressure driven flow forces that develop to enhance the distribution of growth factors and nutrients throughout the appropriate tissues when simple diffusion becomes a time limiting process.<sup>9,73-76</sup> This process is further discussed later in terms of organismal hierarchy and normal tissue development specifically related to blood flow forces that were directly measured in the work described in Chapter 3.

### ***1.2.2. THE PLASMA MEMBRANE***

---

The most important cellular entity to the work presented herein is the plasma membrane. All measurements that have been made involve forces on or within the membrane itself as studied directly through living cells and organisms or modelled with a synthetic lipid bilayer. Thus, it is important to understand the properties that make the plasma membrane so dynamic. Moreover, our interpretations of these properties further identify fragments of complex mechanisms enabling communication across this barrier effecting survival and environmental adaptation.

#### ***1.2.2.1. PHYSICAL PROPERTIES***

---

The fluid mosaic model best describes the overall structural properties of the plasma membrane (Fig. 1.7).<sup>65,77</sup> Within this model, the structure is dynamic and moving as opposed to static and unchanging. The membrane itself can adapt to its environment by changing its shape, dampening pressure, and applying forces related to underlying cytoskeletal structure. Particles, both lipids and proteins, can move amongst each other allowing free diffusion within the membrane. Furthermore, these same particles can be inserted and removed from the membrane changing its overall

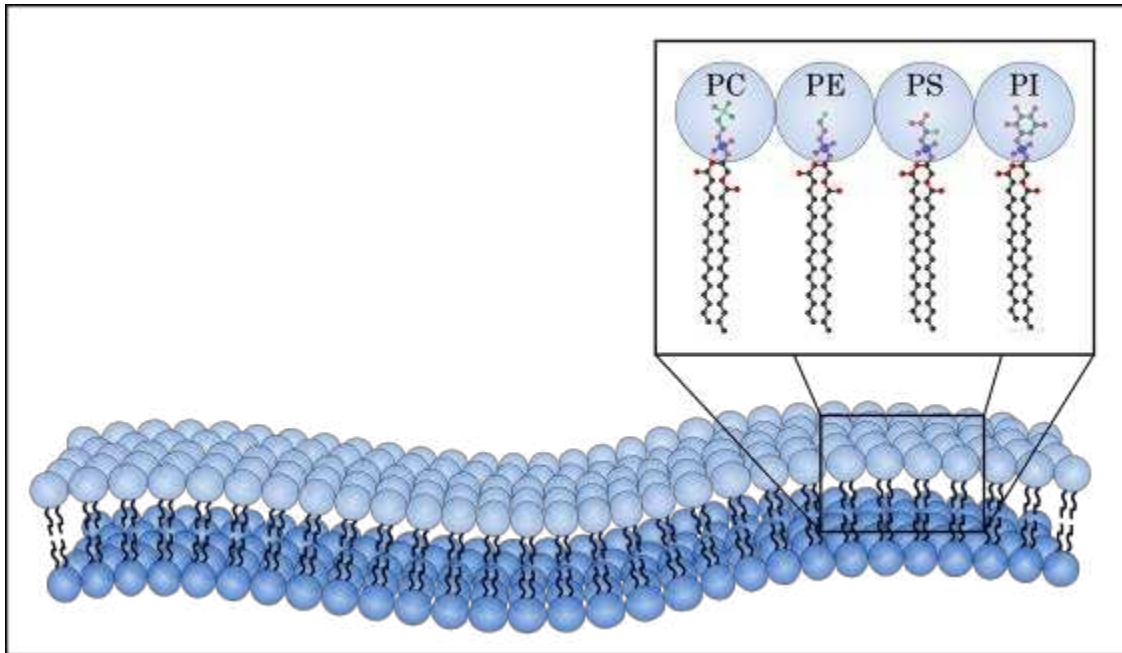


*Figure 1.7 Fluid dynamic model of a lipid bilayer meant to show that the membrane is fluid and moving as opposed to static and unchanging. Particles can move amongst each other diffusing throughout the membrane layer. The membrane is made of phospholipids whose chemical structures are shown inset.*

composition. The composition is not separated amongst particle types either, they intermingle and create what is the mosaic of the membrane.

The cellular membrane itself is a double layered entity made up primarily of molecules known as phospholipids (Fig. 1.7 Inset). These phospholipids have a phosphate group head with tails consisting of varying lipid composition. The phosphate head provides a hydrophilic nature, whereas the lipid tail is highly hydrophobic. This is known as an amphipathic molecule.<sup>78</sup> The greatest benefit of these amphipathic molecules is that they self-assemble in aqueous solutions to create micelles and other structures such as unilamellar vesicles. In other words, the structure of the cellular membrane spontaneously forms through molecular entropic forces via minimization of the energy landscape, i.e. like dissolves like and the polar heads organize towards the water based solution while the tails organize towards

each other.<sup>79</sup> This creates a barrier limiting molecular transport from the interior to exterior and vice versa simply by hydrostatic interactions.

The act of forming a barrier is the most important function of the plasma membrane. The effect of this barrier, however, is dependent on a variety of properties related to the molecular species. The smaller the species, the more likely it is to diffuse across the membrane driven by the entropic forces described earlier that lead to an osmotic pressure. Uncharged species also diffuse freely across the membrane, such as carbon dioxide (CO<sub>2</sub>) and oxygen (O<sub>2</sub>). This is a property that is key to cellular respiration involved in the production of energy molecules of the cell. Lipid soluble, or more hydrophobic molecules have the ability pass dependent on the size; however, water soluble or charged species, i.e. salt ions, are prevented from crossing. This overall function of the lipid bilayer is known as selective permeability, which is key to the function of many different cellular types.

The selective permeability, however, can limit the function of the cell if it cannot get key nutrients or molecules into the intracellular environment. Furthermore, signaling molecules that could not cross would not be detected, which would prevent communication and a cellular response. In some cases, this is beneficial to the cell because it does not respond to a negative stimulus and is not harmed by the particle's inability to enter the cell. However, when it is necessary to detect, the cell has come up with a variety of means to conduct the signal. Membrane protein channels exist to channel the molecules through the cell.<sup>80</sup> Other membrane proteins can bind the molecule on the external surface causing a conformational

change to the protein on the internal surface, which can then activate/inactivate another protein through its acquired ability to bind. The conformational change could also induce enzymatic function enabling catalysis of molecular changes in the cell leading to conduction of the signal. A membrane channel can also be effected by the conformational change just described causing it to open for a different molecule to enter the cell.<sup>80-84</sup> These represent the protein related means of conducting a chemical signal across the membrane leading to gene related regulation within the cell.

The cellular membrane also functions as a means of mechanical stability by forming complexes with the underlying cytoskeleton. Typically, proteins within the membrane anchor to the underlying actin structure known as the cortex.<sup>85</sup> The dense cortical actin structure provides rigidity to the typically elastic membrane.<sup>86,87</sup> Furthermore, these interactions enable the formation of more complex membrane protrusions, such as cilia, filopodia, and lamellipodia that enable movement.<sup>71,85,88,89</sup> These interactions can also form cellular anchoring points known as focal adhesions that provide further mechanical stability as well as a means of sensing mechanical changes in the external environment.<sup>90-94</sup> In general, it is these mechanical properties of the cell that we are most interested for the work described.

#### *1.2.2.2. SYNTHETIC LIPID BILAYERS*

---

The amphipathic nature of the phospholipid molecules enables the production of an *in vitro* model of a plasma membrane. This model is known as a synthetic lipid bilayer, which was used in the work described in Chapter 4. The benefit of such a model comes in the ability to tune and select the molecules present within the

membrane.<sup>95</sup> As discussed above, the cellular membrane is an extremely complex and dynamic entity that performs multiple functions. Furthermore, the complexity of the membrane in conjunction with the difficulty of maintaining and measuring on live cells lends itself to such a model.

Synthetic lipid bilayers can be formed on a rigid glass surface spontaneously by small unilamellar vesicles. Upon formation, they act similarly to the cellular membrane, and will allow other molecules, such as proteins, to bind or insert themselves. This creates a freely mobile, uncompartimentalized membrane for free diffusion of molecules. The tunability of the membrane, such as lipid components, cholesterol content, etc. causes changes in the binding dynamics and the coefficient of friction resulting in dynamic changes in the diffusive patterns in molecules. This makes it an ideal platform to measure varying effects on molecular dynamics outside the natural membrane.

### ***1.2.3. CELLULAR TYPES & THEIR ORIGINS***

---

Earlier, cell types were defined as falling into one of two categories, prokaryotic and eukaryotic, with the focus being on the latter. Clearly, across different organisms, there also exist drastic cellular differences, hence the existence of different organisms and species. Cellular differences, however, also extends across an individual organism. Multicellular organisms possess a variety of different cellular types all with specific structures and functions. Furthermore, a hierarchy exists within the organism that starts on the cellular level. This hierarchy for sexually reproducing organisms, such as the vertebrate lineages in this work, starts from the fusion of two

single cells. Reproductive parent cells merge to produce a viable single cell that will grow, divide, and differentiate into the tissues, organs and systems that make up an individual organism. As differentiation occurs, different systems are produced that work in concert to keep the organism alive and functioning. Here, the focus is on the development of the blood vessels comprising the cardiovascular system in which direct measurements were taken in Chapter 3.

#### *1.2.3.1. OVERVIEW OF VERTEBRATE ORGANISM HIERARCHY*

---

The general hierarchy of a vertebrate organism illustrated in Fig. (1.8) starts on the cellular level, which is why we define cells as the most basic unit of life. Throughout development from the fused, or fertilized, single cell, the cells begin to differentiate into different cellular lineages based on genetic and environmental cues. As differentiation continues the individual lineages begin to produce multiple cell types. These individual cell types continue to replicate and combine to form tissues. These tissues coalesce to produce complex organs with individual functions. These organs that perform concerted functions together then make up systems. These systems combine to make up an organism. The systems function together to maintain homeostasis within the organism that is required to preserve life.

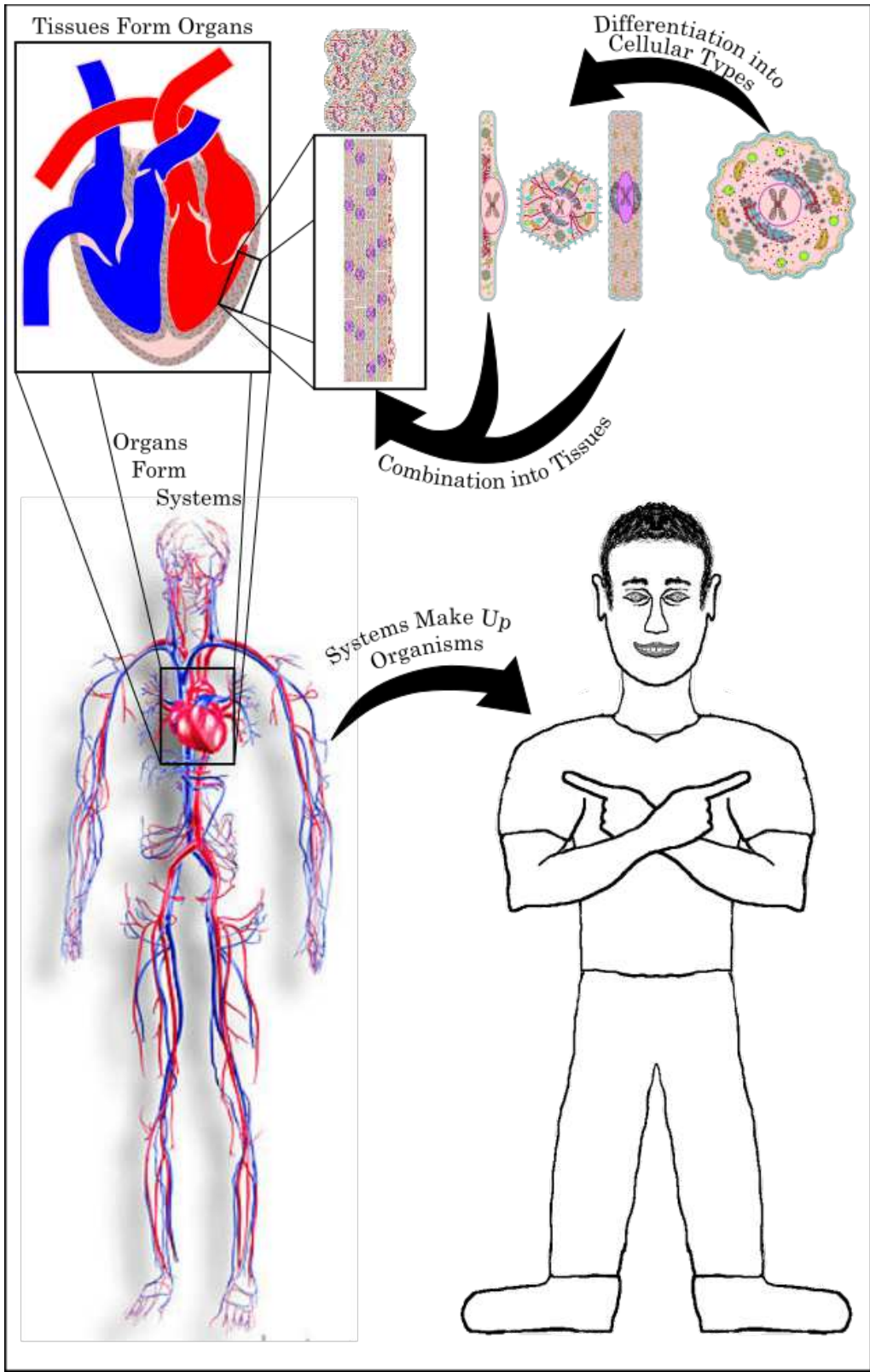


Figure 1.8 Organismal hierarchy illustrated through the cardiovascular system. Stem cells differentiate into different cellular types based on environmental cues. The different cellular types combine into tissues that in turn make up organs and vessels that combine into the systems that work in concert to maintain an organism.

Normal blood vessel formation is key to the function of the cardiovascular system, the first functional organ system to develop in the vertebrate embryo.<sup>96</sup> This system circulates blood throughout the organism to individual organs and tissues to provide nutrient, gas, and waste exchange key to cellular respiration.<sup>97</sup> The cardiovascular system maintains similar architecture across vertebrate organisms with differences in heart structures. The overall formation mechanisms of cardiovascular structures are similar as well.<sup>98</sup> Blood vessel development, the focus herein, occurs by one of two processes: vasculogenesis and angiogenesis.<sup>99</sup> Vasculogenesis is an assembly process that forms blood vessels from precursor cells known as angioblasts. Angiogenesis, conversely, is the sprouting of new blood vessels from existing blood vessels. Each has its place in formation of vascular networks. Furthermore, each involves environmental cues, chemical or mechanical, to stimulate the formation.<sup>73,100</sup> Overall, a consistent vessel architecture is produced across organisms with the architecture dependent on vessel location and flow characteristics.

Chemical cues are seen in the form of growth factors, such as vascular endothelial growth factor (VEGF). Initially, these cues will depend on diffusion as flows do not exist to distribute the factors.<sup>100</sup> Furthermore, diffusion will occur extracellularly until the factors find a receptor on the cellular surface that is also dynamically diffusing within the cellular membrane. Upon receptor binding, this will cause a signal cascade that leads to blood vessel formation. In the case of VEGF,

receptor binding will also cause dimerization of the tyrosine kinase receptor protein to initiate that signaling cascade.<sup>101,102</sup> This is very similar to the work described in Chapter 4 with a different protein model and dimerization. Nonetheless, the mechanism in Chapter 4 may be applicable to this model and signaling mechanism.

Mechanical cues also exist in the form of pressure and the resulting stresses and flows due to pressure dynamics and gradients, respectively. Primarily, the evidence for mechanotransduction of signals related to pressure driven stresses and flows effecting cellular differentiation comes from *in vitro* models on endothelial cells.<sup>93,103–110</sup> More recently, researchers have found evidence for mechanotransduction in *in vivo* models through the presence of ciliary projections from endothelial cells that line the lumen of the vessel. These cilia can mechanically transduce a signal based on the level of frictional flow, or shear stress, across them.<sup>93,103–112</sup> The overall mechanisms tied to mechanotransduction and chemical signaling however have not been fully elucidated as to how much one impacts the other, and vice versa. Thus, the development of *in vivo* means to measure and evaluate the processes is key to understanding the factors that lead to normal vessel development. The work presented in Chapter 3 focused on development of an *in vivo* biomechanical measurement methodology for better elucidating these pathways in the future.

### **1.3. MICROSCOPY BACKGROUND**

---

To understand microscopy, we must first understand the fundamentals of light, as these fundamentals make microscopy possible. Light is a form of

electromagnetic radiation, or waves of electric and magnetic fields that propagate through space at a constant speed, the speed of light.<sup>113</sup> These waves possess energy ( $E$ ) correlating to the frequency of oscillation ( $\nu$ ):

$$E = h\nu \quad (1.41)$$

where,  $h$  is Planck's constant. The frequency varies inversely proportionate to the wavelength ( $\lambda$ ) of electromagnetic radiation:

$$c = \lambda\nu \quad (1.42)$$

where,  $c$  is the speed of light. Combining these two equations gives us energy in terms of wavelength:

$$E = \frac{hc}{\lambda} \quad (1.43)$$

Electromagnetic radiation is typically identified by its wavelength, which falls on a spectrum. This spectrum, in increasing wavelength, includes gamma rays, x-rays, ultraviolet (UV) light, visible light, infrared radiation, microwaves, and radio waves.<sup>113</sup> In this work, we are most interested in electromagnetic radiation that falls within the visible and near infrared spectrum (400-1100nm).

As can be seen in equation 1.42 above, energy increases with increasing frequency or decreasing wavelength. This is an important property, as this means that differing wavelengths hold variant energy that can be used in diverse capacities. That energy is thermodynamically conserved, which means that this energy can be converted, or used in another form. The energy can be transferred to the electrons contained within an atom or molecule to cause the electrons to jump from lower energy levels, or valence shells, to higher levels to create an excited state (Fig. 1.9).<sup>114</sup>

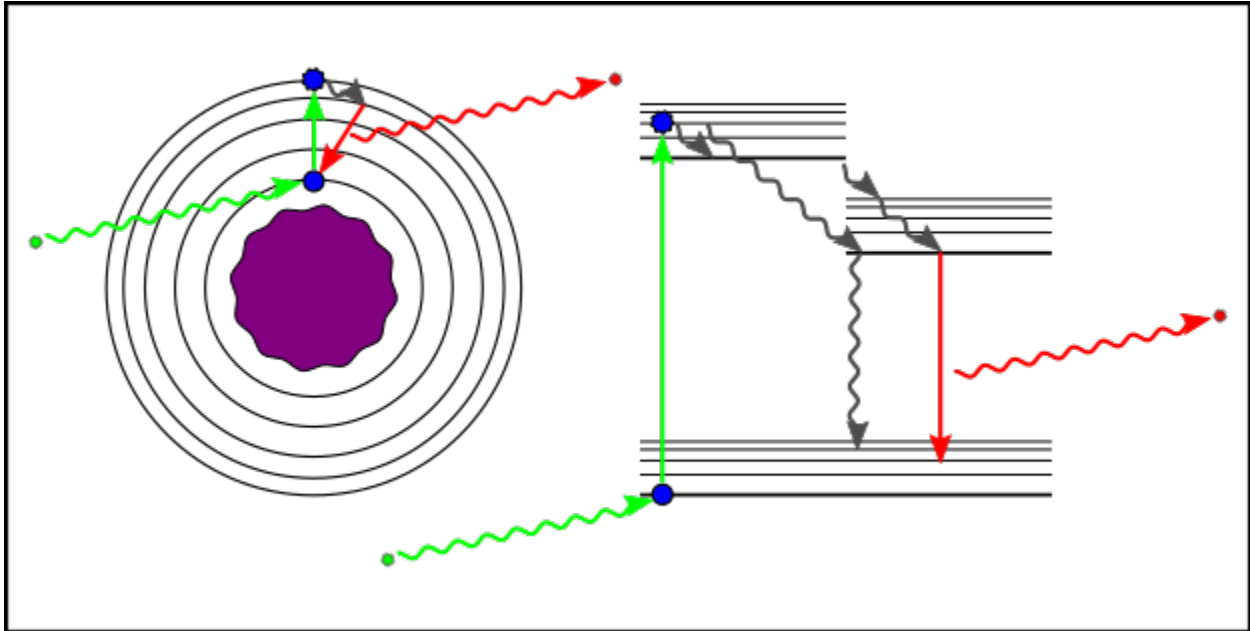


Figure 1.9 Jablonski diagram illustrating photonic excitation of an electron and pathways of relaxation back to the ground state, which includes fluorescence.

This excited state can vary in stability, which translates to the amount of time that the electron wants to spend there, otherwise known as the lifetime of the state. Nevertheless, the electron will want to return in some way to its initial, most stable level, or ground state. This happens by the electron “decaying” back level by level until it reaches this state. In each decay step, energy must be released for conservation laws to hold. This can happen visibly by the emission of a wavelength of light (fluorescence), or it can happen through the production of wavelengths invisible to the human eye typically in the spectrum of heat. The overall result, is energy emission equivalent to the initial energy that was absorbed.

The energy can also impart a force on to the atoms seemingly infinitesimally small that minorly redirects their motion, i.e. a change in momentum.<sup>115</sup> This is an important principle because it means light can impart forces, on other bodies, as will be discussed later. Light therefore can act as a particle and holds quanta of energy,

which are known as photons and were originally described by Einstein as well.<sup>116</sup> The behavior as both a wave and particle is known as the wave particle duality theorem of light.<sup>117</sup> Photons, furthermore are very small with relatively no mass and can pass between the gaps and spaces of atoms, assuming no collisions occur. This is an extremely important concept to microscopy, as it means electromagnetic radiation passing through a sample can be manipulated and detected.

Light passing through different substrates, or media, will also display differing properties within these forms. When considered from a molecular perspective and recognizing that all forms will have differing compositions, this makes sense as the physical properties of the substrates will change relative to the molecular composition as the light passes from one to the other. In passing between the differing substrates, the photons will encounter in some way an interface of differing molecular or atomic types that can cause them to be reflected, refracted, diffracted, scattered, absorbed, or some combination of these events. Reflection is simply the photons encountering a dense molecular surface that causes them to bounce and continue on a path equal and opposite to the angle of incidence, or collision. Refraction and diffraction are both bending of light either through an interface or at an edge, slit, or pinhole, respectively. In both cases, the bending is characteristic of the molecular properties of the material and the angle of incidence; however, in the case of refraction, the molecular properties causing the bending creates an index of refraction characteristic of the material the photons are passing through. Scattering happens in all materials and is random deflections of the photons from their original path. Absorption is a transfer of the

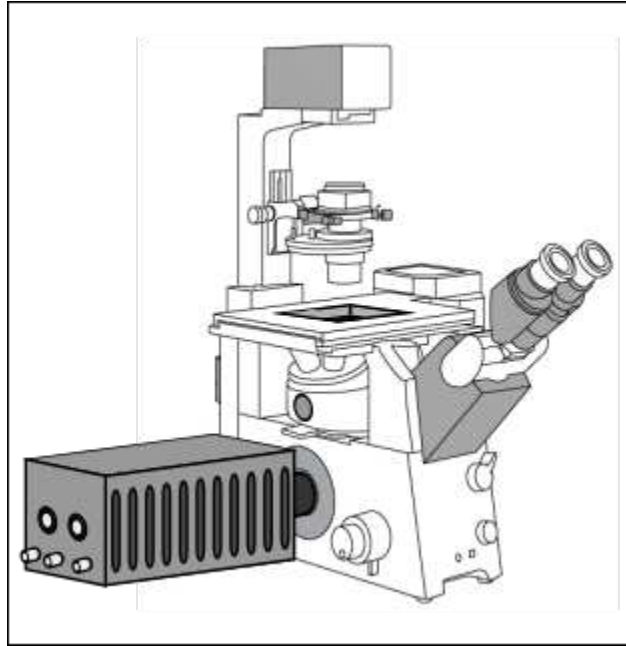


*Figure 1.10 Simple illustration of an optical microscope. This image was modified from an image available on Olympus's website for an IX71/81 microscope.*

photons energy into an electron of the molecules within the material creating a total exchange of energy into the excited state described above. All these photonic interactions can occur at an interface of material differences.

Ultimately, the photons will either be transmitted through the substrate or lost to reflection, scattering, or absorption. It is the manipulation of these interactions that enable us to focus, manipulate, and magnify electromagnetic radiation to visualize and interpret microscopic structures, properties, and events. In the studies to be presented, microscopy is fundamental to the collection of data (images) for analysis of signals. The microscope makes use of simple and complex optical arrangements to magnify an image plane that is in some way a transmission of light/energy visualized by a detector, which could be a camera, a human eye, a photodiode, etc (Fig. 1.10). This ties back to the concept described earlier with

diffusion in understanding that particle collisions act in the form of energy transmission within a system. In this case, the particles are the photons of light just described. These photons pass through samples, or the gaps between atoms, to collide with the detector that is converted to a signal. The more photons collected, the larger the signal.

The signal seen will be related to the photonic energy absorptions, emissions, and transmissions, which will manifest themselves in the image contrast pattern seen at the detector. More optically dense areas correlate to larger levels of absorption or scattering and are manifested as darker areas in the image. Less dense areas exhibit greater transmission shown as brighter areas in the image. Furthermore, optical filters designed for absorbing, reflecting, or transmitting can be placed in the image path targeting certain colors thereby isolating specific wavelength photons. This is a key concept used for fluorescence microscopy that allows the imaging of fluorophores, such as GFP described above.

Multiple forms of microscopy exist making use of the physical properties of light to perform specific functions applicable to the information to be extracted. The work presented herein makes use of specific forms of complex microscopy that are based on simpler bright-field and fluorescence microscopy. These microscopy types will be briefly described in the context of the work to be presented.

### ***1.3.1. MICROSCOPY TYPES***

---

#### ***1.3.1.1. BRIGHT-FIELD MICROSCOPY***

---

The simplest form of all microscopy is bright-field. In this setup, a sample is illuminated from top or bottom with the light being transmitted through to optics on the other side (Fig. 1.10). The light is collected and imaged on a detector providing information on the underlying sample through variations in optical density and refraction. More optically dense areas causing more scattering will appear darker. Conversely, less dense areas appear brighter, as described above. The areas where light is transmitted will refract variably also contributing to this pattern. Thus, contrast between areas and structures shows up in the gradient of brightness, or photon concentration, hitting the detector. Structural differences therefore are seen as contrast differences in the images. This type of microscopy is employed in conjunction with optical tweezers microscopy described below to provide structural information on the subjects being measured upon.

#### ***1.3.1.2. FLUORESCENCE MICROSCOPY***

---

Fluorescence microscopy is like bright-field microscopy in that a sample is illuminated with a source of light. The difference is that the source of light used to illuminate the sample is wavelength targeted to a specific molecule, or fluorophore, that will absorb within that range. This energy coming in will be absorbed through a collision with an electron creating the excited state described above. When the

electron decays back, there is an emission of energy in the form of a longer wavelength of light. This creates the fluorescence signal that is detected.

The fluorescence signal is filtered out from the excitation signal by optical filters. These filters block the excitation wavelength from being transmitted to the detector allowing only for detection of an emission wavelength characteristic of the fluorophore. Thus, a fluorescence signal is seen on the detector relative to the fluorophore particle position. This creates a structural image based solely on the fluorescent probes being used. The fluorophore thereby eliminates the visualization of all other non-fluorescent structures. In conjunction with molecular designs described earlier, such as fluorophore fused proteins, their structural locations can be imaged providing enhanced structural resolution over bright-field microscopy.

### *1.3.1.3. TOTAL INTERNAL REFLECTANCE FLUORESCENCE MICROSCOPY (TIRF-M)*

---

Obvious from the title, total internal reflectance fluorescence microscopy (TIRF-M) is a specific type of fluorescence microscopy. This type of microscopy makes use of the index of refraction properties of different materials. As stated above, the index of refraction tells us how much the light is bent when moving from one material of the other. The amount of refraction, or bending, is dependent both on the incident angle and the material differences. If the incident angle becomes too large to allow light transmission through the sample, the incident light is completely reflected at the second interface, otherwise known as total internal reflection. Thus, there exists a critical angle where no light will be transmitted into the sample (Fig. 1.11).

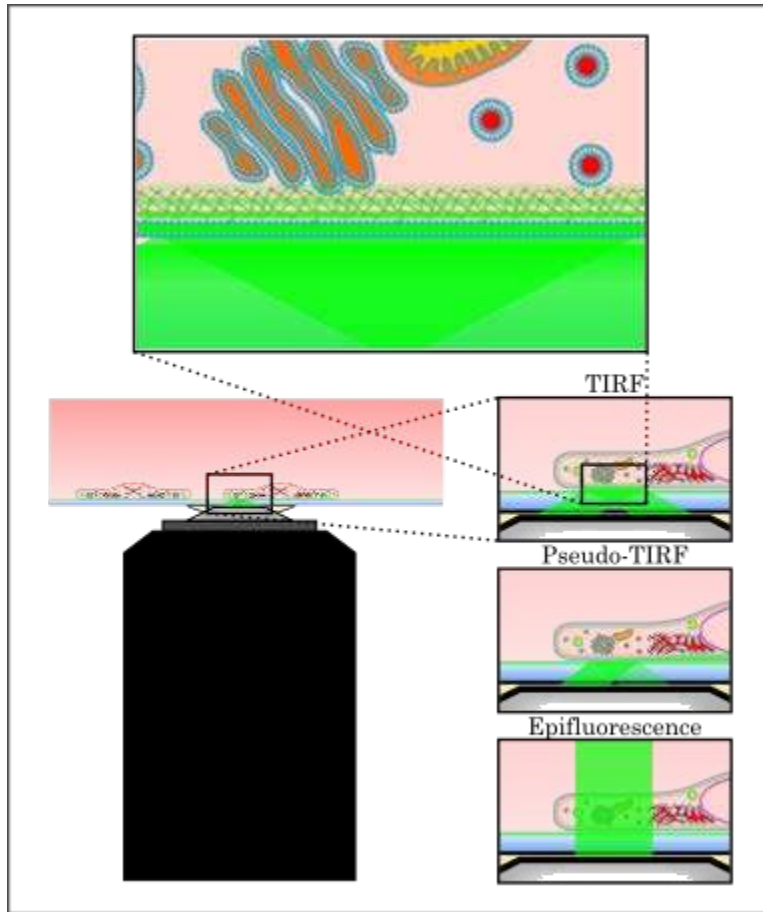


Figure 1.11 Illustration of TIRF microscopy and the effect of the angle of incidence.

Although no light is transmitted through the sample, there is a change of momentum via the change in light direction that occurs at this surface. As with any change in momentum, energy is transmitted at the collision interface. The energy however, cannot cause a strong force change causing a displacement, yet it can be transmitted into the medium at the equivalent level of the wavelength being reflected creating an evanescent wave.<sup>118</sup> Thus, the fluorophores can still be excited to a higher energy level with the transferred energy. The intensity, or magnitude, of the energy being transmitted at this surface however is not transmitted throughout the entire depth of the sample. The magnitude decays exponentially over a maximal distance,

typically around 100 nm into the sample.<sup>119</sup> Only a small portion of the axial sample is illuminated limiting the fluorescence seen to within that layer.

The benefit to this type of microscopy is that you are no longer illuminating all planes of a vertical sample as in classical fluorescence, or epifluorescence microscopy. By eliminating vertical planes above 100 nm, excess signals are eliminated that can distort or wash out the intensity being seen in the initial layer. This lends itself greatly towards use in studying cellular environments specifically found within the plasma membrane adhered to the surface. Thus, we can specifically study fluorescent molecules within the membrane and understand the dynamics therein. In this work, this principle has been extended into synthetic lipid bilayers for the study of monomeric and multimeric particle diffusion.

#### *1.3.1.4. OPTICAL TWEEZERS MICROSCOPY*

---

The most theoretically complex form of microscopy used in this work is the optical tweezers microscope. Although the theory to be developed below is rather complicated, the design of such a microscope is extremely simple. All one needs to achieve an optical trap is a high-power laser source (any wavelength), high numerical aperture objective, an optical microscope, and the necessary optics to collimate and direct the laser source to the back of the objective thereby focusing into the sample. It is this tight focusing of a gaussian beam that is key to achieving a 3D optical trap.

Key to understanding an optical trap is the theory that light can apply a force, or a radiation pressure. Working from Maxwell's theoretical evolution of radiation pressure, Lebedev showed in 1901 that this pressure did exist and that the pressure

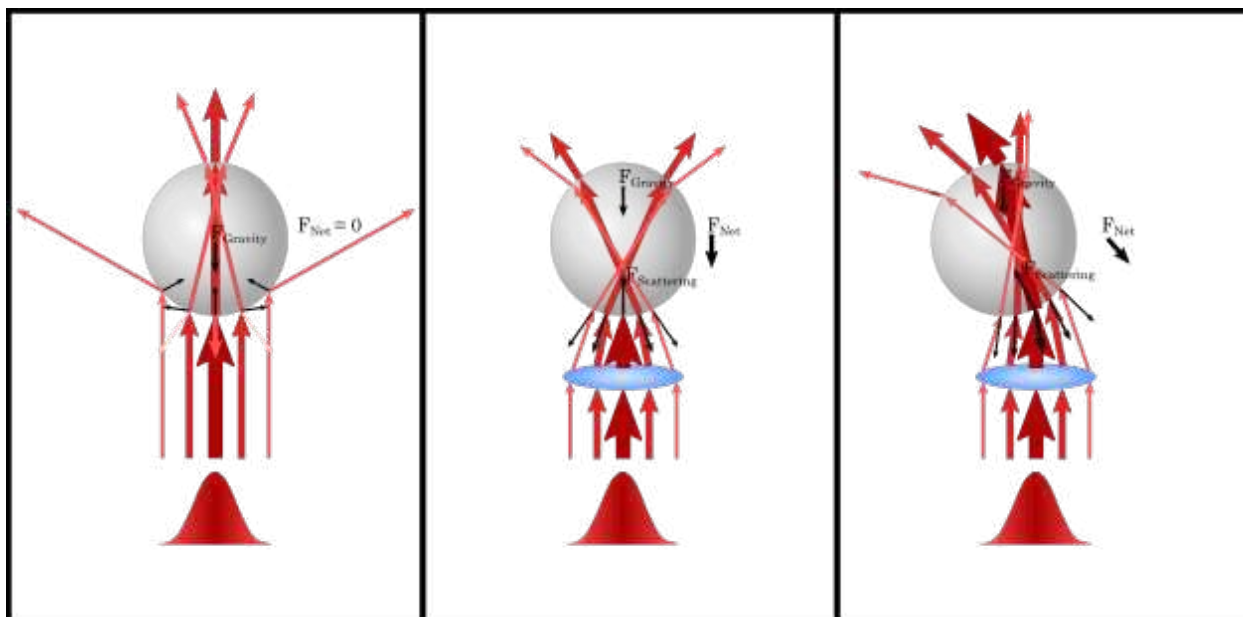


Figure 1.12 Force based illustration of an optical trap. A) Illustration of the lateral trapping effects of a collimated beam with the axial force balanced by the force of gravity. B) Focusing of the collimated beam through the sample creates an axial trapping force pulling the bead downward to the center of the focus. C) Displacement of the bead from center both laterally and axially leads to forces pulling back to center.

was higher on a reflective surface as opposed to an absorbing surface.<sup>115</sup> Extending this work to dielectric particles, Arthur Ashkin showed in 1969 that a radiative pressure could be applied by a laser source causing particle levitation.<sup>120</sup> Unforeseen and inexplicable at the time was the fact that the beam applied to cause axial levitation also created a radial trapping force allowing further manipulation of the particles. The radial trapping was found to be a result of the gradient light forces applied by the intensity distribution of the beam. This laid the groundwork that eventually showed in 1986 that a single focused beam could produce a 3D optical trap upon such particles.<sup>121</sup> The difference with this trap was that the axial force of scattering, i.e. the radiative pressure, was now balanced by the gradient force being focused through the particle as opposed to gravity (Fig. 1.12). Thus, this was the first

illustration that a negative radiation pressure could be applied to a particle driving it in the opposite direction of the propagating beam.

Ashkin reconciled this force using ray optics theory recognizing that two things were occurring outside of the force due to gravity: 1) a radiation pressure based on Rayleigh scattering was happening at the surface of the particle based on reflected photons, and 2) a positive and negative radiation pressure was being applied based on the refraction of the rays passing from the initial surface of the particle and out the other side. In either case, there is a change of momentum of the photon particle as it is either reflected or refracted, which translates to a force being imparted on the particle being trapped that is the sum of the force vectors due to momentum change (Fig. 1.12). Of course, the individual photon has an almost negligible mass traveling at the speed of light creating a relatively low momentum and thereby imparts a very small force. In a concentrated laser beam, however, there are numerous photons being focused into the trap that additively each impart a force on the particle as their paths are changed. Furthermore, a gradient of photons is found both radially and axially based on the Gaussian beam profile and the act of focusing it through a point, respectively. Thus, this gradient drives the force relative to the particle position within the trap (Fig. 1.12).

Forces due to the change in momentum of photon rays as just described are applied to particles in diameter that are relative large comparative to the wavelength of light of the laser source, otherwise known as the ray optics regime. On the other end of this spectrum are particles whose diameters are relatively small comparative

to the wavelength of the source, which is known as the Rayleigh regime. Given the name, it is simple to deduce that Rayleigh scattering dominates the light photons hitting the particle in this regime. Therefore, the scattering force is more influential in this regime making particle trapping more difficult. Nonetheless, Ashkin and his colleagues showed trapping of particles much smaller in radius than the wavelength used. This is due to the nature of the light energy being electromagnetic radiation that it imparts an alternating dipole moment on the particles it is focused through.<sup>122</sup> This induced dipole then experiences a potential based on the electric field being applied by the light source. The electric field is dependent on the intensity of the light being passed through, which for a Gaussian beam is spatially dependent with the highest intensity in the center. Thus, the electric field is a gradient based on the intensity of light with the force being directed opposite to the electrostatic potential generated by the propagating beam. The particle with an induced dipole will then experience a force relative to the potential that points towards the center of the trap.

The two circumstances just described do not describe what is happening when the particle radius is of similar size to the wavelength being used for the trap. In this case, more complex theory is necessary to describe the forces applied<sup>123</sup>, which is beyond the scope of this research. In general, the potential of the trap is based on the intensity of light, which is a Gaussian gradient that can be modeled as a parabolic potential over short distances from the trap center.<sup>124</sup> A parabolic potential is an elastic potential, which ties back into the discussion above of Brownian motion within

a harmonic. Thus, an optical trap can be modeled as a Hookean spring with the gradient force being described as:

$$F_{grad} = -k_{trap}\Delta x \quad (1.44)$$

where  $k_{trap}$  is the trap stiffness and  $\Delta x$  is the displacement of the particle from the trap center. Thus, there is an overall force balance that exists that is dependent on the force due to gravity, the force due to scattering, the force due to the light gradient, and the force due to thermal molecular collisions of the medium. Introduce another force that offsets the particle from the center and the displacement value can be used to measure the force applied assuming the trap stiffness is known. Optical traps therefore give us the ability to directly measure forces purely through the application of an intense focused beam of light.

Given that the force applied is dependent on the intensity gradient of light being focused through the particle, one can quickly deduce that the application of laser power will directly influence the force application. As intensity is a measure of power transferred per unit area, i.e.  $I \propto P/A$ , an increase in power will lead to an increase in the gradient of intensity. As the force is directly proportional to the gradient of the potential, which is driven by the intensity, the force applied will increase directly proportional to the increase in power. The positions within the trap are fixed, therefore the change in force must be reflected in the trap stiffness. Thus, the trap stiffness is a linear function with respect to the laser power applied after the objective:

$$P = \frac{k_{trap}(\Delta x)^2}{t} \quad (1.45)$$

where  $P$  is the laser power applied and  $t$  is time.

Key to optical trapping measurements is calibration of the trap. Multiple methods exist for calibration including: viscous drag calibration<sup>125</sup>, use of the equipartition theorem<sup>124</sup>, power spectral density fitting<sup>126–128</sup>, or more recently use of the Smoluchowski formalism and solution described above to analyze the distribution of displacements.<sup>41</sup> The first three methods will be developed here, whereas the Smoluchowski method is developed in Chapter 3.

The viscous drag method employs either precision flow or micromanipulation, such as a piezoelectric stage, to cause displacements from the trap center with a known velocity. Assuming the viscosity, particle size, and flow rate are known, the trap stiffness can be calculated by equating 1.42 to the force due to viscous drag:

$$F_{trap} = k_{trap}\Delta x = F_{drag} = u\zeta = u6\pi\eta R_{particle} \quad (1.46)$$

Thus, the particle displacements can be measured and the trap stiffness calculated. In the case of the other three, a static trap is employed and the particle undergoes Brownian motion within the trap. The movements are tracked and a distribution is created.

In the equipartition theorem, a distribution of displacements from trap center is created in the form of a histogram, which is then fit with a Gaussian. As above, the variance of the Gaussian fit is equivalent to the mean squared displacement. In this case, the deviations from center are due to the thermal molecular forces, equivalent

to Boltzmann's constant times the absolute temperature. Thus, the relation between the variance and trap stiffness becomes:

$$k_{trap}\sigma^2 = k_B T \quad (1.47)$$

This method tends to over-estimate the trap stiffness due to narrowing of the distribution based on the camera frame rate. The more rare and larger deviations from center due to thermal molecular collisions are therefore not recorded with the camera as if they did not exist resulting in the narrower distribution.

To eliminate the over-estimation by the equipartition method, we employ the other techniques. In the power spectral density method, the time-based deviation signal that we achieve through particle tracking is Fourier transformed into a frequency-based signal. The amplitude of the power at each frequency is based on the number of deviations from the center of the trap based on the thermal molecular collisions. At the point where the deviations stop, there is a cutoff or corner frequency where the deviations are no longer measured. To find this frequency, the power spectrum is fit with a Lorentzian type curve:

$$P = \frac{D}{f^2 + f_c^2} \quad (1.48)$$

where  $P$  is power,  $D$  is the diffusion coefficient,  $f$  is the frequency, and  $f_c$  is the cutoff/corner frequency. The cutoff frequency is correlated to the trap stiffness by:

$$k_{trap} = 2\pi\zeta f_c \quad (1.49)$$

This is similar to the viscous drag calculation described above; however, the displacements ( $\Delta x$ ) and velocity ( $u$ ) are now reflected in the cutoff frequency.

The discussion to this point illustrates no wavelength dependence of the laser source. In other words, any coherent laser source with high enough intensity and a Gaussian profile can therefore be used to create an optical trap. This is in fact true; however, the sample to be measured upon may indicate a wavelength dependence as well as dictating the optics to be used such as the objective. As our work focuses on use with biological specimens, the potential for optical damage is of concern. Damage occurs when the sample begins to absorb too much of the energy causing it to heat up. There is a finite window where minimal damage occurs when working with biological cells. This window occurs between the region where proteins absorb in the visible range and water absorbs in the near infrared and infrared ranges. This is sometimes termed the water window and occurs between  $\sim 750\text{-}1200\text{nm}$ .<sup>125,129</sup> Biological samples are relatively transparent within this region meaning most of the source is transmitted through the sample minimizing absorption and the potential for damage. Nonetheless, this photodamage can happen at any wavelength with a large enough intensity to cause physical heating of the sample. Thus, the power of the laser should be minimized in any biological sampling to minimize influence of cellular damage on the overall measurements being made. This is important to the work done in both Chapters 2 and 3; however, the work in a living organism in Chapter 3 was more largely concerned with this potential for damage.

#### **1.4. IMAGE BASED SINGLE PARTICLE TRACKING**

---

In all forms of microscopy reported, a camera is being used to record images. An image must be collected as the form of data for analysis. Although forms of particle

tracking exist that eliminate the need for image-based tracking, the collection of images is still necessary for structural information on the sample and provides a compounding dataset for later comparison. In this work, all tracking is achieved through an image-based analysis of single particles. In the optical tweezer microscopy, the particles are either single beads or single cells being tracked by an image registration process on white light images. Contrary to white light is the fluorescence signal used in TIRF-M that produces multiple single particle signals per image that can be tracked via a 2D Gaussian fit in conjunction with probability models to connect trajectories. These two methodologies are further described below.

#### ***1.4.1. IMAGE REGISTRATION METHODOLOGY***

---

The full process specifically used in our work is described in the later chapters. The common underlying factor between the 2D vs 1D methodology used in Chapters 2 & 3, respectively, is the use of cross correlation of the phase to determine the shift between images. The process of cross correlation is simply a convolution of the two signals. By definition, a convolution is simply the multiplication of the two fourier transformed signals:

$$\mathcal{F}(f * g) = \mathcal{F}(f) \cdot \mathcal{F}(g) \quad (1.50)$$

Upon multiplication of the two signals, the inverse fourier transform of the result will provide a signal containing information on the shift between the two signals. This information is found in the position of the maximum of the two convoluted signals. The signal being discrete as opposed to continuous, however, will bias the real maximum towards a discrete value, which manifests itself in the form of pixel bias.

Thus, the shift will be found in terms of full discrete values simply by using a max value algorithm.

Higher subpixel accuracy can be achieved by applying various fitting algorithms around the max value.<sup>130</sup> As the max value typically has a binomial type appearance, a simple Gaussian or sinc fit can be used to achieve higher accuracy in locating the maximum. There is a limit, however, to the accuracy that can be achieved with either of these methods that is dependent on the amount of data found within the discrete points. In other words, the number of points being fit will limit the accuracy of the fit.

A method to find higher subpixel accuracy is achieved through a simple upsampling algorithm.<sup>131</sup> Upsampling algorithms use the discrete values available to create a pseudosignal of calculated values between the known discrete points. In other words, a higher number of discrete points to fit in finding the maximum is created based on prediction algorithms. This is typically achieved with algorithms such as nearest neighbor, linear, or cubic spline interpolations. In nearest neighbor interpolation, the calculated values between discrete values will attain a value of the discrete value nearest to it. Linear interpolation, however, uses simple line fitting between discrete points to regress the points being calculated. Cubic spline interpolation takes this a step further and uses a cubic polynomial fit to the discrete values to calculate the theoretical values between.

Based on these brief descriptions, it becomes evident that the highest level of accuracy, i.e. least algorithm error, can be achieved through cubic spline

interpolation, however, this comes at the expense of computation time. There is an inverse relationship that exists between accuracy and speed. In our case, none of the analysis is done in real time. Thus, speed is not a necessity, whereas higher accuracy in particle tracking is critical to single particle measurements. Therefore, we have targeted efficient algorithms that enhance subpixel accuracy. Those algorithms are described in depth in their respective chapters.

#### ***1.4.2. HIGH RESOLUTION FLUORESCENT PARTICLE TRACKING***

---

The benefit to fluorescence imaging is the elimination of background noise. The individual particles themselves are imaged providing higher resolution of the overall structures. Individual fluorophores can be localized with higher precision assuming they are not in close proximity to each other. The proximity that two molecules can be is dependent upon the wavelength emitted by the Rayleigh criterion<sup>132</sup>:

$$d = \frac{\lambda}{2NA} \quad (1.51)$$

where  $d$  is the distance between particles,  $\lambda$  is wavelength, and  $NA$  is the numerical aperture. Assuming GFP is the particle, the emission wavelength is centered at 509nm, which gives ~175nm with a 1.45 NA objective like used in our experiments. Clearly, this resolution is limiting when many particles are being imaged; however, if the number is reduced, then the probability of finding two particles within close proximity is also reduced (refer to the earlier described diffusion equations). Furthermore, limiting the imaging to planes closer to the detector, i.e. near field, also enhances the resolution by eliminating more particles from detection throughout the

sample. It reduces the background noise allowing for larger signal detection and better localization. This is the most basic principle of super-resolution imaging.

By limiting the particle number, we enhance the particle tracking. A particle can be localized with high accuracy based on its point spread function, which is characteristic of the microscope being used. The point spread function can be tracked with image registration as previously described; however, the point spread function of a single source, or single fluorophore, will highly resemble a Gaussian. Thus, the center of the fluorophore can also be found highly accurately and extremely quickly with a simple 2D Gaussian fit.<sup>133</sup> This is a much simpler model to implement with little drawback comparative to image registrations techniques.

Particle tracking over time is achieved by applying probability models with a minimum step length between successive frames based on the random walk model. Thus, trajectories are connected over time for several particles enabling the imaging of an ensemble as opposed to a true single particle experiment like described with the optical tweezers above. More information can be obtained from the field of view that is being imaged. This is the basic principle behind the particle tracking used in Chapter 4 to track synthetic proteins fluorescently tagged on a synthetic lipid bilayer.

## 2. CHAPTER 2: MEMBRANE FORCE SPECTROSCOPY ON LIVING HELA CELLS<sup>1</sup>

---

---

### 2.1. INTRODUCTION

---

---

Measurements of cellular membrane properties are by no means a new concept. A variety of measurements have been performed with tools including optical tweezers<sup>86,124,125,134–148</sup>, magnetic tweezers<sup>149–155</sup>, atomic force microscopy, cell traction force microscopy<sup>86,156–159</sup>, micropipette aspiration<sup>68,160</sup>, scanning electron microscopy<sup>161–163</sup>, and microfluidic devices.<sup>164–170</sup> In all cases, a form of microscopy is used either directly or in conjunction with the technique being applied. Furthermore, each tool directly benefits the measurements being performed. Specifically, optical tweezers can apply a broad force range over a femtonewton to nanonewton scale. This broad force application is dependent on the laser power applied, which can be varied with a high degree of accuracy. Moreover, optical tweezers can be implemented with an optical microscope, a high numerical aperture objective, the proper laser source, and necessary optics to direct the beam through the back aperture of the objective to create the focused trap. The simplicity of this design has enabled use in a broad range of environments, including the high school classroom.<sup>171</sup>

---

<sup>1</sup> Statement of Work: Optical tweezers measurements and data analysis were performed by Bryce Schroder. Image based particle tracking algorithms were modified by Bryce Schroder from those provided by Dr. Cees Dekker's laboratory. HeLa cells were kindly provided by Dr. Jim Bamberg's lab and frozen stocks were created by Bryce Schroder. Dr. O'Neil Wiggan performed molecular biology associated with RNA silencing for membrane blebbing measurements. Work related to membrane blebbing is published in Nature - Scientific reports.<sup>191</sup> Link: <https://www.nature.com/articles/srep40953>.

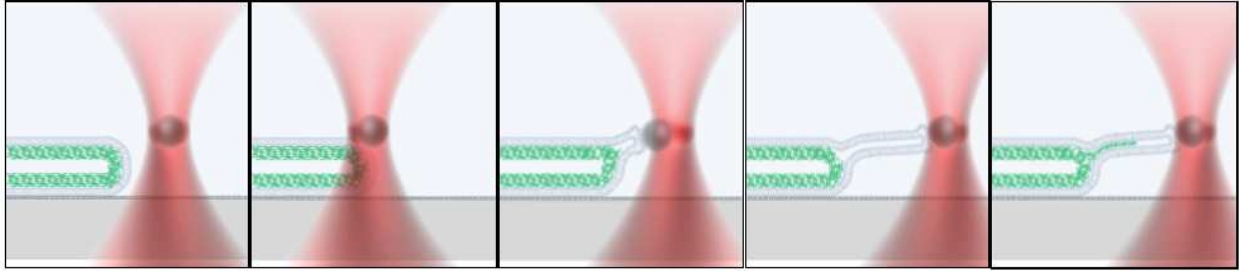


*Figure 2.1 Time based evolution of a tethering experiment. A) Bead positioned near a cellular edge. B) Bead pressed against the cell allowing for membrane attachment. C) The bead is pulled from the cell reaching a maximal force prior to reshaping of the tether attachment at the membrane. D) After the tether reaches maximal displacement and a reshaping event occurs, the bead moves closer to trap center at a lower tethering force that is constant, known as the plateau tethering force. E) Theoretical representation of tether filling with polymerized actin upon being held statically.*

Although the simplicity of the design lends itself to the novice user, the complexity of the experiments performed with optical tweezers have far exceeded the expectation of Arthur Ashkin when he originally developed the concept at Bell Laboratories.<sup>172</sup> Tweezers have been utilized in measuring molecular motor forces<sup>40,173–176</sup>, enzymatic catalysis/polymerization<sup>141,177–179</sup>, protein folding/unfolding characteristics<sup>141,151,152,180</sup>, cellular membrane tension<sup>86,124,134,136–138,140,145–147,154,181–183</sup>, and cytoskeletal properties.<sup>148,154,178,184,185</sup> Specifically, a large amount of this work has aimed at relating measured biophysical forces to cellular properties controlling membrane cortical tension and cytoskeletal organization.

One such methodology includes the pulling of tethers via an attached bead from the cellular surface. Simply, a bead can be roughly positioned near the surface with an optical trap (Fig. 2.1a). A precision micromechanical device, such as a piezoelectric stage, is then utilized to push the bead against the cellular membrane allowing adhesion followed by application of a constant pulling force away from the cellular surface creating a tether composed primarily of cellular membrane (Fig. 2.1b-d). Tethers however can also possess cytoskeletal structure through the formation of

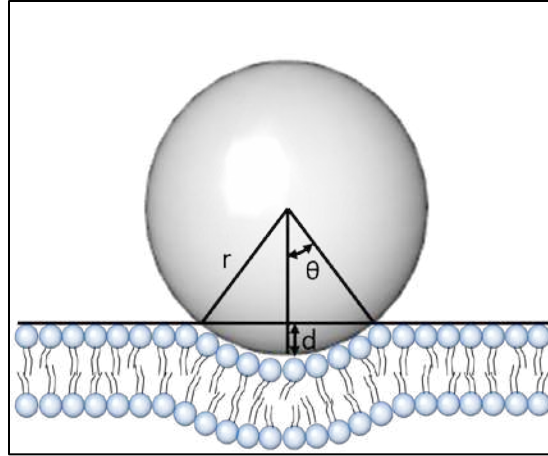


Figure 2.2 Bead penetration into the membrane is a function of bead radius ( $r$ ), the angle of penetration ( $\theta$ ), and the depth of penetration ( $d$ ).

polymerized actin within the tether itself (Fig. 2.1f).<sup>138</sup> Additionally, a balance between the molecular composition of the membrane and cytoskeletal structure exists that directly impacts the force values obtained.

Regardless of the values obtained, tether measurements are not trivial. A variety of factors influence the force response of a tether pulled from a cellular surface. More obvious factors include the elasticity of the membrane and its adhesion to underlying cytoskeletal structures. However, less obvious influences include bead penetration into the membrane (Fig. 2.2), number of membrane adhesion points, and velocity of tether pulling.<sup>138</sup> Furthermore, the cell type, stage in cellular life cycle, and underlying measurement matrix, i.e. the cytoskeleton and cytoplasmic contents, will also influence the tethering force applied. Cells also possess the ability to respond to external stimuli by resisting force application (a stiffening response), cleaving the membrane to sever the tether, and breaking the bonds between beads and the associated proteins.

Despite the difficulty presented, a large amount of cellular specific identifying information has been identified through optical tweezers experiments. Particularly, optical tweezers have been used to categorize membrane properties of various cell types<sup>124,135,136,145,147</sup>, differences between cancerous and non-cancerous cell lines<sup>142,157</sup><sup>186</sup>, stages in cellular life cycle<sup>136</sup>, and membrane tension forces associated with programmed cellular death<sup>147,187,188</sup>, or apoptosis. Here, the work is presented to obtain specific cellular information related to HeLa cells, a cell line derived from cancerous uterine tissue of Henrietta Lacks in the 1950s.<sup>189</sup> Specifically, our work aimed initially at corroborating previous tethering forces on HeLa cells<sup>136</sup>, thereby validating our system. Upon validation, information related to tethering velocity and the tethering force, as well as the viscoelastic response of pulling and returning multiple tethers from the same cellular adhesion point at varying speeds was targeted. We then induced bleb formation on the HeLa cell surface through the RNA based silencing of both cofilin (Cof) and actin depolymerization factor (ADF), which have been shown to competitively inhibit myosin II activity on actin filaments associated with maintenance of both cellular and nuclear architecture as well as internal cellular pressure.<sup>190,191</sup> This work collectively has provided insight into the functional relationship between the membrane and its underlying cytoskeletal structure. Furthermore, we have identified a novel method of bead tracking utilizing image processing techniques in conjunction with a Hough circle transform enhancing bead center localization in difficult to track bead environments.

## **2.2. MATERIALS & METHODS**

---

### ***2.2.1. SURFACE PREPARATION***

---

Cells were cultured in 30 mm glass bottom culture dishes purchased from Mattek. Uncoated glass surfaces provided weak cellular adhesion for culture and measurement. To counteract this problem, the surfaces were treated with 1M hydrochloric acid for an hour before rinsing with deionized distilled water. The surfaces were then passively coated with poly-L-lysine to enhance surface attachment and cell spreading following the protocol outlined in Appendix A-1.6.

### ***2.2.2. CELL CULTURE***

---

HeLa cells were obtained from Dr. Jim Bamburg's lab and frozen stocks were produced (Appendix A-1.2). Cells were planted from frozen in 100 mm tissue culture polystyrene dishes and cultured in Dulbecco's Modified Eagle Medium (DMEM) supplemented with 10% Fetal Bovine Serum (FBS). Cultures were incubated at 37°C in an incubator maintaining  $\geq 95\%$  humidity and 5% carbon dioxide. The cells were grown to greater than 80% confluence at which point the cells were split, or passed to the next round of culturing. A protocol for the plant and passage procedure can be found in Appendix A-1.3. Cells were maintained in this manner for the duration of experimental work.

At the point of experimentation, the cells were transferred into the poly-L-lysine coated 30 mm glass bottom culture dishes previously prepped. This "splitting" of cells occurred less than 24 hours prior to experimentation and multiple dishes were

setup at once. The 24 hour time period was chosen to allow the cells enough time to recover, spread, and grow naturally post chemical removal from the culture surface with trypsin, a protease typically found within the small intestine. Furthermore, the cellular density was kept low during the passage to minimize cellular divisions and maximize the cellular surface area for membrane optical tweezers measurements.

The cells were cultured overnight and experiments performed the next morning. Approximately one hour prior to experimentation the culture dishes were rinsed with sterile phosphate buffered saline (PBS) removing any cellular debris. Fresh 0.2  $\mu\text{m}$  filtered DMEM containing 20 mM Hepes was added following the rinse. Hepes acted to buffer the carbon dioxide concentration in the media by maintaining the carbonate concentrations. Carbonate acts to buffer the hydrogen ions in solution similar to that of our blood, thereby maintaining the pH. This enabled preservation of a neutral pH preventing dips that were killing the cells and reducing our measurement times.

Following the addition of fresh media, 1.7  $\mu\text{m}$  beads were added to the dish and a layer of mineral oil was overlaid gently on top of the DMEM creating a diffusion barrier slowing gas exchange. This methodology provided several hours of measurement time prior to the cells rounding up and undergoing programmed cell death, or apoptosis. At this point, a fresh dish was removed from the incubator, and prepped per the methodology just described. These methodologies extended experimentation times by several hours allowing multiple measurements typically unattainable in an open-air microscope environment.

### ***2.2.3. EXPERIMENTAL CELLULAR MODIFICATIONS***

---

The membrane blebbing force spectroscopy performed required cellular modifications to induce blebbing. These preparations were performed by Dr. O'neil Wiggan in Dr. Jim Bamburg's lab and provided to us for the force measurements. To induce membrane blebbing, an RNA silencing technique was implemented to knock down the expression of actin depolymerization factor (ADF) and cofilin (COF). These two proteins are thought to competitively bind to actin interrupting the amount of force myosin II can apply to the actin cytoskeleton. The competitive binding nature helps uphold a pressure sensitive homeostasis within the cell. When ADF and COF are silenced 24-48 hours prior to measurements, we ultimately see induction of membrane blebbing known to be caused by the increased myosin II contractile activity on the actin cytoskeleton.<sup>190</sup> This induction technique produced an ideal measurement environment where blebbing was prolonged and highly active across the culture dish. Furthermore, cells could continue to grow and divide regularly until blebbing started, which occurred in varying timeframes for different cells. Thus, multiple measurements could be performed on a variety of cells from the same dish.

### ***2.2.4. BEAD PREPARATION***

---

Uncoated 1.7  $\mu\text{m}$  polystyrene beads were purchased from Spherotech. The beads were subjected to a cleaning protocol prior to use (Appendix A-1.1). The procedure was carried out in 1.5 ml microcentrifuge tubes that had been pre-treated with acetone and heated drying at 80°C. This heat treatment process insures less binding to the tube surface enabling maximum recovery of beads between steps. A 1

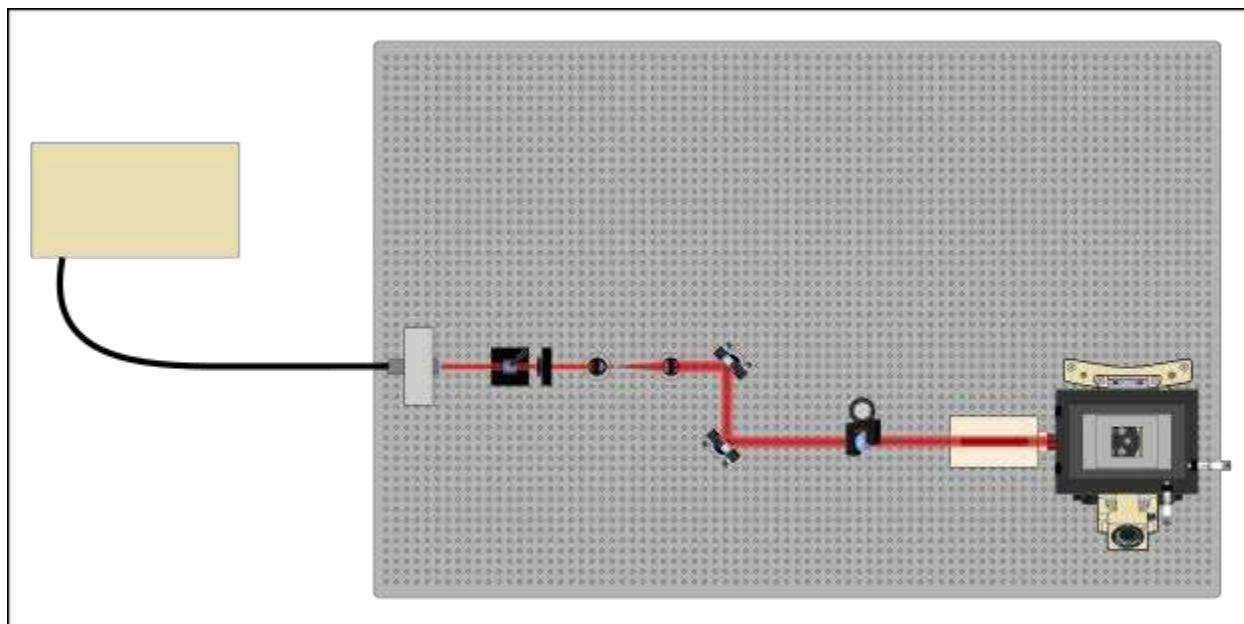


Figure 2.3 Illustration of home built optical tweezers setup. Collimated beam is passed through a polarizing beam splitting cube into a  $\frac{1}{4}$  wave plate for control of laser power. The beam is then expanded through a telescope to a diameter that will fill the back aperture of the objective at the microscope. The beam is steered into the side of the microscope via mirrors and a periscope arrangement.

ml volume of bead suspensions was transferred to the treated tube and pelleted at max speed in a desktop centrifuge for 30s. The supernatant was discarded and replaced with wash buffer. The centrifugation was then repeated twice in this buffer before resuspension in a storage buffer for later use.

### ***2.2.5. EXPERIMENTAL SETUP***

---

All experiments were carried out on a homebuilt optical tweezers setup (Fig. 2.3) comprised of an IX71 microscope with 1070 nm continuous wave Nd:YAG trapping laser (YLR-5-1070-LP, IPG Photonics, Oxford, MA) focused through a high numerical aperture objective (60X water immersion, 1.20NA; Olympus). Glass bottom dishes with a 0.17 mm, or No. 1.5, coverglass thickness were placed on a dish warmer (Warner Instruments) mounted to the piezo-electric stage. A single vertical beam trap was created and focused through the sample enabling bead trapping. Manipulations

were performed utilizing a manual XY positioning stage for rough position. Fine positioning and precisely controlled movements were carried out by a three-axis piezo-electric stage (Nano-PDQ350, Mad City Labs Inc., Madison, WI). The sample was illuminated from above with white light and images of cellular manipulations and associated bead displacements were recorded on a monochromatic CCD camera (acA1300-30gm, Basler AG, Ahrensburg, Germany) mounted below the sample.

## ***2.2.6. OPTICAL TRAP CALIBRATION***

---

### ***2.2.6.1. VISCIOUS DRAG CALIBRATION***

---

Optical trap calibration was performed using a viscous drag method. Beads were trapped and moved to an isolated area away from any cells. The beads were then moved away from the glass surface to eliminate frictional effects introduced by the no slip boundary condition. A height of ~10 microns was found to be sufficient to eliminate these effects. A triangular waveform was applied to the piezo electric stage via a custom written Labview code (National Instruments, Austin, TX). The velocity of the displacement was varied collecting multiple displacement information on each bead. This protocol was repeated for multiple power levels to obtain the overall trap calibration as a function of laser power. Bead displacements were recorded on the CCD camera for image-based tracking described in detail below. Bead positions with respect to time were plotted and the peak-to-peak displacement measured. The displacement from trap center ( $\Delta x$ ) was measured as half the peak-to-peak displacement. Using the displacements from center and the applied velocities, the trap stiffness can be found from a force balance relationship. The viscous drag force

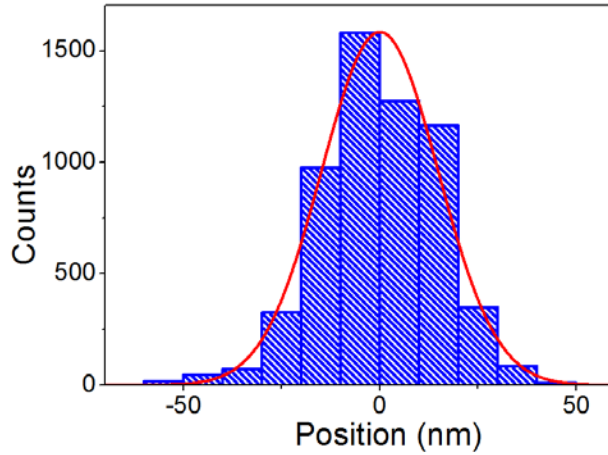


Figure 2.4 Histogram of bead displacements illustrating a gaussian distribution and fit.

is set equivalent to the force of a particle trapped within a harmonic as was discussed in Chapter 1 (Eq. 1.47). This balance gives trap stiffness,  $k_{trap}$ , from known variables.

#### 2.2.6.2. *EQUIPARTITION THEOREM*

---

A secondary method employed for calibration included the use of the equipartition theorem. A bead was trapped statically, and under these conditions, images of bead positions were collected. Images were tracked, and the bead positions placed into a histogram of displacements from the trap center (Fig. 2.4). The histogram was fit with a Gaussian curve, and the variance of the Gaussian fit was correlated to trap stiffness with the following equation (a play off the Einstein relation):

$$k_{trap,x} = \frac{k_B T}{\sigma_x^2} \quad (2.52)$$

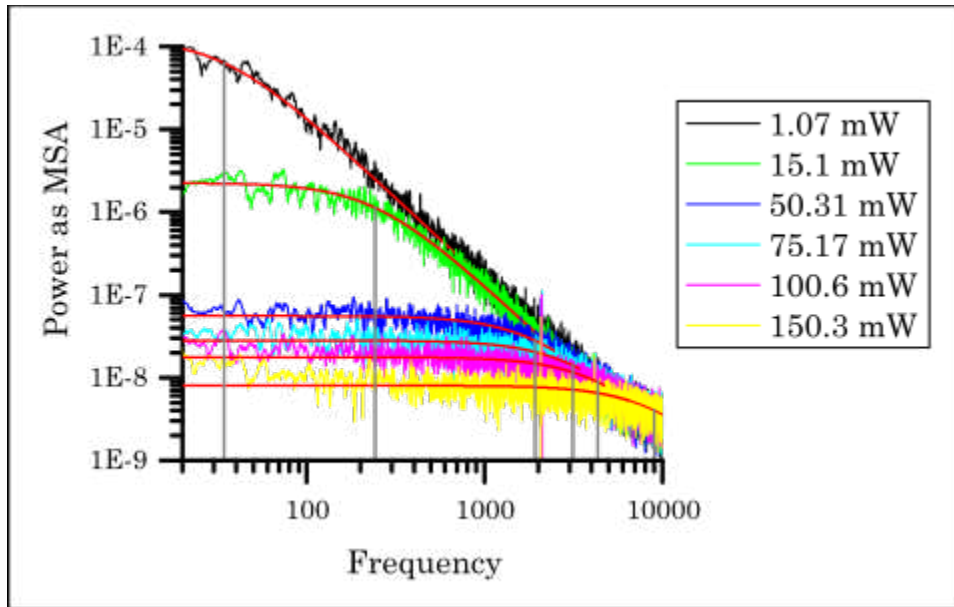


Figure 2.5: Power spectral analysis of a trapped bead at varying applied laser powers. Red lines indicate Lorentzian fits. Gray lines indicate resulting cutoff frequencies.

### 2.2.6.3. POWER SPECTRAL ANALYSIS

---

The final method used to estimate the trap stiffness was the power spectral analysis method. As with the equipartition method, a bead was statically trapped and images with positional data recorded. The time dependent positional data was extracted using the bead tracking algorithm described below, and a fast Fourier transform was applied to the extracted waveform. This was then used to create the power spectrum in the frequency domain (Fig. 2.5). The data was then fit with a Lorentzian curve using Equation 1.49. The trap stiffness was then inferred from the cutoff frequency (Eq. 1.50). This method required knowledge of values for viscosity and particle size. For our purposes, the viscosity was assumed to be that of water at 25°C ( $8.90 \times 10^{-4}$  Pa·s), and particle size was that of the bead radius, or 0.85  $\mu\text{m}$ .

### ***2.2.7. MEMBRANE TETHER FORCE SPECTROSCOPY***

---

In tethering experiments, the prepared dishes containing HeLa cells were placed on the tweezers setup as described. Beads were introduced into solution at a 1:10,000 dilution from stock concentration and allowed to settle for 10-15 min prior to experimentation. This bead density was found to be ideal for preventing crowding while enabling quick bead discovery for experimentation. After settling, tethering experiments were performed. A cell was located illustrating a spread, non-mitotic, or flattened morphology and a bead was trapped peripheral to the cell boundary. Upon trapping, the bead was manually positioned near the edge of the cell just above the glass surface. At this point, image recording started and the bead was gently pressed against the cell surface using the piezoelectric stage. It was held in this position for 5-10 s providing enough time for membrane attachment to the bead surface. The bead was then pulled away from the surface at a rate of 7.6 nm/s. The rate chosen was comparable to the rate of actin polymerization in forming filopodia, much slower than typical tweezers experiments.<sup>138</sup> This rate was chosen to determine if actin polymerization could be artificially induced through tethering experiments in conjunction with measuring membrane cortical tension.

A tether was pulled away from the cell surface for a distance of 10  $\mu\text{m}$ . At this point, the tether was held for variable timeframes prior to release. At the time of release, the tether response was recorded over the response time and imaging ceased. A full elastic response was indicative of a purely membrane tether, whereas a partial

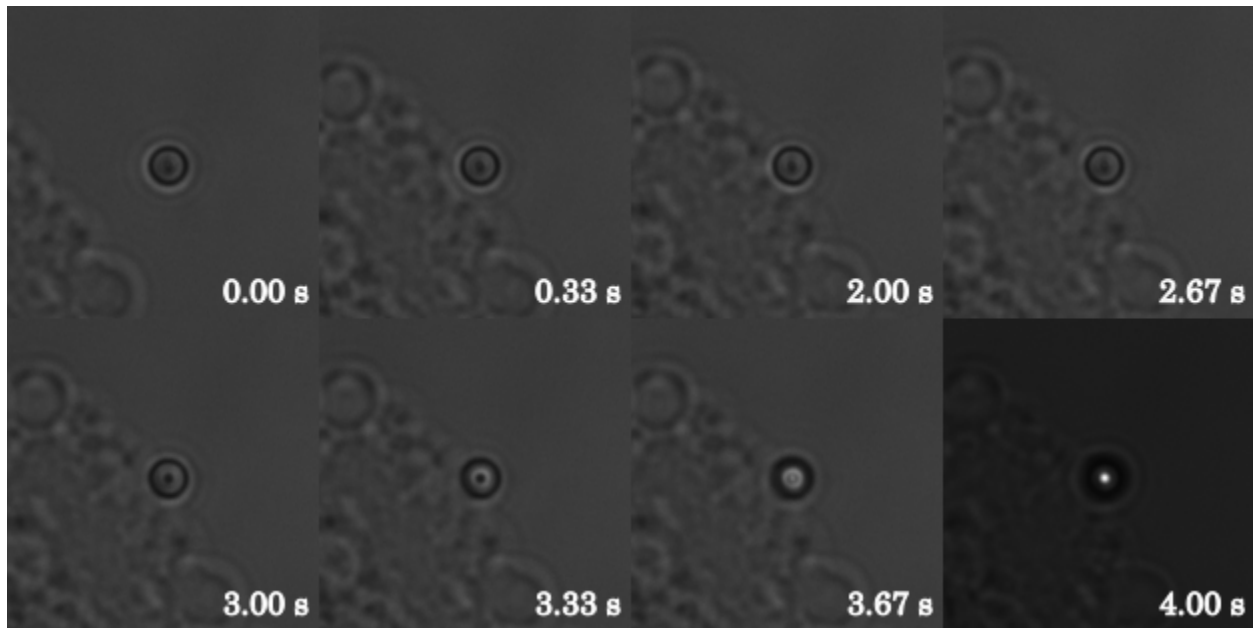


Figure 2.6: Time-lapse images of a single bleb measurement. The top frames illustrate positioning of the  $2\ \mu\text{m}$  bead near the blebbing cell. Lower images illustrate displacement of the bead upon bleb formation.

elastic to no response was indicative of cytoskeletal structure being formed. The longer the bead was held, the less response expected.

### ***2.2.8. MEMBRANE BLEBBING FORCE SPECTROSCOPY***

---

Membrane blebbing experiments were performed identically to the tethering experiments just described. However, no pulling was necessary to measure the blebbing forces. Similarly, blebbing forces induced a displacement from trap center with an associated force; however, the forces inducing displacement were pushing as opposed to pulling. Furthermore, the formation of blebs on the cellular surface was randomly distributed. Thus, determining where a bleb would form was arbitrary. It was however noticed that blebs formed in areas consistently over periods of time. Hence, areas that illustrated higher structure (i.e. less bulbous protrusions) where blebs had formed and retracted were targeted as future blebbing sites. This technique enabled prediction of future blebbing sites with a fair degree of accuracy; however,

random particle positioning at the cellular surface may have been adequate for the work as well.

To measure the bleb forces, a particle was positioned at the cellular surface similarly to the tethering experiments while images were being recorded (Fig. 2.6). Rather than pushing, the bead was held near the cell initially to ensure a zero-force starting point. The trap was held static from this point throughout the entire bleb force measurement. Once bleb expansion ceased, a tether force measurement was performed to measure the cortical tension of the bleb as well. This measurement was performed as described in the tethering section.

#### ***2.2.9. MEMBRANE VISCOELASTICITY FORCE SPECTROSCOPY***

---

Membrane viscoelasticity measurements followed the same initial protocol of bead tethering experiments. Beads were trapped and positioned near the surface. Image recording was initiated followed by tether formation utilizing the piezoelectric stage. After tether formation, the experiments differed in the velocity profile applied to the formed tether. Rather than a single constant pulling velocity out to a static position at 10  $\mu\text{m}$  from the surface, a triangular pattern was applied over the 10  $\mu\text{m}$  distance, thus returning the bead to the tether start position. This was done to each tether for 5 different velocities and the bead response recorded throughout. A short wait period of 30 seconds was applied between each velocity to minimize cellular responses from the previous cycle. This method enabled us to find the response of the membrane to varying force application and the memory the membrane had to each successive force application.

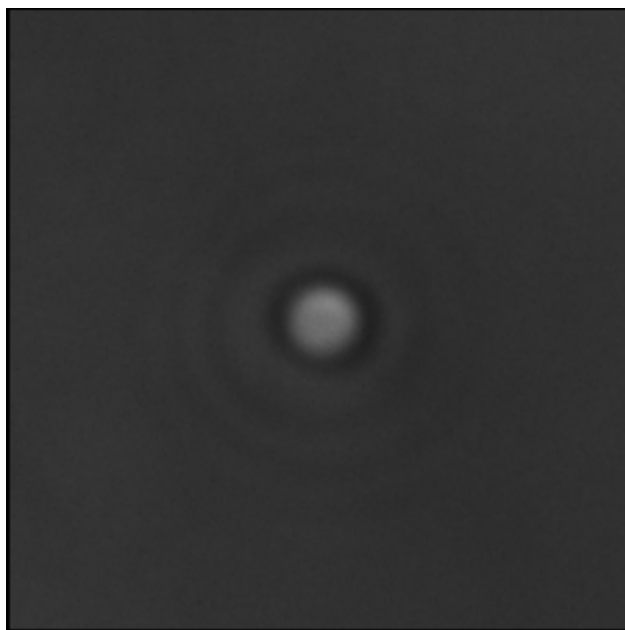


Figure 2.7 Airy disc pattern illustrated by light refraction through a polystyrene bead.

## ***2.2.10. BEAD TRACKING***

---

### ***2.2.10.1. TWO-DIMENSIONAL BEAD TRACKING***

---

Image-based particle tracking was accomplished through an image registration process based on an autocorrelation algorithm. The algorithm varied dependent on the experimental images collected. In simple bead tracking, the beads illustrated a nice airy disk pattern of concentric circles with alternating light and dark regions created from the interference pattern of the scattering bead (Fig. 2.7). This pattern was simple to track, as a center of mass (COM) could roughly locate the bead center from the intensity pattern providing an initial starting location for the autocorrelation function. The autocorrelation then used the COM to focus a tighter window around the rough bead center. This window was then registered upon itself.

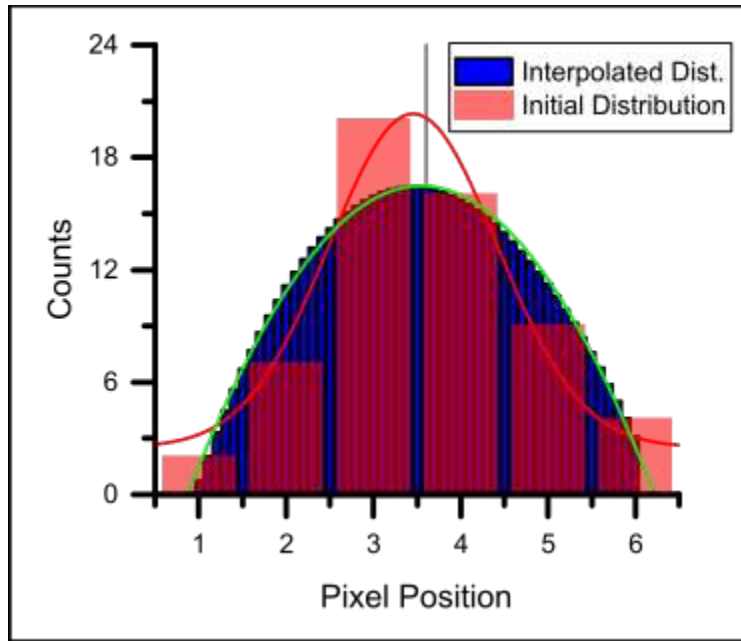
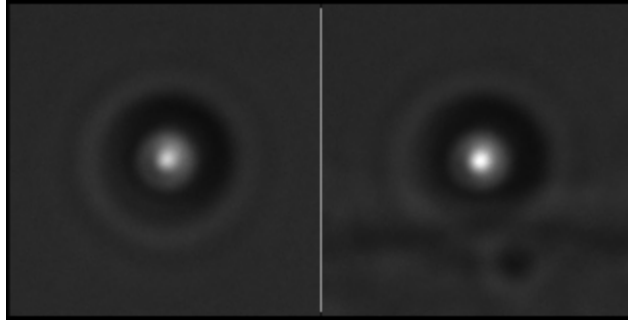


Figure 2.8: Illustration of a theoretical intensity distribution that has been fit to a center of mass (grey line) and a gaussian followed by bicubic spline interpolation and a second gaussian fit. The interpolation smooths the distribution and provides more points to fit yielding a higher level of accuracy in center localization.

Autocorrelation involves the same process as cross-correlation; however, rather than registering an image against a reference, the image is registered against itself. The cross-correlation process is simply a convolution of two images in the frequency domain. In other words, a 2-D Fourier transform is applied to each image and then their frequencies are multiplied against each other. The convoluted image then undergoes 2-D inverse Fourier transformation producing a distorted image with an intensity maximum. The location of the intensity maximum correlates to the maximum likelihood position of the two image patterns intersection. Furthermore, this maximum is Gaussian distributed, and thus the peak can be fit with a parabolic function to find the center to higher sub-pixel accuracy. Dependent upon the camera resolution and pixel size, typically sub-10 nm accuracy can be achieved with this method.



*Figure 2.9 Illustration of cellular effects (right) on airy disc pattern of the same bead in solution (left).*

For our work, the accuracy cross-correlation alone could attain was inadequate. This was due to pixel bias, which influenced the tracked position (Fig. 2. 8). To counteract pixel bias, an up-sampling algorithm was implemented using a bi-cubic spline interpolation technique.<sup>131</sup> This created a pseudo-high-resolution image with a greater number of pixels, which enhanced the particle center localization by providing a larger number of points for the parabolic fit (Fig. 2. 8). In other words, it artificially filled gaps between the original points increasing the precision of the fit. Conversely, this decreased pixel bias that was limiting precision.

In the cellular work, simple bead tracking worked well when away from the cellular surface; however, distortion of bead patterns occurred when the bead approached the cellular surface (Fig. 2.9). This distortion pattern was due to the influence of intensity patterns of the cell and its contents. As the pattern distorted, this biased the COM calculation away from the bead center. Although these effects influenced COM measurements, the ring pattern characteristic to the bead seemingly remained. Thus, a circle tracking algorithm was sought to more accurately find the initial bead center location. Simple circle detecting algorithms innate to Labview, however, lacked the ability to find such patterns in the intensity images. Thus, a

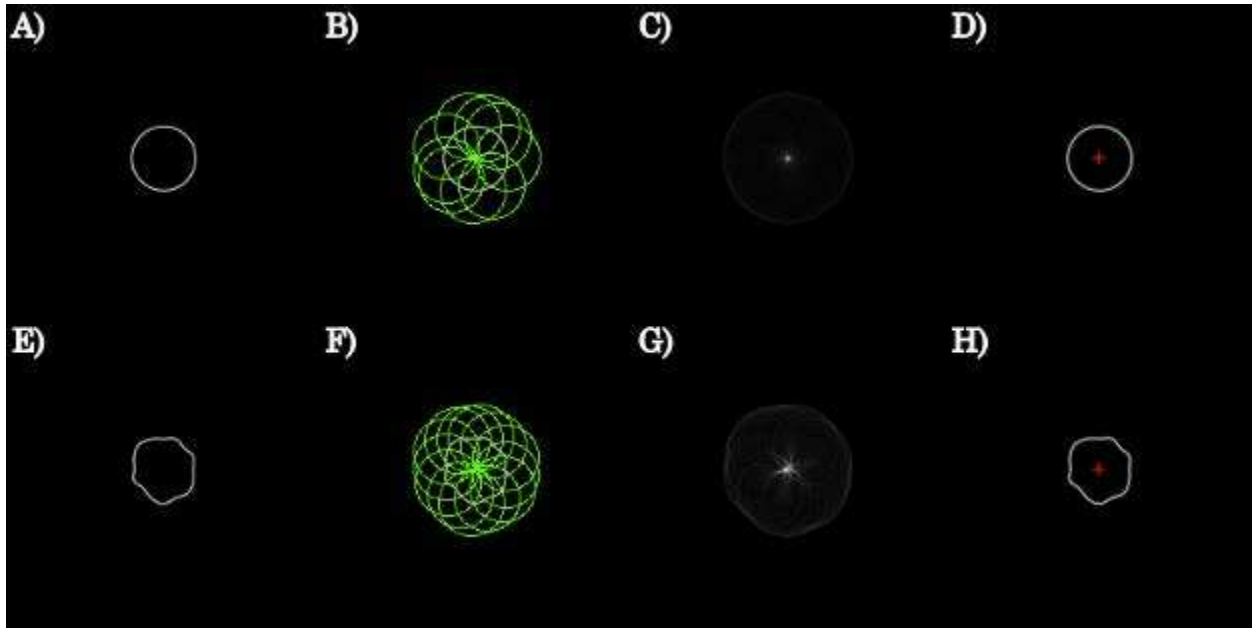


Figure 2.10: A) Initial circle. B) Overlaid circles from the Hough Circle transform. C) Intensity distribution by summing all circles in transform. D) The center point of the circle is localized. E-F) Same process applied to a distorted circle.

custom circle detection algorithm was implemented utilizing the Hough circle transform.<sup>192</sup> This algorithm uses the edges of a circular pattern of pixels by drawing circles around each pixel. A single count is added to each pixel location as each circle is drawn around each point on the boundary (Fig. 2.10a). This creates an intensity distribution around the center of the circle with the maximal intensity correlating to the circle center (Fig. 2.10b).

The hough circle transform only works well when the edges of the circle are well defined and easily found, which was not the case in our images (Fig. 2.11). A simple watershed applied to the image provided the edges of the circle better than edge detecting algorithms, yet was not adequate to prevent the detection of unwanted semi-circular shapes. Thus, Gaussian blurring was implemented to smooth the image intensity profiles decreasing the pathways the watershed algorithm could find based

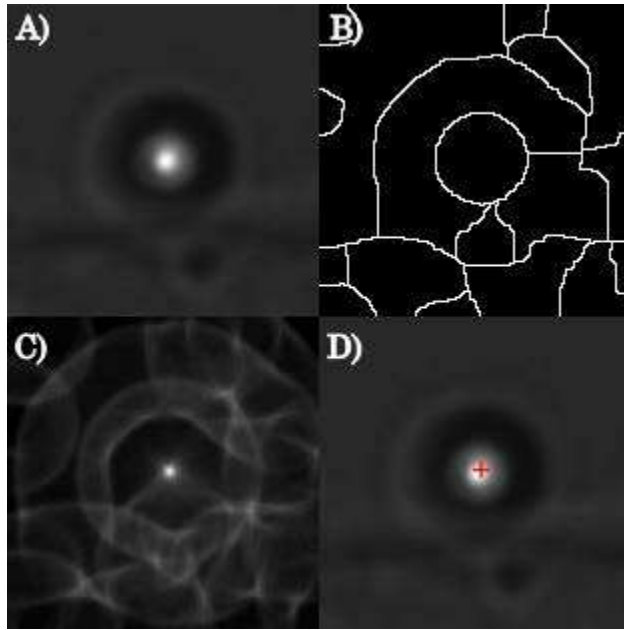


Figure 2.11: Application of the Hough Circle Transform on experimental data image. A) Initial bead image. B) Watershed of blurred image shown in A). C) Hough Circle transform of watershed image. D) Localized center intensity for input into cross-correlation algorithm.

on intensity differences. After applying the watershed in this manner, the circular edges remained while many of the other false patterns disappeared.

The Hough transform was then applied producing the intensity distribution described above. A simple thresholding applied at 0.75 times the maximum intensity provided the central intensity points (Fig. 2.11). A COM localization was then employed upon the central intensities providing an accurate estimate of bead center position in a complex image pattern. The up-sampled autocorrelation function was then applied in the same manner already described based on the center position found in this manner.

### 2.2.10.2. THIRD DIMENSION Z-AXIS TRACKING

Tracking in 3-D was achieved using a z-axis look-up table (ZLUT). The ZLUT table was created by applying a step waveform in the z-axis to the piezoelectric stage



*Figure 2.12 Intensity illustration of Z axis Look Up Table (ZLUT). Horizontal pixel lines illustrate radial intensity distribution of a single bead at multiple Z positions. The focal plane is when the bead intensity changes from light to dark.*

at 10nm intervals to a dish with beads immobilized on glass. A total distance of 10  $\mu\text{m}$  was covered, i.e.  $\pm 5 \mu\text{m}$  from the focus. Images were continuously recorded at 30 fps throughout the waveform application. Areas for recording were chosen with multiple beads. The choice to record multiple beads was due to the variability found in bead radius as provided by the manufacturer. Bead radius is Gaussian distributed around a standard value, 1.7  $\mu\text{m}$  in our case. Thus, areas with the highest variability in bead pattern correlating to variations in bead radius were sought for producing the ZLUT. This was done to ensure the ZLUT reflected a wider variety of intensity distributions for comparison to those produced in experimental samples. This reduced the level of error by providing a distribution of profiles representative of the bead radii distribution for tracking each experimental bead.

The ZLUT was created through the same image registration process used for 2-D tracking. The center of the bead pattern was localized followed by creation of a radial profile around this point for each image within the stack (Fig. 2.12). The radial profiles created from images within a single step of the waveform were averaged against each other providing an average profile for each 10 nm point along the z-axis. The radial profiles were then entered into a 2-D array with the correlating location

in  $z$  found in the first column (Fig. 2.12). A 2-D array was created for each bead within the image, thus creating a 3-D array containing the ZLUT information for multiple beads.

Tracking with the ZLUT was implemented after experimentation. Recorded images were tracked with the 2-D cross-correlation algorithm. The creation of a radial profile followed as above; however, the profile was not stored in an array. The profile was registered in 1-D against the radial profiles for each bead in the ZLUT. The highest level of correlation was found for each bead creating an array of axial localizations. This array of axial localizations was saved in conjunction with the XY tracking data for each image creating a 2-D array of tracked data containing the XY center localizations as well as localization in  $Z$  for each bead profile within the ZLUT. The axial profile illustrating the smoothest transitions with the most realistic curve and lowest level of noise was selected in each case. The 3-D data was then used to calculate the overall displacement from the trap center, which was directly correlated to force.

## **2.3. RESULTS**

---

### ***2.3.1. BEAD TRACKING ENHANCEMENT***

---

The resolution of particle tracking is critical to accurate force calculation. Obviously, the higher the resolution, the better the measurement. However, image-based tracking algorithms suffer from errors due to the inherent discrete sampling. Furthermore, the resolution is dependent on both the accuracy and the precision, which are measures of systematic error, or bias, and statistical error, or scatter,

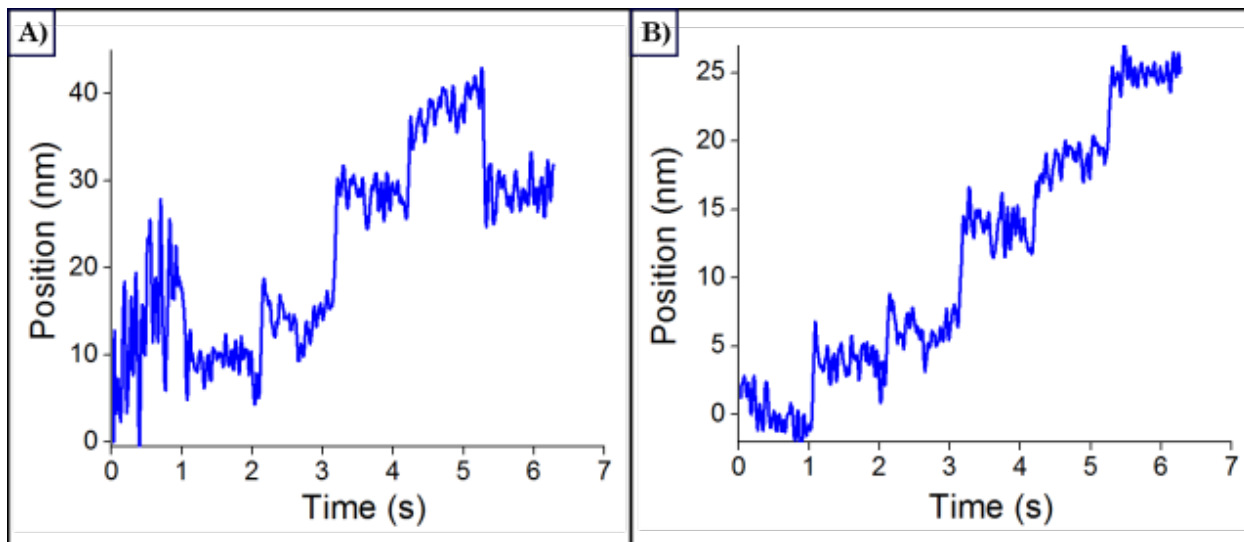


Figure 2.13: A) Initial tracking of 5nm steps with a standard cross-correlation algorithm. B) Tracking obtained after upsampling the initial data set.

respectively.<sup>193</sup> In sampling non-diffraction limited particles, where the wavelength is smaller than the particle radius, statistical error is typically lower due to high signal/noise ratio. Thus, the prominent error we see is that of pixel bias, which arises from the discrete sampling inherent to the camera sensor array. Each pixel intensity is an average of the intensity hitting the entire area of that pixel. At lower magnification a larger area is represented comparative to higher magnifications with bias being inversely related. However, sampling at higher magnifications to reduce the bias limits the area that can be imaged. Hence, the importance of accurate tracking algorithms becomes apparent.

Initially, the pixel bias of our system prevented us from achieving the sub-5 nm precision we were targeting (Fig. 2.13). We were limited to a precision of  $\sim 10$  nm, a value comparable to a COM algorithm.<sup>193</sup> This accuracy needed improvement. As we were already limited on magnification, an alternative solution was found. It was realized that the bias could be limited if the sample could be falsely magnified. In

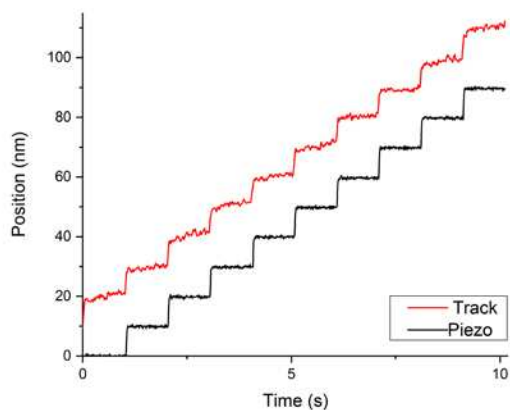


Figure 2.14 Z-axis particle tracking results illustrating clear differentiation of 10 nm steps.

other words, if the same image could be created with a larger number of computed pixels, increased accuracy could be achieved *in silico* without any changes to the experimental methods. This pseudo-magnification was achieved in Labview through a simple image up-sampling algorithm using bi-cubic spline interpolation creating a pseudo-high-resolution image. This technique enhanced the particle center localization by providing a larger number of points for parabolic fit to find the correlation maximum (Fig. 2.13).

Compounding the necessity for more accurate lateral (XY) tracking is the fact that the accuracy of axial (Z) localization is directly dependent upon the accuracy of XY localization. This dependency arises from the method of z localization. The use of radial profiles hinges upon accurate center localization, which produces an axis of symmetry that makes the radial profile equal in all directions. The radial distribution shifts slightly with deviations from center introducing errors, or a blurring in the profile. Thus, achieving higher lateral accuracy leads to higher accuracy in Z

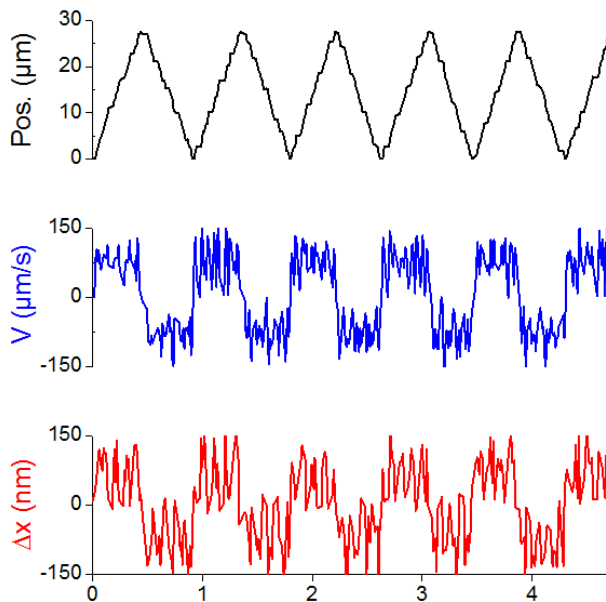


Figure 2.15 Viscous drag calibration of the trap via an applied triangle waveform (top) through the piezoelectric stage. The resulting stage velocity (middle) illustrates a square waveform that is translated into the bead displacement (bottom).

localizations. Utilizing these methodologies, a greater than 10 nm resolution was achieved along the Z-axis (Fig. 2.14).

### ***2.3.2. OPTICAL TRAP CALIBRATION***

---

Viscous drag calibration of the optical trap resulted in deviations from trap center that were recorded as a square wave pattern (Fig. 2.15). The constant velocities applied by the piezoelectric stage in a triangular wave pattern leads to constant displacements and the resulting square wave. The displacements seen are due to frictional effects of the medium that act as an opposing, or drag force on the trapped bead. The magnitude of displacement depends on the magnitude of the drag force as balanced with the trapping force within the harmonic potential. In other words, a force balance exists that reaches equilibrium with each side having its contributing factors. This is reflected in Equation 1.47, which was used to establish our trap

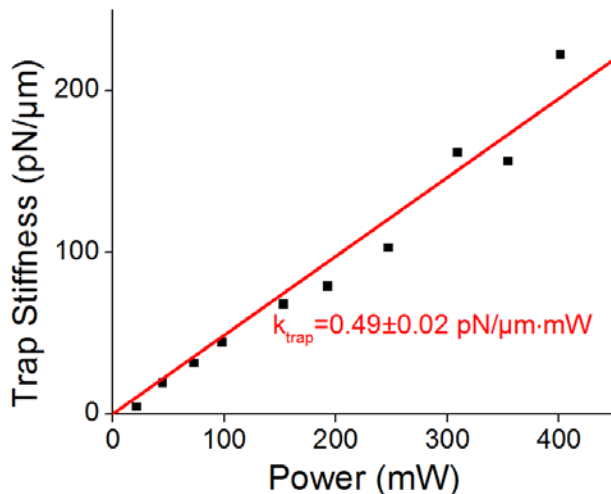


Figure 2.16 Trap stiffness as a function of laser power applied.

stiffness. Velocity was a known parameter directly applied through our triangular wave pattern. Displacement, however, was found through our particle tracking algorithm.

This methodology provided a trap stiffness of  $0.49 \pm 0.02$  pN/μm\*mW of laser power at the back aperture (Fig. 2.16). Furthermore, the expected linear relation with respect to power was achieved. These properties also held for the axial (vertical) trap stiffness, which was determined to be  $0.13 \pm 0.02$  pN/μm\*mW. Overall, these properties indicated the trap was within normal operating parameters and comparable to previously obtained values. Power spectral analysis corroborated these results.

### ***2.3.3. MEMBRANE TETHERING FORCES***

---

#### ***2.3.3.1. TETHERING EFFICIENCY***

---

As stated previously, a variety of factors influence tethering experiments. The effects of those factors can be minor without influencing measurements; they can be

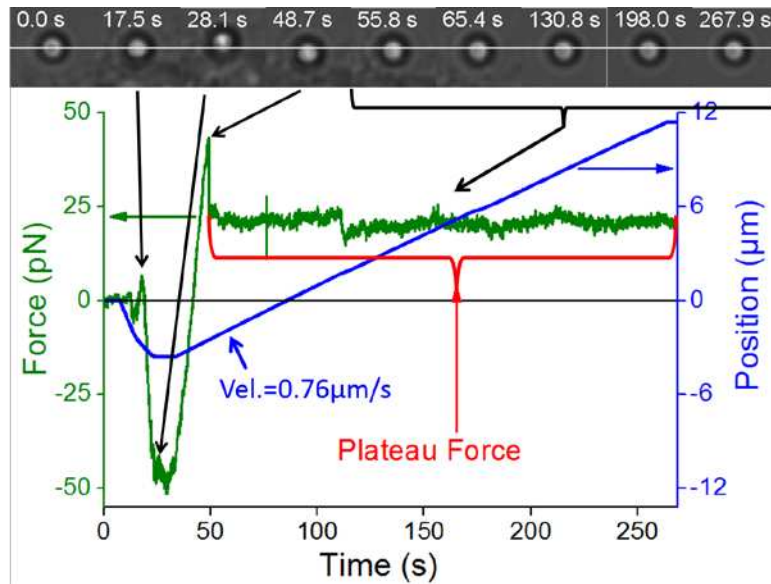


Figure 2.17 Force based tracking of a single membrane tethering experiment shown in green. The correlating piezoelectric stage movement relative to the optical trap is shown in blue.

characteristic leading to information about cellular properties; and they can be detrimental leading to invalid measurements. The latter directly impacts the measurements leading to a decrease in efficiency. Other groups have reported on factors influencing experimental efficiency, such as tether breakage and loss of bead adhesion.

### 2.3.3.2. *TETHERING FORCES*

Two different forces related to tethering were studied, a maximal tethering force and a plateau tethering force (Fig. 2.17). The maximal tethering force occurs right before an apparent breakage of bonds to the underlying cytoskeleton that precedes the plateau tethering force. The maximal force is thought to occur at a point prior to a tether restructuring, where the initial pulling pulls at the membrane in a manner like lifting a blanket from a single point creating a conical shape in the membrane as it pulls upward. Now imagine the blanket could modify its structure to

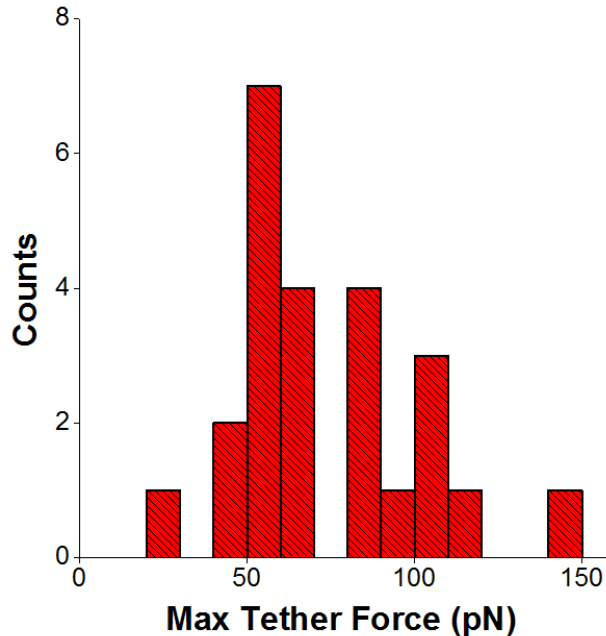


Figure 2.18 Histogram of maximum tether force illustrating a potential bimodal distribution.

where only the threads directly attached to that point are being pulled upward without disturbing the rest of the blanket. This would create a tubular structure containing less mass and a less strained conformation. This is similar to what occurs when the tether actually forms. Bonds holding the entire membrane to the underlying cytoskeletal structure are released around the bead attachment point allowing pulling of the membrane alone composed of freely flowing lipids. This allows the tether to form at a constant stretching force, or plateau force, until the reservoir of membrane lipids is exhausted. We did not extend beyond this reservoir exhaustion point in our experiments.

In our work, we found that the maximal tethering force illustrated a bimodal distribution (Fig. 2.18). It has been shown that the tethering force is dependent on the bead immersion angle into membrane, which directly correlates to the overall tether radius.<sup>138</sup> The distribution we obtained is most likely representative of the

immersion into the membrane based on step size movement with the piezoelectric stage. Thus, deeper immersion led to greater attachment to the membrane yielding larger radii tethers with greater tethering force.

The plateau force was found to be  $39 \pm 3$  pN for the HeLa cell measurements. Raucher and Sheetz had originally reported plateau forces of 14 and 40 pN for HeLa cells found in interphase vs metaphase, respectively.<sup>136</sup> Thus, hypothetically the experimentally measured cells existed primarily in metaphase of the cell cycle. However, as cells typically spend the most time in interphase<sup>194</sup>, this result is highly unlikely. Furthermore, the tether extraction rate of Raucher and Sheetz was nearly 400 times that of our experimental tethering rate. The tethering rate of Pontes *et al*<sup>138</sup>, the basis for this work, yielded a plateau force of 39 pN on mouse derived 3T3 fibroblast cells. Therefore, the more likely source of higher than expected plateau forces obtained can be attributed to the lower tethering rate. The lower rate thereby enabled a larger cellular response time, which increased the viscoelastic forces from the membrane. These higher viscoelastic forces may be further attributed to the tethering rate being that of a growing filopodial extension, potentially yielding active formation of actin cytoskeletal structure similar to that seen by Pontes *et al*. We attempted to confirm this with the transformation of the HeLa cells with the LifeAct plasmid, which enabled the actin to be visualized via fluorescence microscopy. The quantum efficiency of our camera, however, limited the fluorescence signal that could be detected. Thus, we could not visualize the actin in live cells.

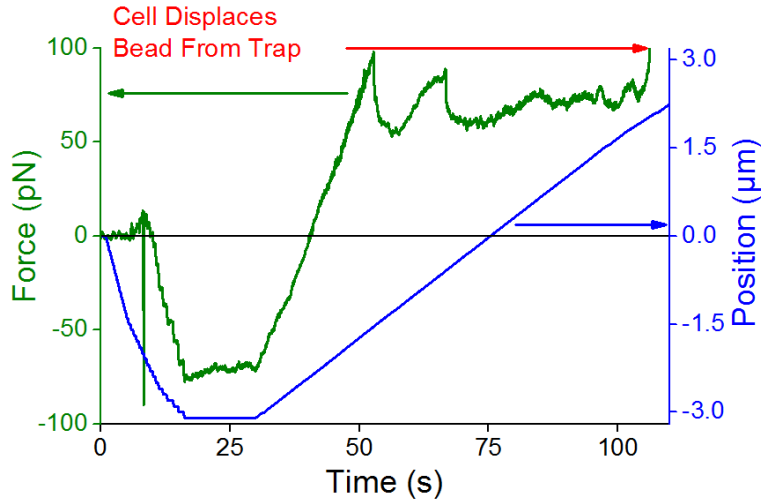


Figure 2.19 Membrane tethering experiment that illustrated multiple tugging events on a single bead that eventually led to displacement of the bead from the trap.

### 2.3.3.3. CELLULAR RESPONSES

---

The hypothetical formation of cytoskeletal structure within tethers was corroborated in bead release experiments performed after tether extraction. It was found the longer beads were held extended from the cellular surface, the less the bead moved back towards the surface upon release from the optical trap. Assuming tethers were primarily composed of cellular membrane with no underlying cytoskeletal structure, one would expect a nearly complete elastic response with the bead snapping directly back to the surface, as was seen by Raucher *et al.*<sup>195</sup> Furthermore, as tethers were maintained well above the dish surface in these experiments, adherence of membrane/tethers to the glass surface of the dish causing a similar, shortened response is highly unlikely.

The presence of cytoskeletal structure formation was further supported by cellular responses seen upon the tethered bead. These responses varied from tether breakage to bead tugging to full bead escape from the trap center (Fig. 2.19). A variety

of sources can be attributed to tether breakage including: bond breakage from the bead, tearing of the cellular membrane, and cellular cleavage of the membrane. This was one of the primary problems leading to non-representative tether force measurements that were ultimately discarded. Furthermore, the presence of multiple sources makes it difficult to identify the root cause, especially without further complex experimentation. However, it can be ascertained these results may be attributed to a cellular response, such as bond breakage via protein conformational changes or tether cleavage to maintain membrane integrity and pressure.

The tugging and total escape of beads from the trap further argued for a cellular response that theoretically is attributed to the formation of cytoskeletal structure. Specifically, the tugging is a clear cellular response that arises primarily from a singular source: myosin II activity on actin filaments. Whereas bead escape from the trap is related to the transient tethering force being larger than the force the trap could apply, which could be attributed to cytoskeletal structure, larger tethering radius creating larger initial forces, and/or molecular motors acting on the cytoskeletal structure in concert at the time of escape. The scope of identifying these root sources, however, extends beyond the scope of the research performed.

#### ***2.3.4. MEMBRANE BLEBBING FORCES***

---

Membrane blebbing induced through the silencing of ADF and COF was effectively measured with the optical tweezers setup as a function of the blebbing diameter (Fig. 2.20). Although we are by no means the first to measure forces on blebbing cells<sup>147</sup>, to our knowledge we are the first to passively measure blebbing

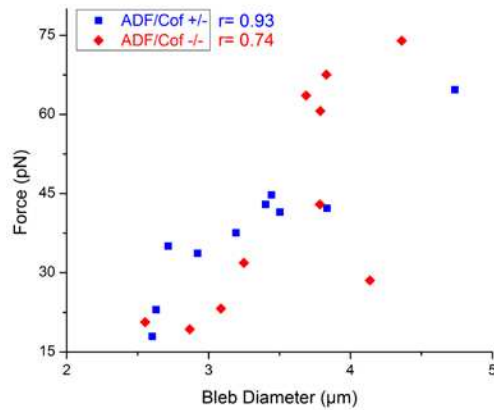


Figure 2.20 Bead displacement force as function of bleb diameter illustrates a high level of correlation. Correlation coefficients ( $r$ ) are shown to the right of the plot legend.

related forces through use of 3-dimensional bead displacement within an immobile trap as opposed to measuring the cortical tension as a function of tethering experiments. Furthermore, we have shown that the force of displacement grows with the size of the bleb, a result to be expected. This result, however, can be tied back to the cortical tension of the cell at the bleb site, which effectively dictates the initial hole size of the bleb.<sup>68</sup> Moreover, our displacement based force measurements provided size based estimations of forces pulling on nuclear membrane extensions tied to the plasma membrane that effect nuclear architecture and mechanotransduction of signal leading to genetic alterations in expression as a function of blebbing.<sup>191</sup> Estimations of these forces therefore becomes impactful in understanding how mechanotransduction plays a role in the development of diseases such as cancer. Furthermore, understanding the force applied during this transduction may be impactful in understanding specifically how much force it takes to turn specific genes on and off related to disease specific progression. This however extends beyond the scope of this work.

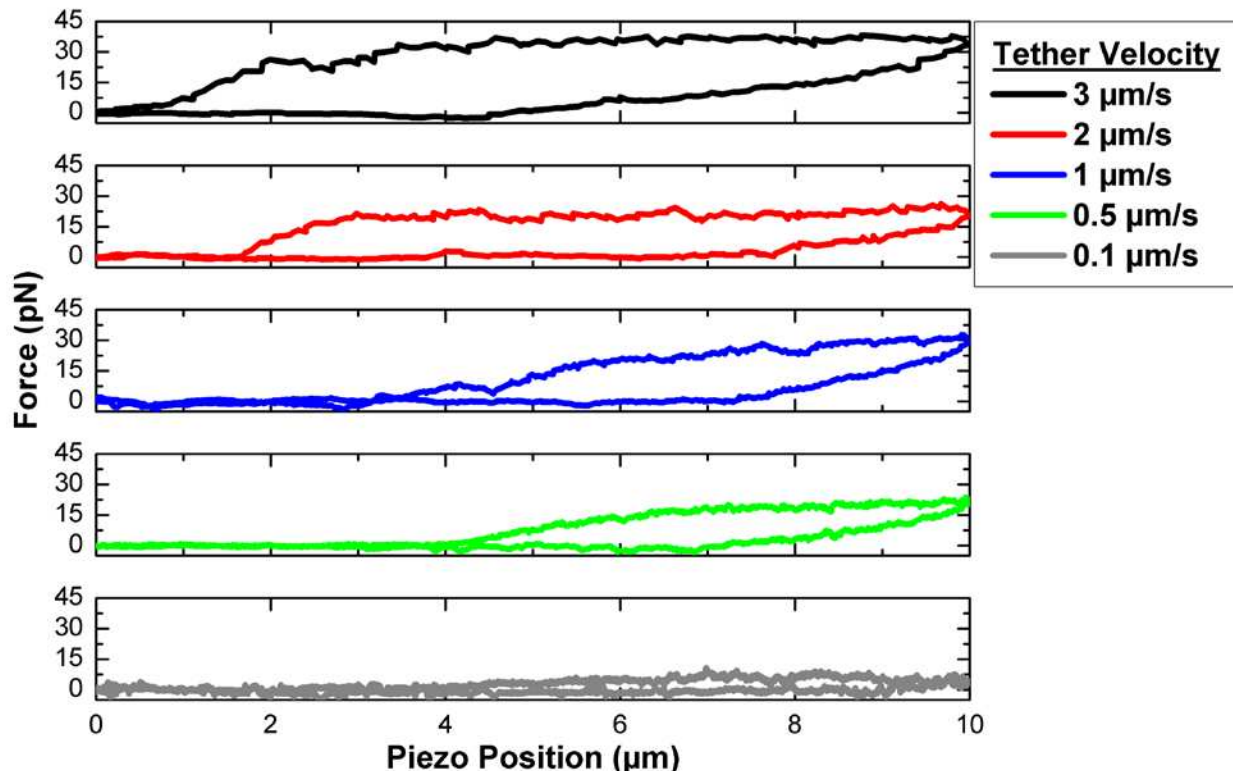


Figure 2.21 Membrane viscoelasticity experiment evolving top to bottom with different tethering velocities. Force based tracking curves illustrate hysteresis and a non-elastic response. Moreover, memory of tethering events is seen in successive tethers as an increased reservoir dampening the force-based bead displacement.

### 2.3.5. MEMBRANE VISCOELASTICITY RESPONSES TO VELOCITY CHANGES

Membrane viscoelasticity measurements proved to be difficult as a function of tether pulling speed due to the cellular responses described above. A characteristic response, however, can be seen in Fig. (2.21). As can be seen, tethering force increased with increasing velocity, an unexpected result based on the results obtained in our previous tethering experiments as well as those found in the literature. We expected larger tethering forces at lower velocities due to stronger cellular adhesion and more time for the cell to respond to an external stressor. This data, however, was collected in order of decreasing velocity of tether pulling. Thus, the first pull was at the highest velocity decreasing in steps down to the lowest velocity. When tethers were pulled in

the opposite direction, or increasing velocity, the highest tether force was also seen in the first pull, indicating the cell “remembers” where stress has been applied and relaxes this region upon successive stresses, regardless of velocity. This idea is also illustrated in the “memory” of the tether, as the initial region, or zero force region, of the tether was larger with each successive pull. This result indicated the tether is retaining increasing amounts of membrane reservoir. How velocity effects this pulling, however, is yet to be fully elucidated. Multiple measurements were made with both increasing and decreasing velocity profiles, yet most measurements were affected by some sort of cellular response. This response was more prone to occur at the lower pulling speeds that afforded the cell more time to respond to the stimulus.

#### **2.4. DISCUSSION & CONCLUSIONS**

---

A fully functional optical tweezers setup was built and validated through measurements of membrane tethering forces. The measurements further illustrated cellular related responses compounded by slower tethering speeds. Although it could not be determined in this work directly, it is our belief that these cellular responses are mediated through actin polymerization and myosin II activity similar to retraction of a membrane bleb. This is supported by the fact that Pontes *et al* illustrated the presence of actin in tethers of fixed cells that had been pulled at the same tethering speed. The presence or absence of actin in tethers was previously thought to have been settled in favor of the latter. Our work illustrates that the presence of actin may be subject to the tethering speed. We, however, cannot confirm or deny this allegation based on the current study.

The tethering dynamics also showed memory contained within the tether through two independent measurements. Direct tethering and maintenance of tether length for increased periods of time indicated decreased retraction upon bead release from the trap. Viscoelasticity measurements consisting of repeated tether pulling and retraction on the same bead illustrated increased membrane reservoir with each successive pull. This memory may also be related to actin polymerization as described above; however, it may also be related to a larger localized reservoir of membrane lipids in the tether. The latter hypothesis is less supported, as a localized reservoir of lipids would theoretically be absorbed back into the rest of the membrane based on its fluid nature. Moreover, a similar reservoir would be expected in membrane blebbing, which we know not to be the case. Overall, this further supports the idea actin polymerization occurs leading to memory and cellular response capabilities.

Membrane blebbing experiments illustrated a high degree of correlation between the measured force and the bleb radius. To our knowledge, these are the first known measurements of pressure-based displacement related to blebbing forces with an optical trap. RNA silencing measurements published with this work have also illustrated nuclear rearrangement correlating to bleb formation.<sup>191</sup> The abnormalities seen have been linked to a loss of cofilin and actin depolymerization factor mediated interaction with actin filaments. The filaments tied to the nucleus through linker of nucleoskeleton and cytoskeleton (LINC) proteins then allow conduction of myosin II forces to the nucleus leading to deformation of the nucleus like that seen in many disease processes. Furthermore, the increased myosin II activity leads to increased

internal cellular pressure creating disruptions of cytoskeletal interaction with the membrane. Disruption of these interactions leads to membrane blebbing. Thus, measurement of the bleb displacement forces reflects the amount of force related to nuclear rearrangements, rearrangements that have been tied to abnormal cellular signaling in disease processes such as cancer.

Overall, the work presented illustrates the influence of biomechanical measurements on the elucidation of membrane related properties. The properties of the membrane are characteristic of the cellular type.<sup>124,135,136,145,147</sup> Furthermore, tuning measurement properties directly influences the characteristic properties of the cell. In general, the more time the cell is given to respond, the more likely a response will occur. This provides further evidence to the growing testimony that cells in their natural environment can adapt to biomechanical cues and build in memory. These responses and memory have been shown to be related to the cytoskeletal structures<sup>196</sup>, which we believe also affected our measurements. This is further evidenced by the complex linking between the cytoskeleton and nucleus illustrated through RNA silencing used in the blebbing measurements.<sup>191</sup> This further illustrates the ability for direct mechanotransduction from the membrane to the nucleus directly effecting genetic expression. Our measurements place directly measured values related to the mechanotransduction. These values may hold promise for understanding the complex changes related to induction of disease type processes. Further work in this field continues and will continue to produce characteristic

biomechanical properties directly effecting cellular signaling related to normal and diseased cell architecture.

### 3. CHAPTER 3: FORCE SPECTROSCOPY IN THE BLOODSTREAM OF LIVE EMBRYONIC ZEBRAFISH<sup>2</sup>

---

---

#### 3.1. INTRODUCTION

---

---

Fluid pressure forces and shear stress in blood vessels play a critical role in embryonic cardiovascular development. Tissue architecture is dependent on a concerted effort between chemical signaling, mechano-transduction of flow forces, metabolic stimuli, and cell-cell or cell-matrix interactions<sup>99</sup>, which regulate gene expression via a signaling cascade. The pathways related to chemical signaling via growth factors are well established.<sup>101,197,198</sup> The factors related to mechano-transduction, however, are primarily evidenced by *in vitro* studies.<sup>93,104,108,199</sup> Furthermore, measuring these dynamic forces in living organisms is challenging. *In vivo* evidence, nonetheless, has been shown with imaging studies illustrating ciliary protrusions from the cellular surface for flow based sensing.<sup>111,112</sup> Though the evidence exists, measurement of the underlying forces is purely an estimation. The analysis of such forces is further complicated by crowding effects that turn blood into a non-Newtonian fluid.<sup>200</sup> Measurement accuracy also depends on preserving natural flow and morphology. Thus, the development of non-invasive tools to directly probe

---

<sup>2</sup> Statement of Work: Zebrafish were kindly provided by Dr. Deborah Garrity. Zebrafish breeding and preparation was performed by Bryce Schroder and Brennan Johnson. Optical tweezers experiments were executed by Bryce Schroder and Brennan Johnson. Data analysis was performed by Bryce Schroder with methods being developed by Bryce Schroder, Brennan Johnson, and Diego Krapf. Some of the work in the Introduction, Material & Methods, and Results sections are as published in Frontiers in Optics 2014 OSA Technical Digest (online) (Optical Society of America, 2014).<sup>217</sup> Link: <https://www.osapublishing.org/abstract.cfm?URI=FiO-2014-FTu1F.5>.

forces *in vivo* presents a key step in understanding normal cardiovascular development.

Key to the development of these tools is the selection of an appropriate *in vivo* model. Several model organisms exist for the study of vertebrate blood vessel development; however, zebrafish have emerged as one of the most widely studied. The rapid development, small size, optical transparency, and vertebrate lineage of the embryonic zebrafish make it an excellent model.<sup>98</sup> Furthermore, successive breeding yields many embryos whose heart development and initiation of circulation occurs around 24 hours post fertilization.<sup>201</sup> Thus, it is also a high throughput model yielding multiple experiments throughout the same period that alternative model organisms develop for a single experiment. Zebrafish have therefore been employed in a variety of studies aimed at cardiovascular development.<sup>98,112,202–210</sup>

Normal development is well characterized throughout cardiovascular formation within vertebrate lineages including zebrafish. Characterization, though, is primarily related to chemical and morphological changes related to development. The dynamically changing forces are inferred from the morphological changes that are occurring and *in vitro* models. Flow dynamics in the developing zebrafish system have been exemplified through techniques such as particle image velocimetry (PIV) in both normal and abnormally developing fish.<sup>73,204</sup> Dynamics have further distinguished the velocity profile that has been used to estimate the flow driven forces and wall shear stress.<sup>204,206</sup> However, estimation of forces with these methods is indirect and dependent on assumptions of viscosity and particle size, shape, and

rigidity. This further evidenced the gap in tool development aimed at full environmental characterization providing more accurate force-based measurements.

Optical tweezers are capable of probing forces associated with flow. The platform has been used in a variety of flow environments used for cell sorting<sup>146,211</sup>, characterizing flow dynamics<sup>212</sup>, and measuring flow induced cellular stretching.<sup>139,142,146,157,167,213</sup> Optical tweezers present an advantage for work in zebrafish, as they can be used non-invasively to directly measure forces on cells under flow without *a priori* knowledge of the environment. The accuracy of measurements, however, is dependent on the precision of calibration. Typically, calibration is performed by the methods described in the previous chapters. This type of calibration suffers the same limitations as force estimates based on flow dynamics; assumptions of viscosity and particle size are necessary to provide calibration values thereby limiting the accuracy and precision. A novel calibration technique developed by Yuval Garini's group based on the analytical solution to the Smoluchowski equation described in the first chapter has been employed to overcome these limitations.<sup>41</sup> It makes use of the probabilistic properties of Brownian motion within an elastic potential to eliminate the need for *a priori* knowledge of the environmental properties. Thus, the environment and trap characteristics can therefore be derived through particle tracking techniques.

Further complicating optical tweezers experiments is the propensity for laser heating leading to damage in tissues with excess power. The causes of laser heating are related to wavelength dependent absorption described in greater detail in the first

chapter. As discussed, this is overcome by targeting the laser wavelength for minimal absorption within the tissue. Although absorption is minimized, it is not eliminated. Several studies have shown the propensity for damage with increased laser power.<sup>125,129,214,215</sup> Nonetheless, studies have also shown the ability for optical trapping *in vivo* without damage.<sup>216</sup> Ultimately, laser power was minimized to reduce the potential for irreparable damage.

The work presented in this chapter therefore describes the adaptation of an optical tweezers setup to directly trap blood cells found within circulation of developing embryonic zebrafish. Although optical trapping proved straightforward, the extraction of force related data proved less trivial. Conventional techniques for calibration and particle tracking were unsuccessful due to characteristics of embryonic zebrafish blood being undefined and image complexity, respectively. Development of novel tools and analysis techniques are therefore described relative to the complications found with conventional methodologies. Our results illustrate the first known optical trapping of blood cells within a developing zebrafish, and were reported at *Frontiers in Optics* in 2015.<sup>217</sup> Furthermore, the forces extracted have provided the first non-invasive, direct force measurements associated with flow inside zebrafish blood vessels. Force and velocity information also enabled further characterization of the fluid environment yielding the first known value for apparent viscosity of embryonic zebrafish plasma.

## **3.2. MATERIALS & METHODS**

---

### ***3.2.1. ZEBRAFISH PREPARATION***

---

Adult wild-type zebrafish were raised and bred in accordance with Westerfield.<sup>218</sup> Fertilized eggs were harvested and incubated at 28°C in embryo water until initiation of circulation, which begins around 24 hours post-fertilization (hpf). At this stage, embryos were dechorionated and placed in a coverglass bottom dish in a solution of 0.17-0.2 mg/mL tricaine (Fig. 3.1A Inset). We found this concentration to be optimal for preventing embryo movement with minimal effect on cardiac function. The dish was then placed on the optical tweezers setup for imaging. Embryos were given at least five minutes for onset of anesthetic effect and temperatures to stabilize.

### ***3.2.2. OPTICAL TWEEZERS EXPERIMENTAL SETUP***

---

Force spectroscopy was performed on our home built optical tweezers setup with a 1070nm infrared trapping laser (YLR-5-1070-LP, IPG Photonics, Oxford, MA) and a high NA objective (60X water immersion, 1.20NA; Olympus) built around an IX-71 inverted microscope (Fig. 3.1A). The fish were positioned aligning the trap centrally to each vessel location (Fig. 3.1B). For our studies, 6 measurement locations were selected based upon high visual clarity, anatomical reproducibility, and representation of flow throughout changing vessel architectures (Fig. 3.2). Upon thermal equilibration and anesthetic onset, the trap was turned on. Power was maintained at a minimum preventing damage to the fish, and images were recorded

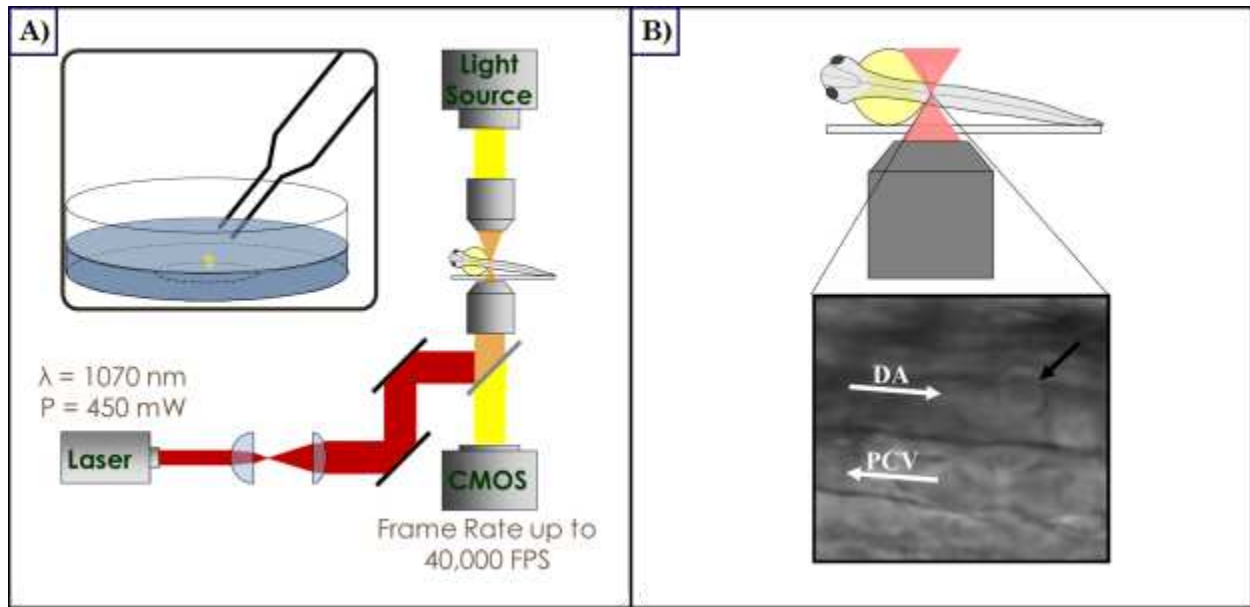


Figure 3.1: A) Illustration of optical trapping experiment with placement of zebrafish embryo inset. B) Illustration of a typical trapping experiment with a cell highlighted by the black arrow trapped within the dorsal aorta just above the posterior cardinal vein. White arrows indicate blood flow directions.

at 125 frames per second (fps) on a high-speed camera (Fastcam SA3, Photron, San Diego, CA). Images were recorded with the trap on and off to provide force and velocity information, respectively. Immediately after measurements, the heart was arrested via tricaine overdose, and a cell was trapped and held in the vessel for calibration purposes. Images were then recorded at 25,000 fps for ~15 seconds.

### 3.2.3. IMAGE ANALYSIS

To determine the forces related to displacement, we had to extract the displacement information along the axis parallel to flow. This proved to be a difficult task, as the cell position could not be extracted from algorithms typically used for tracking particle positions such as those described for bead tracking within the previous chapter. The difficulty in tracking cellular position is derived from the fact that cells are inhomogeneous, typically aspherical, and highly elastic in nature.

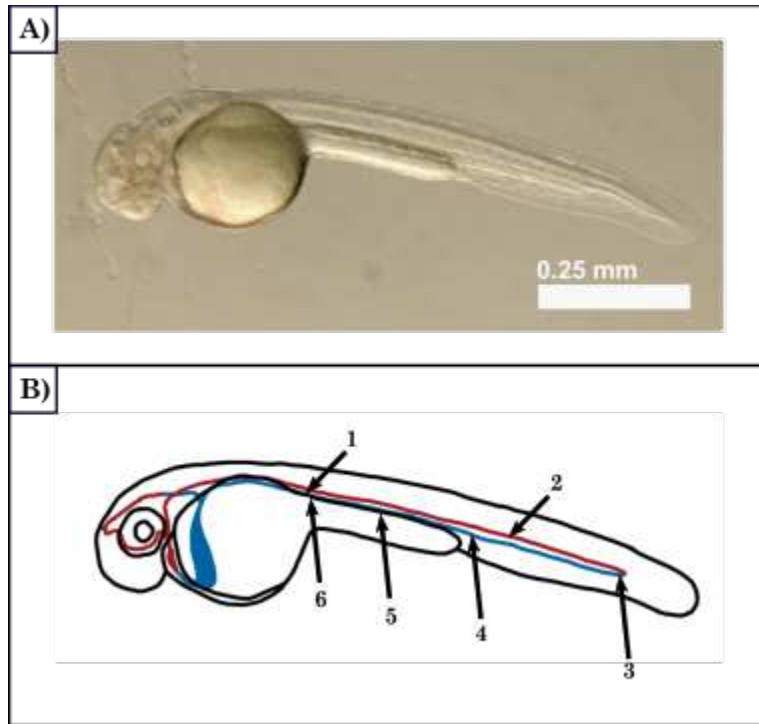


Figure 3.2: A) White light image of a zebrafish embryo taken from a stereomicroscope. B) Simplified illustration of zebrafish blood architecture.

Hence, they do not produce the nice airy disk pattern seen with spherical particles as described in the previous chapter. Moreover, the environment blood cells reside in is inhomogeneous and dynamic creating greater complexity for tracking by simple bright-field microscopy.

These problems are typically overcome with use of fluorescently labelled cells that can be traced by simple particle image velocimetry techniques within a flow field.<sup>219</sup> Our setup, however did not possess the capability to image fluorescent cells. Other groups have also used image processing technique to remove background intensity information leaving only intensity profiles in dynamically changing areas.<sup>220</sup> In general, this will remove structural data leaving the intensities where flow and moving boundaries (heart or vessel walls) occur. PIV is then applied to the filtered images to track the moving particles. Our work, however could not directly

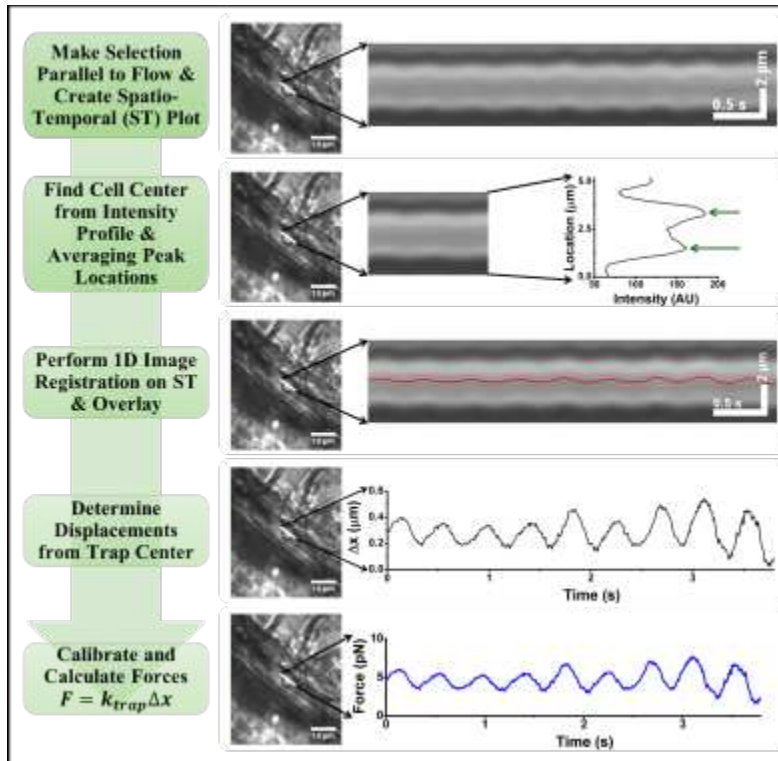


Figure 3.3: Flow diagram for creation of spatio-temporal (ST) plot for extraction of cellular displacement and associated force information throughout a trapping experiment.

employ either of these techniques. Furthermore, the accuracy of tweezer measurements necessitates subpixel tracking precision not achieved with PIV techniques.

Ultimately, this problem was overcome by extracting a line of pixels along the axis of flow from each image and combining each line into a spatiotemporal (ST) plot (Fig. 3.3), a.k.a. a kymograph. This plot, produced from a custom Labview code (Appendix A-2.10 & A-2.11), contained the displacement information and resulting waveform. The waveform was extracted by performing a 1-dimensional image registration process, where a single line of pixels representing a single time point was extracted from the ST plot and registered against all other pixel lines in the plot to find displacements. This process was performed in Matlab with a code modified from

Guizar-Sicairos et al.<sup>221</sup> (Appendix A-2.12) Upon obtaining the displacement data, the center of the cell was found by taking the line of pixels used in the image registration process and plotting its intensity profile. Two peaks in the profile correlating to the cell edge were found and fit to find their center positions. The peak positions were averaged to estimate the cell center, which was combined with the displacement data giving the displacement of the cell center to be used in relation to the center of the trap. This information was crucial; without it we could not have accurately calibrated our trap and estimated the forces associated with flow. An overview of this process is highlighted in Fig. 3.3.

#### ***3.2.4. OPTICAL TRAP CALIBRATION IN A LIVING ORGANISM***

---

Optical tweezers use has typically been limited in living organisms. This can be attributed to a variety of causes as discussed above. One of the central issues is difficulty of trap calibration using conventional methods described in the previous chapters. As calibration is key to obtaining accurate force measurements, this presented a major hurdle. We overcame this problem with the use of a novel formalism developed by Yuval Garini's group<sup>41</sup> combined with conventional power spectral analysis for validation. The implementation of these methodologies is discussed below.

##### ***3.2.4.1. POWER SPECTRAL CALIBRATION***

---

As stated above, calibration was performed in a stagnant environment produced by stopping the heart with an overdose of anesthetic. Images were collected at 25,000 fps and analyzed by the 1D kymograph registration. Initially, the trap

stiffness was estimated utilizing the power spectral analysis method, as described in the previous chapter. This method, however, required values for viscosity and particle size. Data on blood cell size was found to be 3-8  $\mu\text{m}$  in the literature. Measured viscosity values for zebrafish plasma could not be found, and most studies referencing viscosity values for calculations assumed human values were comparable. A range of viscosity values, 1-10 mPa s, was therefore estimated from values measured from other fish species.<sup>222-227</sup> Therefore, calibration values were an imprecise range.

#### 3.2.4.2. *SMOLUCHOWSKI CALIBRATION*

---

The primary drawback to the power spectral analysis is that values must be inferred from the *in vivo* environment thereby decreasing precision. This issue was resolved through implementation of a formalism recently developed by Yuval Garini's group based on the Smoluchowski equation describing Brownian motion of a particle within a trapping potential.<sup>41</sup> The analytical solution to this equation (1.37) provides the probability of a particle's position in a window of time given its initial position (Fig. 3.4A). The probability distribution has a characteristic width, or variance, that widens with time and will converge to the steady state Boltzmann distribution. The characteristic width for each window of time is dependent only on temperature, the particle's diffusion coefficient, and the strength of the trap. Regardless of initial position, the width remains the same. Thus, a single particle's displacements within a sliding time window can be used to yield distributions similar to that seen in Fig. 3.4A, each with a characteristic width. The characteristic widths can be plotted

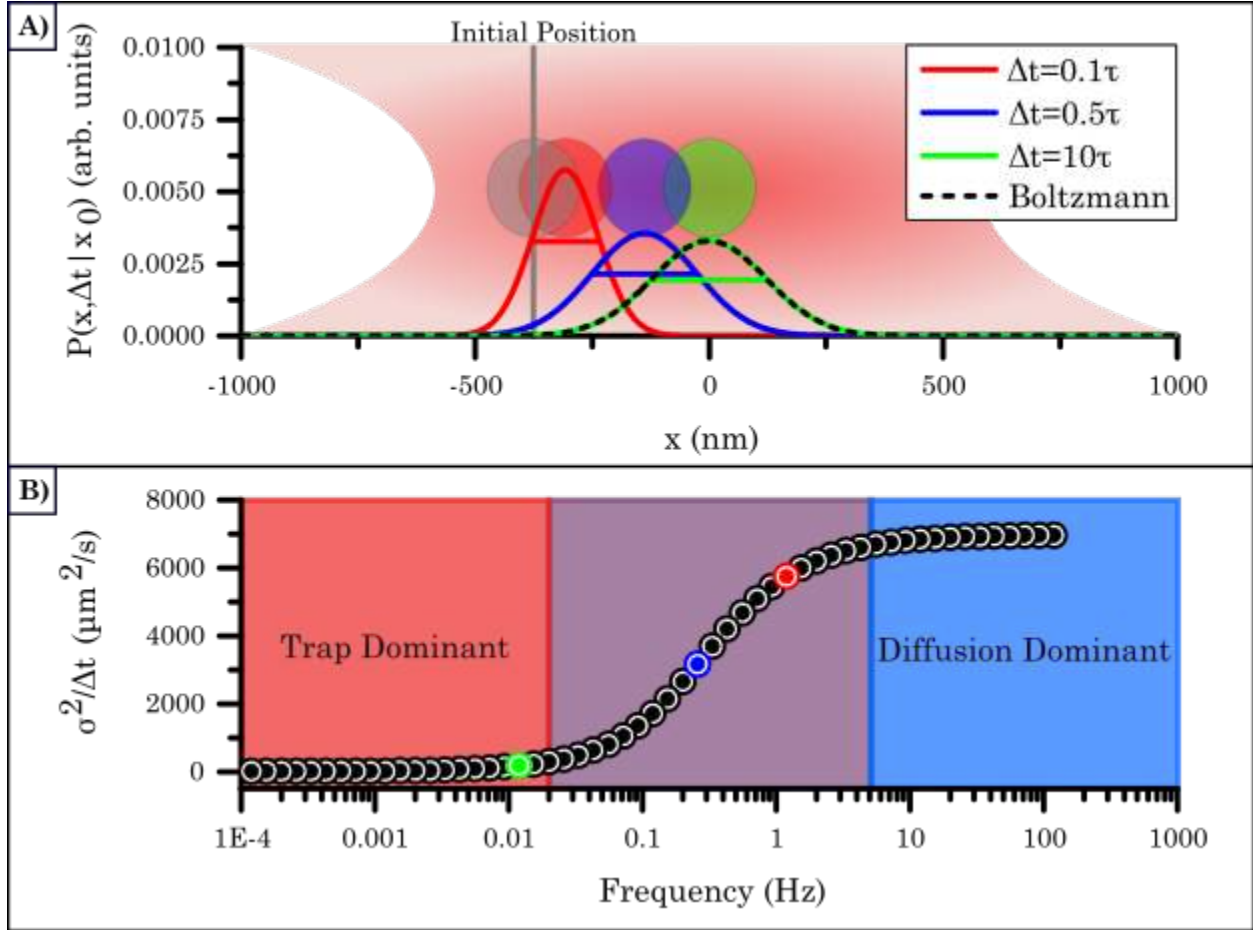


Figure 3.4: A) Figurative representation of the probability density functions over different time periods of a bead displaced from the center of a weak harmonic potential represented by an optical trap. The widths of the probability functions are characteristic of the time periods, regardless of the starting position that will provide a characteristic function like seen in B). The particular curves shown in A) are highlighted with their respective colors in B).

normalized to time to produce a characteristic curve that illustrates three regimes (Fig. 3.4B): a diffusion dominated regime that is manifested over short time periods, a trap dominated regime that is manifested over long time periods, and a region in between that is dependent on both forces. This characteristic curve is then fit using the variance achieved from 1.37 normalized to the sliding time window:

$$\frac{\sigma^2}{\Delta t} = \frac{k_B T}{k_{trap} \Delta t} \left[ 1 - \exp\left(\frac{-2k_{trap} D \Delta t}{k_B T}\right) \right] \quad (3.1)$$

where  $\sigma^2$  is the variance,  $\Delta t$  is the sliding time window,  $k_B$  is Boltzmann's constant,  $T$  is absolute temperature,  $k_{trap}$  is the trap stiffness, and  $D$  is the diffusion coefficient.

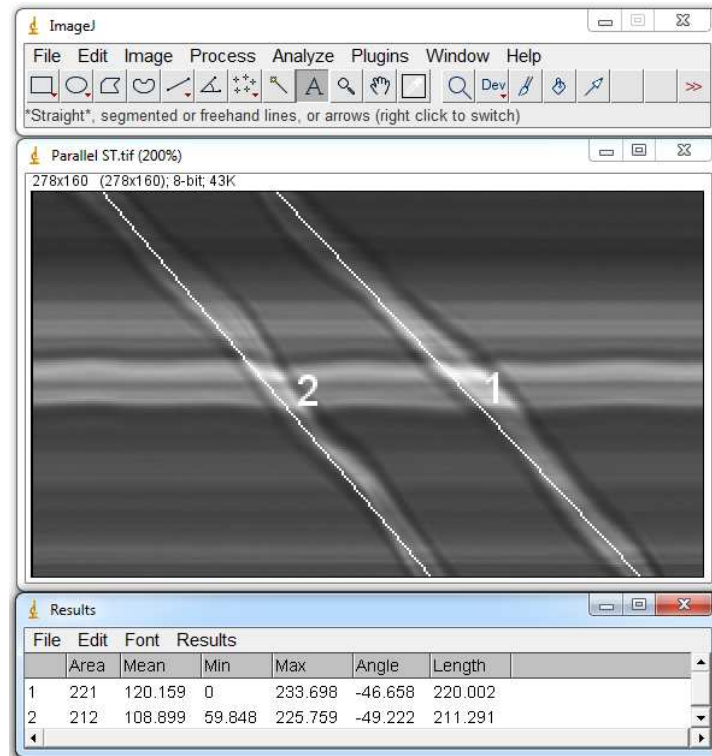


Figure 3.5: Extraction of cellular velocities occurred in ImageJ through the measurement of multiple angles. The angles were averaged prior to calculating the slope that correlated to the cellular velocities.

Thus, the benefit to applying this formalism to analyze our positional data is that we can extract information about a trapping potential without *a priori* information on the environment in which they reside. This is particularly powerful in the case of *in vivo* work where fluid and particle properties must be inferred from *ex vivo* work reducing accuracy and introducing assumptions upon conditions possibly differing within the particle's native environment.

### ***3.2.5. EXTRACTION OF CELLULAR VELOCITIES***

---

The creation of the ST plots described above proved to be a valuable tool in multiple ways. Not only could positional data be extracted for force measurements, velocity information of cells entering, leaving, and under non-trapping conditions

were represented by slopes of the patterns within the plots. These slopes were measured in ImageJ by overlaying lines on the edges of the pattern (Fig 3.5). The slope of the line was provided in pixels from ImageJ measuring tools. Using the pixels sizes with the x-axis representing time and the y-axis representing camera pixels, the frame rate (125 fps) and the camera pixel size (168.05 nm), respectively, were used to calculate the velocity:

$$u = 168.05 * 125 \text{ nm/s} \quad (3.2)$$

where  $u$  is cellular velocity and  $m$  is the measured slope.

### ***3.2.6. EFFECTIVE VISCOSITY DETERMINATION***

---

Effective viscosity was determined using the formula for the viscous drag force originally described by Stokes:

$$F = \zeta u \quad (3.3)$$

where  $F$  is the viscous drag force,  $u$  is velocity, and  $\zeta$  is viscous drag coefficient. The viscous drag coefficient is equivalent to  $6\pi\eta R$ , where  $R$  is our particle radius and  $\eta$  is the effective viscosity of the medium. This simple relation allowed us to plot the average forces found with optical trapping vs the measured cellular flow velocities. Moreover, multiple cells at varying locations in a single fish or a single location in multiple fish could be used in this manner to ultimately estimate the effective viscosity of the blood within zebrafish at the 24 hpf time point.

### 3.3. RESULTS

---

#### 3.3.1. GENERAL OBSERVATIONS

---

Flow onset was determined prior to experimentation by a 20X magnification stereo microscope. Upon removal to the optical tweezers setup and dosage with tricaine, flow was not always visible within the fish. Furthermore, flow would sometimes diminish with experimental time. Initially, these observations were attributed to varying tricaine effects and temperature cooling slowing the heart rate. Further observation found that the heart was still beating and therefore flow should have been present. We also noticed that certain fish would have a greater number of cells circulating with higher flow as opposed to lower flow fish with very few or no cells circulating and no differences in age of the embryos. A tracing of the vessel architecture back to the yolk sac found that there was an agglomeration of blood cells upstream from the heart that were not being circulated. The rate of flow and number of circulating cells was qualitatively correlated to the blockage of cells. Moreover, we would see clusters of cells undergo circulation supporting the theory that the blockages would break loose and undergo circulation periodically (Fig. 3.6). The cause of this observation is uncertain, although it is believed the lower flow velocities in the yolk sac lead to greater chances of the cells interacting and binding. As flow builds throughout development and the heart gets stronger, this no longer occurs due to faster circulation and an ultimate elimination of the pooled area within the yolk sac.

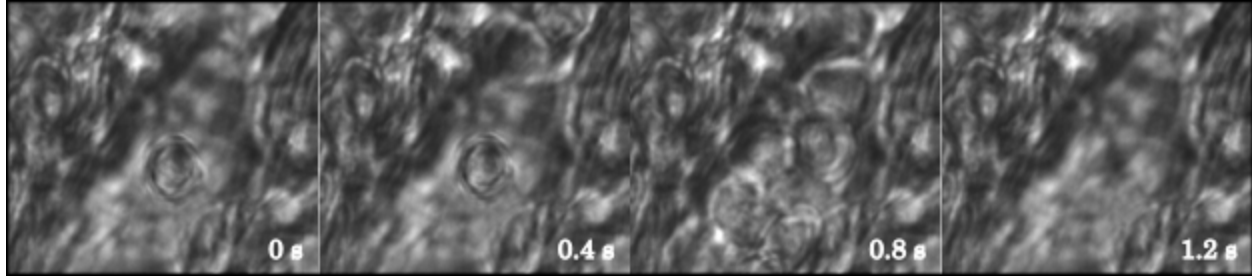


Figure 3.6: Time-lapse representation of clump of cells passing through the optical trap. Initially, a trapped cell is shown that is displaced in the 3<sup>rd</sup> frame by a clump of cells that has cleared by the 4<sup>th</sup> frame.

The effects of this variation at the onset of circulation on overall development is unknown. We, however, believe it to be minor, as the small size of the fish enables nutrient absorption without circulation.<sup>202</sup>

### 3.3.2. OPTICAL TRAP CALIBRATION

Optical trap calibration was achieved within a static trap eliminating the need for a dynamic viscous drag calibration that would have been extremely difficult inside a living organism. Two methods were employed to achieve the overall trap stiffness. The power spectral method achieved a cutoff frequency of  $4.08 \pm 0.03$  Hz (Fig. 3.7A). Image based measurements of blood cell diameter were found to be  $\sim 5 \mu\text{m}$  making our

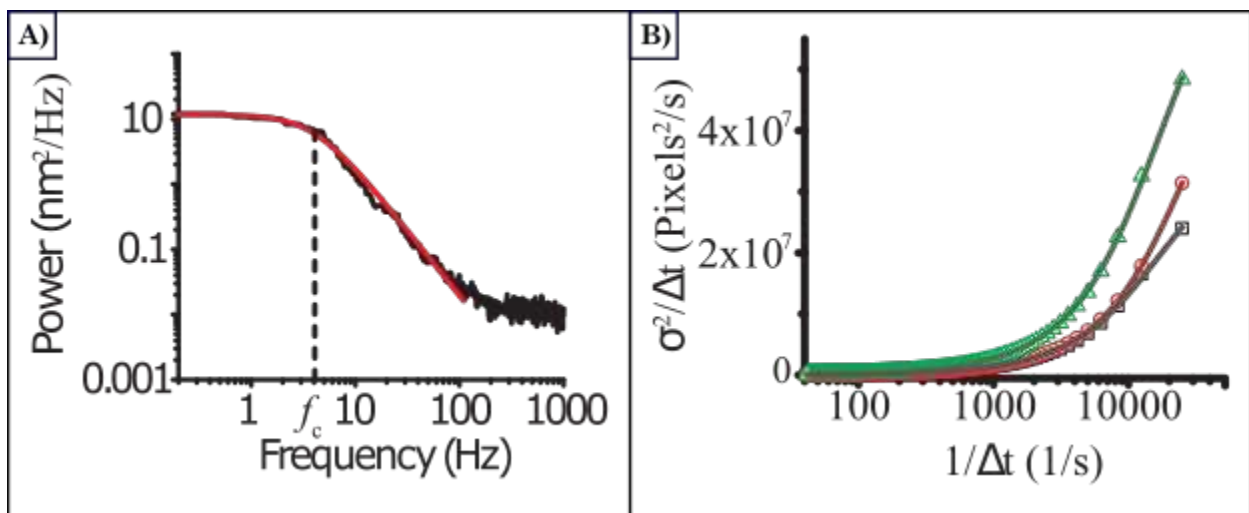


Figure 3.7: A) Power spectral measurement with a Lorentzian fit showing a cutoff frequency of  $4.08 \pm 0.03$  Hz. B) Smolochowski measurement with appropriate fits demonstrating an average trap stiffness of  $2.81 \pm 0.01$  pN/ $\mu\text{m}$ .

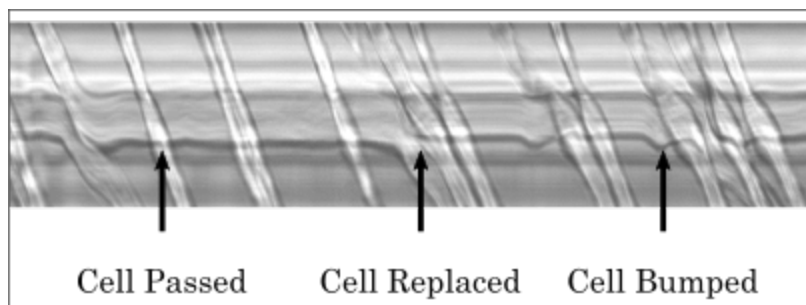


Figure 3.8: ST plot illustrating a trapped cell being passed by other cells, sometimes being bumped or replaced by the passing cell.

particle radius  $2.5\mu\text{m}$ . In conjunction with the range of viscosities described above, this produced a trap stiffness range of  $1.2\text{-}12.1\text{ pN}/\mu\text{m}$ . The Smoluchowski formalism improved upon this range providing a trap stiffness of  $2.81\pm 0.01\text{ pN}/\mu\text{m}$  directly from the fitting parameters (Fig. 3.7B).

### ***3.3.3. COLLECTIVE FORCE MEASUREMENTS***

---

Direct force measurements were achieved in multiple fish near the onset of flow. Given the reports in the literature on flow velocities in developing zebrafish<sup>112</sup>, we expected little variation in flow characteristics across fish. This was not seen at the onset of circulation due to the clustering described above. Thus, measurements were not made in a near constant velocity as we expected. Furthermore, vessel size and architecture varied slightly across fish, which also led to changes in flow dynamics. Although we targeted anatomically reproducible locations, the statistics at those locations were skewed by the flow dynamics and irreproducibility of exact conditions. Further compounding this problem was the number of circulating cells. Greater numbers of cells led to more difficulty getting measurements on single cells, as new cells would constantly enter the trap displacing the previous cell (Fig. 3.8). Thus, we could not extract a constant waveform under these conditions.

Trap limitations also occurred relative to the flow velocities and cell trapping capabilities, which was to be expected with minimized laser power to prevent damage adversely impacting the force we could apply. Furthermore, although embryonic blood cells are more rounded and contain a nucleus at the stage of development we were measuring, the cells were not perfectly spherical which also detracted from the force the trap could apply. The larger particle nature of the cells in theory enables greater force application relative to laser power<sup>127</sup>; however, this assumes that the trapping of a cell and bead of the same particle radius will produce equivalent forces. Optical trapping of cellular organelles of much smaller sizes has also been shown previously bringing into question whether it was whole cell or subcellular trapping occurring.<sup>228–230</sup> Blood cells typically lack organelles and are highly inhomogeneous, typically aspherical, and elastic in nature. Thus, the overall properties enabling cellular trapping are not equivalent to a polystyrene bead. Furthermore, assuming the ray optics regime applies, their refractive index is only slightly different from the media making their refractive properties low. In other words, the deflection of the beam comparative to a bead is much less. Less change in direction means less change in momentum resulting in a lower imparted force on the cell. Collectively, these all point to greater difficulty trapping a cell comparative to a bead of the same radius.

Regardless of the difficulties presented, optical trapping was achieved in several vessel locations at the onset of flow. Flow dynamics were primarily dictated by the pumping of the heart creating a pressure differential across the system. The pressure differential was pulsatile due to the beating of the heart. The pressure

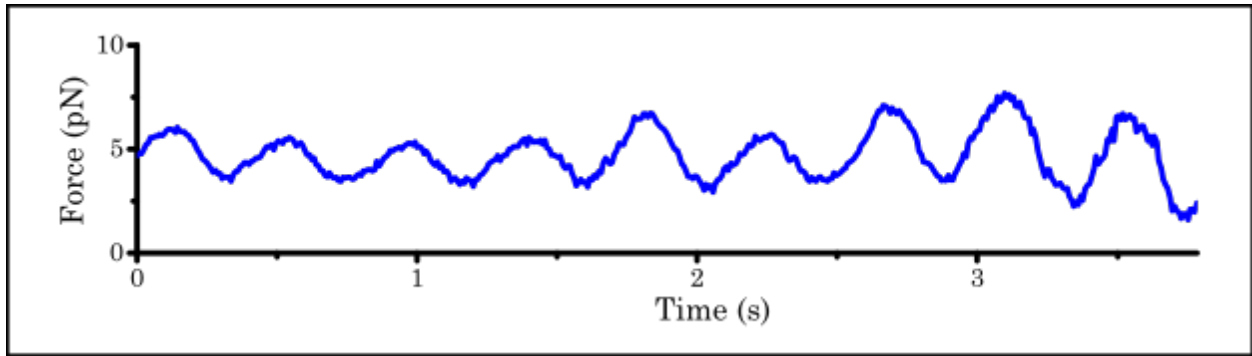


Figure 3.9: Force measurement of trapped blood cell in arterial flow illustrating the sinusoidal pattern representative of pulsatile flow driven by the beating zebrafish heart.

differential also seemed to be dictated by the blockage of cells previously described. Nonetheless, the pulsatile flow was reflected in the extracted waveform of the trapped cells (Fig. 3.9). The waveform illustrated the expected sinusoidal pattern characteristic of flow within an artery.<sup>231</sup> Furthermore, position in the vessel also dictated the flow velocities and the subsequent force felt (Fig. 3.10). Although we targeted the center of the vessel in most measurements, the potential for error did exist based on our qualitative selection of where the boundary walls existed. As there was no direct measurement of the vessel diameter and precise placement of the cells at a distance half that from the wall, we very easily could have been at different

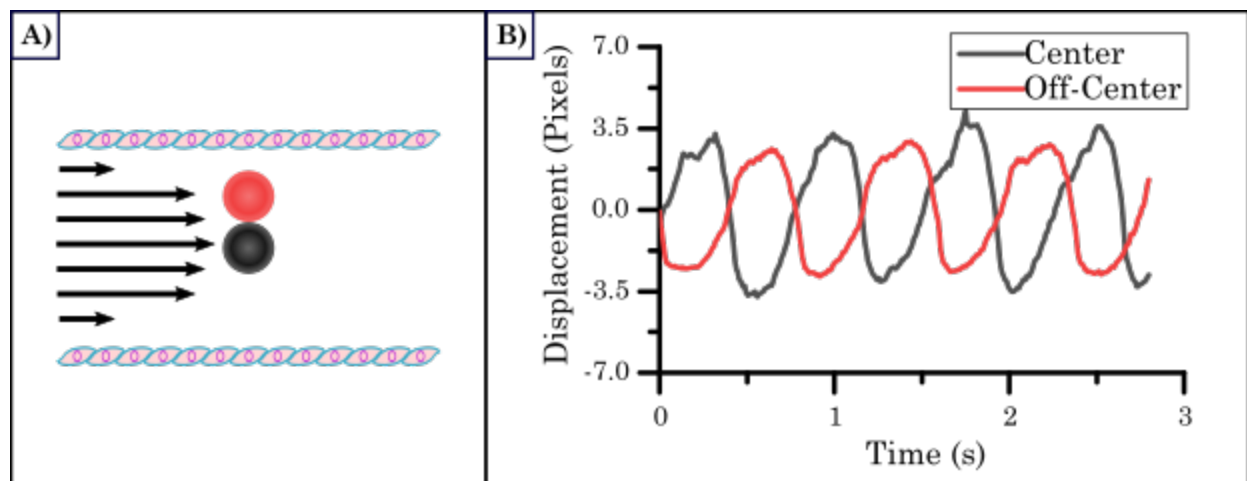


Figure 3.10: A) Theoretical velocity profile seen by a trapped cell at the locations shown. B) Actual displacement curves of single cell trapped within flow at the locations shown in A). As can be seen, the off-center cell experiences slightly lower velocities that can be seen in the slight narrowing of the peak to peak profile.

locations measuring the flow profile as opposed to the actual flow at the center. This was compounded by problems locating the boundaries axially as well, which was done by targeting the maximum width of the horizontal boundary. The cells would, however, typically tumble the closer they got to the boundary, helping localize vessel center. Overall, these effects lead to potential error in the force-based measurement.

To overcome the issues of force-based measurements in variable flow, a normalization can be achieved. This can be achieved through normalizing the force to the velocity achieving the viscous drag coefficient for each cell based on the measured velocity in the same flow. This provides a means to narrow the distribution and eliminate the problems associated with variable flow rates and the rudimentary positioning of the trap. The only other effects that can broaden the distribution is the cellular radius. Radius does vary, but much less than the flow velocities. Applying this approach, we achieved a viscous drag coefficient of  $0.4 \text{ pN}\cdot\text{s}/\mu\text{m}$  (Fig. 3.11B).

#### ***3.3.4. LOCATION BASED FORCE MEASUREMENTS***

---

Measurements were taken at multiple locations within the fish (Fig. 3.2B). This was done to characterize the flow along the vessel at different locations within the arteries and the veins, both close and distal from the heart. Measuring at these locations provided highly variable forces with differences in the pulsatile pattern measured. The variable forces most strongly correlated to the flow velocities, which was expected. Furthermore, the flow velocities qualitatively also depended on vessel diameter, another obvious assertion assuming Poiseuille flow:

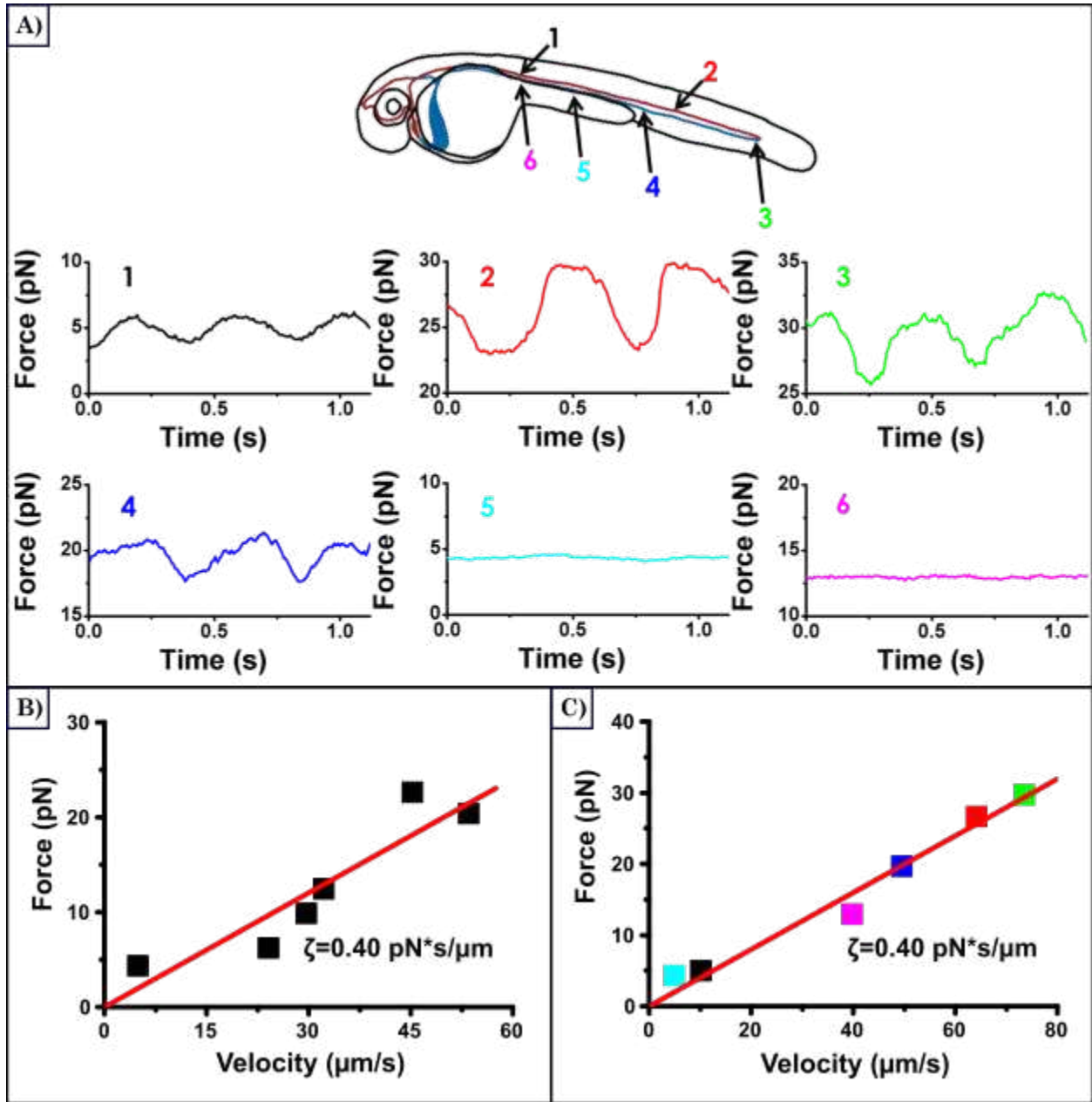


Figure 3.11: A) Measured forces at varying locations within a single fish starting in the dorsal aorta working their way down the tail to the tip of circulation and back up into the cardinal vein. The force graphs have been normalized to the same 10 pN force range to show the dampening of pulsatility seen moving from the arteries into the vein. B) Normalization of the force by the velocities seen at a single location across multiple fish provides the viscous drag coefficient with a high degree of linearity ( $R^2=0.98$ ). C) Normalization of the force against velocities at locations across a single fish provides the same viscous drag coefficient ( $R^2=0.99$ ).

$$Q = \frac{\Delta P \pi r^4}{8L\eta} \quad (3.4)$$

where  $Q$  is the average flow rate across the vessel length,  $\Delta P$  is the change in pressure along the vessel length,  $r$  is the vessel radius,  $L$  is the vessel length, and  $\eta$  is the

viscosity of the blood flowing through the vessel. The most impacting factor in this equation is the radius. Thus, changes in vessel architecture throughout the system, i.e. narrowing moving away from and dilation moving back towards the heart, should be reflected in the force profiles as well. This is reflected in the force reaching a maximum as we move away from the heart towards the tail decreasing from that point. Furthermore, vessel compliancy, or elasticity, changes from more rigid to more elastic moving from the arteries to the veins, respectively. Thus, a dampening of the pulsatile amplitude should also occur in the more elastic regions (Fig. 3.11A). Thus, the force profiles at different locations in the same fish fully illustrate the expected trends based on the changes in vessel architecture.

### ***3.3.5. EFFECTIVE VISCOSITY***

---

Effective viscosity was very simply determined after normalizing the force values to the flow velocities (Fig. 3.11B) at each location providing a viscous drag coefficient that is linearly dependent on both the viscosity of the medium and the particle radius. We measured the particle radius to be 2.5 $\mu\text{m}$ . Thus, using Stokes equation for the viscous drag coefficient:

$$\zeta = 6\pi\eta R \quad (3.5)$$

where  $\zeta$  is the coefficient,  $\eta$  is viscosity, and  $R$  is particle radius, we achieved an effective viscosity of 8.3 mPa·s. This is a very important measurement, as it provides the first known direct measurement of effective viscosity inside a living zebrafish. Furthermore, it provides a value to more accurately estimate forces from PIV profiles

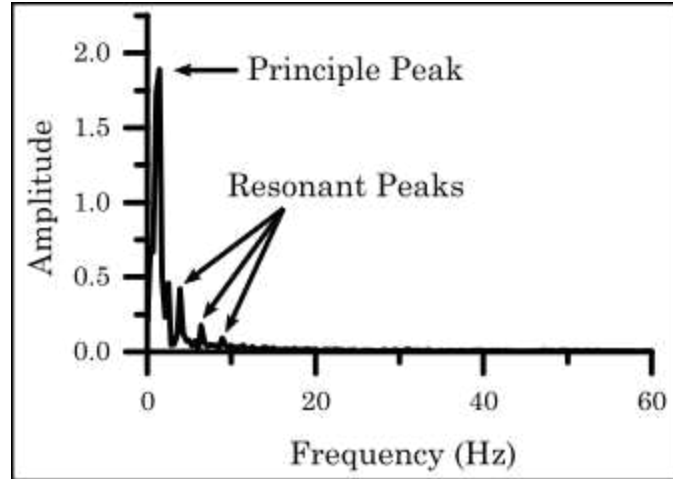


Figure 3.12: Power spectral measurement to find principal peak at a frequency correlated to the heart rate of the fish.

from a measured value as opposed to inferred. Thus, the system has been better characterized for this age of development.

### ***3.3.6. HEART RATE DETERMINATION VIA POWER SPECTRAL ANALYSIS***

---

Heart rate was measured by simply applying a fast Fourier transform to the displacement curves and finding the principle peak in the power spectral curve (Fig. 3.12). The heart rate is then found using the following equation:

$$HR = f_{principle} * 60 \quad (3.6)$$

where,  $HR$  is the heart rate and  $f_{principle}$  is the measured principle frequency from the power spectrum. Based on previous measurements, we expected a value of ~90 beats per minute (bpm).<sup>232</sup> The value we achieved was  $104.4 \pm 6.7$  bpm (n=8). This value is slightly higher than the expected values found in the literature. Multiple potential sources exist for this discrepancy: temperature induced laser heating increasing the heart rate, use of lower dosage tricaine comparative to literature values, fish age discrepancies, differences in fish breeding environments, and/or laser induced stress on the fish. Understanding this discrepancy is outside the scope of this work.

### 3.4. DISCUSSION & CONCLUSIONS

---

This work shows the first known direct measurements of flow driven force by an optical trap on circulating blood cells within developing embryonic zebrafish. Measurements such as these are critical to the understanding of normal cardiovascular development, as well as the forces associated with disease progression or repair of damaged tissue. Achievement of appropriate vessel architecture is dependent on the flow driven forces in conjunction with other mechanical and chemical cues. Understanding these forces and the flow and physical characteristics associated with the blood vessel environment can translate to higher degrees of accuracy in inferred measurements such as those made using PIV. Furthermore, PIV can be used in stronger flow fields where optical tweezers fail. Optical tweezers, however, can provide supplemental information on viscosity and shear stresses at the vessel wall where flow forces are lower. In conjunction, the two can work to provide larger amounts of information not attained in this work.

Although optical tweezers have a limit of capability in measurement of flow driven forces, trapping in younger fish with slower flows was quite simple. Fish of this age are also of benefit due to lower numbers of circulating cells that still illustrate a spherical shape with a nucleus, as opposed to the well-known unnucleated biconcave disc shape seen in adult red blood cells. Trapping of such cells yielded measurements of forces within different vessel architectures across different fish. Vessel architecture played a role in both flow rate and dampening of the pulsatile signal. More compliant vessels resulted in nearly a complete dampening of the

sinusoidal signal seen in more rigid vessels. Furthermore, larger diameter vessels illustrated lower flow rates, as expected in Poiseuille flow, which correlated to lower measured forces. The forces ranged much more greatly than expected, but a normalization of force to the measured flow velocities illustrated a highly linear trend that yielded the viscous drag coefficient of the fluid. Utilizing the measured blood cell radius further provided the first known measurement of apparent viscosity in an embryonic zebrafish. This measurement is critical to other measurements that necessitate *a priori* knowledge of the microfluidic environment that have typically used values for human blood viscosity for estimation of flow driven forces.

This work is fundamental towards future work in the area and lays a path for multiple other forms of measurements and extension into other organisms potentially, like has already been achieved in the ears of mice.<sup>216</sup> Further work in zebrafish can be made in conjunction with PIV techniques to yield further unique information throughout development. Work within different ages can be carried out, further yielding information on development of the cardiovascular system. Moreover, the use of mutant fish with slower flows, lower blood cell counts, and other hemodynamic changes can lead to greater understanding of forces and fluidic characteristics related to the mechanical signaling involved in disease progression.

## 4. CHAPTER 4: SUPERDIFFUSIVE MOTION OF MEMBRANE-TARGETING C2 DOMAINS<sup>3</sup>

---

---

### 4.1. INTRODUCTION

---

---

A myriad of signaling proteins are recruited to specific cell membranes via phospholipid-binding domains.<sup>233,234</sup> These molecules dock to the surface of specific lipid membranes and undergo two-dimensional diffusion in search of a target. Once the target is located, many proteins either activate or suppress a downstream signaling pathway for various physiological and pathological processes. Examples of membrane-targeting domains include pleckstrin homology (PH)<sup>235</sup> and C2<sup>236</sup>, which have been identified in hundreds of human signaling molecules as well as in eukaryotic species as diverse as fungi and flies.<sup>237</sup> PH domains bind specifically to phosphoinositides while C2 domains bind a variety of membranes, and a subset of C2 domains only bind membranes in the presence of calcium and play key roles in signaling pathways. The association to lipid membranes often takes place in response to different extracellular and intracellular stimuli, but typically the residence on the membrane surface is only temporary. The transient nature of peripheral protein-membrane interactions enables a tight temporal regulation of signal transduction.

---

<sup>3</sup> Statement of Work: Molecular biology and lipid preparation were performed in Dr. Olve Peersen's laboratory by Grace Campagnola. Chamber preparations and data collection were performed by Bryce Schroder, Grace Campagnola, and Kanti Nepal. Data analysis was performed by Kanti Nepal and Diego Krapf with codes provided by Diego Krapf and modified by Bryce Schroder. The work in this section is as published in Nature - Scientific reports<sup>287</sup>. Link: <http://www.nature.com/articles/srep17721>.

Further, membrane dissociation has also broad implications on the search for the target substrate, but this process is less understood. Recently, Knight and Falke observed the dissociation of PH domains from supported bilayers followed by rapid rebinding to the surface after a short excursion in the bulk solution.<sup>238</sup> They proposed that the hopping process may be important in the search for target molecules in eukaryotic cells. Subsequently, Yasui et al. found that PTEN (phosphatase and tensin homologue) molecules hop along the plasma membrane of living cells due to dissociation followed by rebinding.<sup>239</sup> PTEN is an important protein that suppresses development of cancer. It prevents cells from growing and dividing too rapidly by dephosphorylating phosphoinositide substrates on the plasma membrane. PTEN-membrane affinity is regulated by a C2 domain and it is enhanced by electrostatic interactions. The observed hopping of the C2 domain on the plasma membrane is thus expected to alter the dynamics of the search for a phospholipid substrate. A straightforward consequence of membrane hopping is that a molecule remains in its immediate vicinity for a short time and then jumps to a location that is further away than expected from two-dimensional diffusion. Therefore, the search process is allowed to explore larger areas and the molecule can bypass diffusion barriers that may be present in the membrane. However, hopping comes at the cost of the search being less exhaustive. We may ask the questions how the dynamics of membrane-targeting domains is affected by such long jumps and how this motion deviates from a simpler two-dimensional diffusion. Such potential complex behavior can yield anomalous diffusion of membrane-targeting domains, which would alter the outcome

of search processes and the sequential molecular reactions. Anomalous diffusion is widespread in the motion of molecules in biological systems.<sup>240–243</sup> In general, a particle exhibits anomalous diffusion when the mean square displacement (MSD) scales as a power law with an exponent  $\alpha \neq 1$

$$\langle x^2(t) \rangle = K_\alpha t^\alpha \quad (4.1)$$

where  $K_\alpha$  is the generalized diffusion coefficient with units  $\text{cm}^2/\text{s}^\alpha$ . When  $\alpha < 1$  the process is subdiffusive and when  $\alpha > 1$  it is superdiffusive. Subdiffusion in the cytoplasm<sup>244–246</sup>, the nucleus<sup>247</sup>, and the plasma membrane<sup>248–250</sup> of live cells is caused by crowding<sup>251,252</sup> and complex interactions with the cytoskeleton and macromolecular complexes, among others. Similarly, subdiffusion can take place in model membranes due to crowding and packing effects.<sup>253,254</sup> The appearance of superdiffusion processes in biomolecular systems is far less common. The archetypal mode of superdiffusive motion is due to active cytoplasmic flows and transport mediated by molecular motors, requiring ATP energy consumption.<sup>255–257</sup> From a theoretical point, there are three major mechanisms that can introduce superdiffusion.<sup>258</sup> It can be caused by correlations in the random walk, such as those in fractional Brownian motion with a Hurst index  $H > 1/2$ , by persistent directional motions (Lévy walks), and by long jumps (Lévy flights). Active biological transport can be modelled as Lévy walks.<sup>257</sup> Bulk-mediated diffusion processes, which can be described as Lévy flights, have been observed for transient adsorption on a solid surface where molecules display intermittent behavior, alternating between periods of immobilization at the solid-liquid interface and periods of diffusion in the bulk

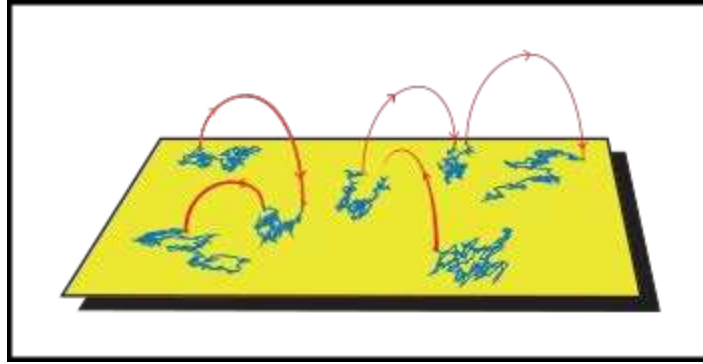


*Figure 4.1: Sketch of the diffusion process. A molecule alternates between phases of two-dimensional and three-dimensional diffusion. Diffusion in the three-dimensional bulk is much faster than diffusion on the lipid bilayer, and thus only the effective two-dimensional process is observed without loss of trajectory connectivity. The excursions into the bulk are seen as long jumps in the two-dimensional trajectories. This figure was provided by Kassi Prochaska.*

fluid.<sup>259,260</sup> In this article we report the experimental observation of superdiffusive transport of membrane-targeting C2 domains on supported lipid bilayers. Measurements of the diffusion of membrane-targeting domains are performed by single-particle tracking and are compared to both analytical theory and numerical simulations. In stark contrast to active cytoplasmic transport, superdiffusion in model membranes does not require energy. Our data strongly suggests that superdiffusion is caused by bulk-mediated diffusion, namely molecules dissociate from the membrane and perform three-dimensional random walks until they reach the membrane again and reabsorb at a new location, as sketched in Figure 4.1. Interestingly, the motion of membrane-targeting domains shows weak ergodicity breaking, a phenomenon that has recently attracted considerable attention in cellular environments and other complex systems.<sup>240,242,261–263</sup> The ergodic hypothesis, which is fundamental to statistical mechanics, states that ensemble averages and long-time averages of individual trajectories are equivalent. The violation of ergodicity has pronounced implications for the dynamics of individual molecules, which can be very

different from the ensemble statistics.<sup>240</sup> In the traditional way of obtaining the MSD, the square displacements are averaged over a large ensemble of molecules at a time  $t$  since the beginning of the measurement, i.e. an ensemble average. Alternatively, it is possible to perform the average over all the displacements in a lag time  $\Delta$  of a single trajectory, i.e. a temporal average. For ergodic systems, both averages converge to the same value. However, weak ergodicity breaking can take place as a consequence of kinetics with power-law statistics in the plasma membrane<sup>264,265</sup> and in the cytoplasm of live cells<sup>246,266</sup> as well as in inorganic complex systems such as quantum dots<sup>267,268</sup> and models of glassy dynamics.<sup>261</sup>

## **4.2. METHODS**

---

### ***4.2.1. IMAGING BUFFER***

---

Imaging and rinsing during the preparation steps was performed in an imaging buffer consisting of 50 mM HEPES, 75 mM NaCl, 1 mM MgCl<sub>2</sub>, 2 mM tris(2-carboxyethyl)phosphine (TCEP), 200  $\mu$ M CaCl<sub>2</sub>. CaCl<sub>2</sub> is necessary for C2 domain binding to the reconstituted membrane.

### ***4.2.2. PREPARATION OF PHOSPHOLIPID VESICLES***

---

Phospholipids were purchased from Avanti Polar Lipids (Alabaster, AL). Chloroform-suspended 18:1 ( $\Delta$ 9-Cis) PC (DOPC) and 18:1 PS (DOPS) were mixed at a ratio of 3:1. The phospholipid mixture was vacuum dried overnight and resuspended in imaging buffer to a final concentration of 3 mM followed by probe sonication to form sonicated unilamellar vesicles (SUVs).

#### ***4.2.3. PREPARATION OF COVERSLEIPS AND SUPPORTED LIPID BILAYERS***

---

Glass coverslips were cleaned by sonication in a detergent solution followed by soaking in 1M KOH. The coverslips were rinsed extensively in Milli-Q water and blown dry with a stream of nitrogen gas. Then, the coverslips were treated with an oxygen plasma. Immediately after the plasma cleaning, a perfusion chamber (CoverWell, Grace Bio-Labs) was adhered to the coverslip. In order to deposit the lipid bilayers a solution of SUVs (1.5-mM lipid) composed of phosphatidylcholine (PC) and phosphatidylserine (PS) at a 3:1 ratio in 1M NaCl and imaging buffer was introduced into the perfusion chamber and incubated for one hour at 4°C. Refrigeration minimizes lipid oxidation. The surface was then rinsed with imaging buffer multiple times prior to addition of protein sample.

#### ***4.2.4. C2A AND GST-C2A EXPRESSION AND PURIFICATION***

---

An expression plasmid containing the gene for a GST-ybbR-Synaptotagmin 7 (Syt7) C2A domain fusion protein was transformed into *E. coli* BL21-CodonPlus(DE3) competent cells. The ybbR segment provides a site for Sfp-catalysed fluorophore labelling.<sup>269</sup> Cells were grown at 37°C to an OD<sub>600</sub> of 0.6 and then induced to express protein with 0.5 mM IPTG at room temperature for 6 hours. The harvested cells were lysed at 18,000 lb/in<sup>2</sup> in a microfluidizer in a buffer containing 50 mM Tris pH 7.5, 400 mM NaCl and centrifuged at 17,000 rpm in a Sorval SS-34 rotor. The clarified lysate was loaded onto a 5-ml GSTrap FF column (GE Healthcare LifeSciences, Pittsburgh, PA) followed by gradient elution with 50 mM Tris, pH 8.0, 100 mM NaCl, and 10 mM glutathione. Fractions containing protein were pooled and diluted to

reduce the salt to less than 0.1 M prior to loading onto a HiTrap Q HP column (GE Healthcare LifeSciences, Pittsburgh, PA) and eluting with a linear gradient to 1 M NaCl in 25 mM Tris, pH 8.5, 20%(vol/vol) glycerol, and 0.02%(wt/vol) NaN<sub>3</sub>. A portion of the construct was subjected to thrombin cleavage and then separated using a Superdex 200 gel filtration column (GE Healthcare LifeSciences, Pittsburgh, PA) equilibrated in 50 mM Tris, pH 7.5 and 100mM NaCl to yield a ybbr-Syt7 C2A construct.

#### ***4.2.5. PROTEIN LABELLING***

---

10 mM CoASH (New England Biolabs, Ipswich, MA) in 400 mM Tris, pH 7.5 was mixed with 10 mM ATTO-565 maleimide (ATTO-TEC, Siegen, Germany) in dimethylformamide and incubated at 30°C overnight to form ATTO-565 CoA, then quenched with 5 mM DTT, 10 mM Tris pH 7.5. 10 µM GST-ybbr-Syt7 C2A and ybbr-Syt7 C2A were labelled with the ATTO-565 via SFP synthase (4'-phosphopantetheinyl transferase). Each reaction contained 50 mM tris 7.5, 10 mM MgCl<sub>2</sub>, 40 mM NaCl, 20 µM ATTO-565 CoA and 1 µM SFP synthase. Reactions were incubated at room temperature for 30 minutes, then placed at 4°C overnight. Samples were dialyzed against 1 L of 50 mM HEPES, pH 7.0, 75 mM NaCl, 4 mM MgCl<sub>2</sub> and 5% glycerol overnight at 4°C then concentrated to 10 µM.

#### ***4.2.6. IMAGING***

---

All images were acquired using an objective-type total internal reflection fluorescence microscope (TIRFM). The microscope was home-built around an Olympus IX71 body<sup>248,264</sup> with a 561 nm laser line as excitation source. A back-

illuminated electron-multiplied charge coupled device (EMCCD) camera (Andor iXon DU-888) liquid-cooled to  $-85^{\circ}\text{C}$ , with an electronic gain of 300 was used. In order to maintain constant focus during the whole imaging time we employed an autofocus system (CRISP, Applied Scientific Instrumentation, Eugene, OR) in combination with a piezoelectric stage (Z-100, Mad City Labs, Madison, WI). Videos were acquired at a frame rate of 20 frames/s.

#### ***4.2.7. IMAGE PROCESSING AND SINGLE-PARTICLE TRACKING***

---

Images were acquired using Andor IQ 2.3 software and saved as 16-bit tiff files. Then the images were filtered using a Gaussian kernel with a standard deviation of 1.0 pixel in ImageJ. Single-particle tracking of Atto-C2 and Atto-GST-C2 was performed in MATLAB using the U-track algorithm developed by Jaqaman et al.<sup>270</sup> under thorough manual inspection of detection and tracking.

### **4.3. RESULTS**

---

#### ***4.3.1. DIFFUSION OF MEMBRANE TARGETING PROTEINS ON SUPPORTED LIPID BILAYERS***

---

We tracked the motion of the membrane-targeting C2A domain from synaptotagmin 7<sup>271</sup>, labelled with Atto-565, in a supported lipid bilayer composed of phosphatidylcholine (PC) and phosphatidylserine (PS) at a 3:1 ratio. The lipid bilayer was self-assembled on a clean coverslip<sup>238</sup>. Imaging was done in a home-built total internal reflection (TIRF) microscope under continuous illumination at 20 frames/s. Surface densities were kept low enough to enable accurate tracing of trajectories and to allow assignment of connections even after micrometer-long jumps. Figure 4.2A

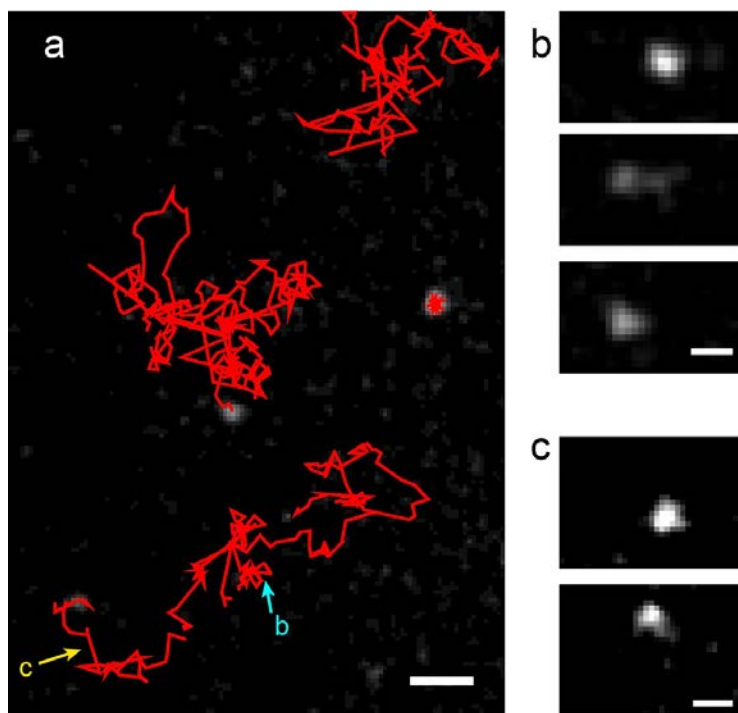


Figure 4.2: Single particle tracking of membrane-targeting domains. (a) C2A-Atto565 individual trajectories collected during a 10-s time window. Three mobile trajectories are observed in the image together with one immobile particle that is tracked but is not included in the analysis. The last frame is overlaid on the trajectories. Scale bar  $2 \mu\text{m}$ . (b) Region of interest (ROI) around the location of a micrometer jump that occur in the lowermost trajectory, marked with the letter b. Three frames are shown corresponding to before, during, and after the jump. Scale bar  $0.5 \mu\text{m}$ . (c) ROI around the location of the jump marked with the letter c. Scale bar  $1 \mu\text{m}$ .

shows an example of trajectories obtained in a 10-s window, overlaid on the last frame. Often, long jumps are observed in the particle trajectories as seen in the examples in Figs. 4.2B and C. These jumps suggest the C2A molecules detach from the surface and reabsorb after brief excursions into the liquid bulk. The motion in the bulk is much faster than diffusion on the viscous membrane and jumps are thus expected to occur instantaneously for all practical purposes. For the C2A domain, the diffusion coefficient in the lipid bilayer  $D_s$  is of the order of  $2 \mu\text{m}^2/\text{s}$ , but in liquid the

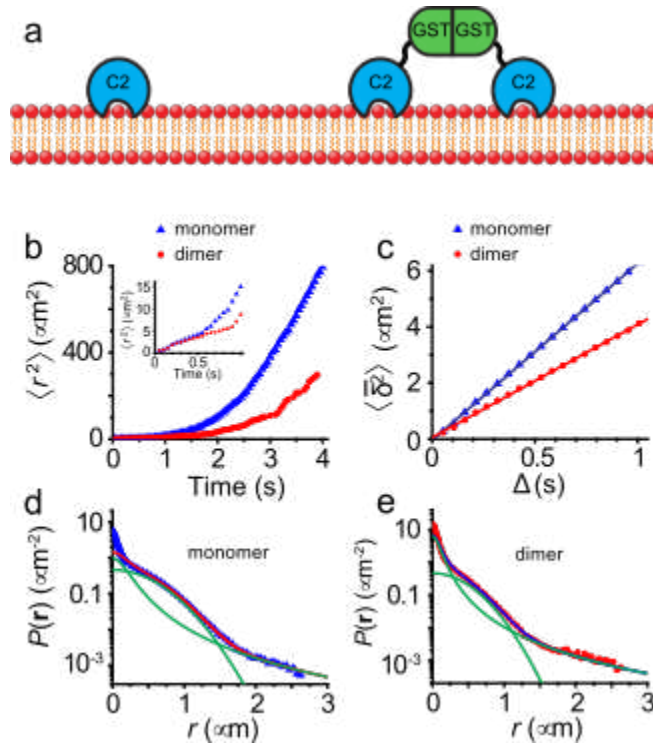


Figure 4.3: Anomalous diffusion analysis of membrane-targeting domain C2A (monomer) and dimer forming GST-C2A. (a) Sketch of the C2A monomer and the GST-C2A dimer employed in this study. (b) Ensemble averaged MSD  $\langle r^2 \rangle(t)$ . (c) Time averaged MSD  $\overline{\langle \delta^2 \rangle}$  as a function of lag time  $\Delta$ . The time average-MSD of individual trajectories varies greatly, so the MSDs of individual trajectories are also ensemble averaged. (d-e) Distribution of displacements for  $\Delta = 100$  ms. The total number of displacements are 207,000 and 56,000 for C2A and GST-C2A, respectively. The solid lines show fitting to equation (4) and to the individual components of the propagator, i.e. the Gaussian part  $[(1 - \omega)/2\pi\sigma^2]\exp(-r^2/2\sigma^2)$  and the Cauchy propagator part  $\omega\gamma/2\pi(r^2 + \gamma^2)^{3/2}$ . The cutoff at  $2.6 \mu\text{m}$  appears because trajectories are not connected when jumps longer than this distance take place. This threshold is placed in order to avoid the risk of particle misconnections.

diffusion coefficient  $D_b$  is estimated to be 100 times higher.<sup>272</sup> As a consequence, when a molecule performs a jump through the bulk it can sometimes be observed at reduced intensity in both the old and new locations within the same imaging frame, as seen in Figure 4.2b. In order to study the effect of the dissociation constant, we also employed a C2A construct fused to a non-membrane interacting glutathione S-transferase (GST), which has a strong tendency to dimerize (Figure 4.3a). The GST-C2A dimer forms two independent interactions with the membrane and will

consequently have a slower dissociation rate than C2A monomer, providing a good comparison for validating our superdiffusion predictions. Additionally, GST-C2A dimer has a higher viscous drag coefficient and, in turn, its diffusion coefficient on the membrane surface is reduced to nearly half.<sup>44</sup> We collected 14,000 C2A and 3,600 GST-C2A mobile trajectories. Immobile fluorophores that did not exhibit any apparent diffusive motion were excluded from the analysis. The ensemble-averaged MSD  $\langle r^2(t) \rangle$  of C2A monomers and dimer-forming GST-C2A are shown in Figure 4.3b. A deviation from a linear MSD is evident in the figure, showing superdiffusive behavior. Further, the onset of superdiffusion for GST-C2A occurs at a later stage.

The time-averaged MSD  $\overline{\delta^2(\Delta)}$  is often used in the analysis of individual trajectories. Throughout this manuscript we will denote the ensemble average of an observable with brackets  $\langle \cdot \rangle$  and the time average with an overbar  $\bar{\cdot}$ . For a trajectory with  $N$  time points,

$$\overline{\delta^2(\Delta)} = \frac{1}{N-n} \sum_{j=1}^{N-n} [r(j\tau + \Delta) - r(j\tau)]^2 \quad (4.2)$$

where  $\tau$  is the time interval between consecutive measurements and  $n = \Delta/\tau$ . This approach is especially useful when a limited number of trajectories is available, as usually occurs in single-molecule studies. Figure 4.3c shows the time-averaged MSD after it is additionally averaged over all the trajectories. GST-C2A exhibits the expected slower diffusion rate than C2A, based on the MSD slope. As mentioned above, for ergodic processes, the temporal and ensemble averages coincide in the long-time limit,  $\overline{\delta^2(\Delta)} = \langle r^2(t) \rangle$ . However, the ergodic hypothesis breaks down for C2A

molecules. In contrast to the ensemble-averaged MSD, the time-averaged MSD is linear in lag time

$$\overline{\delta^2(\Delta)} \sim \Delta \quad (4.3)$$

Thus, an observer analyzing time-averages would reach the misleading conclusion that the diffusion behavior is not anomalous. The distribution of displacements  $P(r)$  at  $\Delta = 100$  ms is shown in Figs. 4.3d and e for C2A and GST-C2A, respectively. The distribution exhibits two different characteristic regimes: a central part up to a distance  $r \approx 1.5 \mu\text{m}$  and a long tail. This behavior can be understood from the scaling properties of bulk-mediated diffusion as discussed by Bychuk and O'Shaughnessy.<sup>273</sup> Once a molecule dissociates from the surface, it performs a three-dimensional random walk until it returns. In the asymptotic limit, the first return time distribution scales as  $\psi(\tau) \sim \tau^{-1.5}$ . For any given return time, the surface distance between the dissociation and return points has a Gaussian distribution  $P(r_j | \tau) \sim \exp(-(r_j^2)/(4D_B \tau))$ . Therefore, the distribution of jump lengths is  $P(r_j) \sim r_j^{-3}$ , as observed in Figs. 4.3d and e for long distances. The theoretical probability density function of jump lengths can be found using the image method.<sup>274</sup> The distance of first return to the surface are governed by  $P(r) = \gamma_0/2\pi(r^2 + \gamma_0^2)^{3/2}$ , that is a two-dimensional Cauchy distribution. At short times, the probability that the particle performs more than a single jump is small. If we neglect the distance covered by surface diffusion within time intervals at which the particle undergoes a bulk excursion, the motion at each short interval is either by surface diffusion or via a jump. We can then approximate the distribution of displacements at short times by

$$P(r) = \omega \frac{\gamma_0}{2\pi(r^2 + \gamma_0^2)^{3/2}} + \frac{(1 - \omega)}{2\pi r^2} \exp\left(\frac{-r^2}{2\sigma^2}\right) \quad (4.4)$$

where  $\omega$  is the probability that the particle hops within the given time and surface diffusion yields  $\sigma^2 = 2D_s t$ . A least-square fitting of the distribution of displacements (Figs. 4.3d and e) to this propagator yields  $D_s = 1.7 \mu\text{m}^2/\text{s}$  for C2A monomers and  $D_s = 1.0 \mu\text{m}^2/\text{s}$  for GST-C2A. The parameter  $\gamma$  is found to be  $0.24 \mu\text{m}$  and  $0.12 \mu\text{m}$  for C2A and GST-C2A, respectively. The distribution of displacements for longer times involves both a random number of jumps, each having a Cauchy distribution, and the Brownian motion on the surface. Chechkin *et al* derived the full solution for the propagator of bulk-mediated diffusion.<sup>275</sup> For the case when  $D_s = 0$  and neglecting long distance corrections, the distribution of displacements is given by the Cauchy propagator, in agreement with scaling arguments<sup>273</sup>,

$$P(r) = \frac{\gamma t}{2\pi[r^2 + (\gamma t)^2]^{3/2}} \quad (4.5)$$

When the particles also diffuse on the surface, i.e.  $D_s \neq 0$ , the probability density of the displacements is given by the convolution of equation (5) with a normal distribution. Even though the full solution for long times is complicated, the tail of this distribution for large distances still scales as  $P(r) \sim r^{-3}$ . Due to this asymptotic behavior, the exact distribution has similar properties to the Cauchy distribution.

### **4.3.2. NUMERICAL SIMULATIONS: DIFFUSION IN THE PRESENCE OF BULK EXCURSIONS**

In order to verify the model of surface diffusion in the presence of bulk excursions we analyzed numerical simulations of the process diagrammed in Figure 4.1. Molecules perform a two-dimensional random walk, but at random times they

jump due to a hypothetical bulk excursion. The surface residence times are assumed to be independent and identically distributed exponential random variables and the jumps are modelled according to the first return time to the surface given simple diffusion in a three-dimensional medium. These simulations are analyzed in the same way as with experimental observations of the motion of membrane-targeting C2 domains on supported membranes. 500 realizations were simulated off-lattice with a surface diffusion coefficient  $D_s = 0.5$  and a dissociation coefficient  $k = 0.1$ . The chosen parameters do not intend to capture the real protein properties, but to simply test theoretical predictions without the effects of experimental noise. The displacements for two-dimensional diffusion are drawn from a Gaussian distribution with variance  $\sigma_s^2 = 1$  and the return times from bulk excursions are drawn from a distribution  $\psi(tb) = z_0(4\pi D_b t_b^3)^{-1/2} \exp(-z_0^2/4D_b t_b)$ .<sup>274</sup> Then the jump distances are drawn from a Gaussian distribution with variance  $\sigma_b^2 = 2D_b t_b$ .

The distribution of displacements  $P(r)$  for the numerical simulations is shown in Figure 4.4a. As expected, there are two regimes: a central Gaussian part due to the two-dimensional diffusion on the membrane between bulk excursions, and a heavy tail that arises from the long-distance behavior of bulk excursions. The distributions for short times can again be modelled with a propagator that includes contributions from Gaussian surface diffusion and a Cauchy distribution due to bulk excursions. By fitting to equation (4), it is found  $D_s = 0.50 \pm 0.05$  (the value employed in the simulations is  $D_s = 0.5$ ) and  $\gamma_0 = 0.75$ .

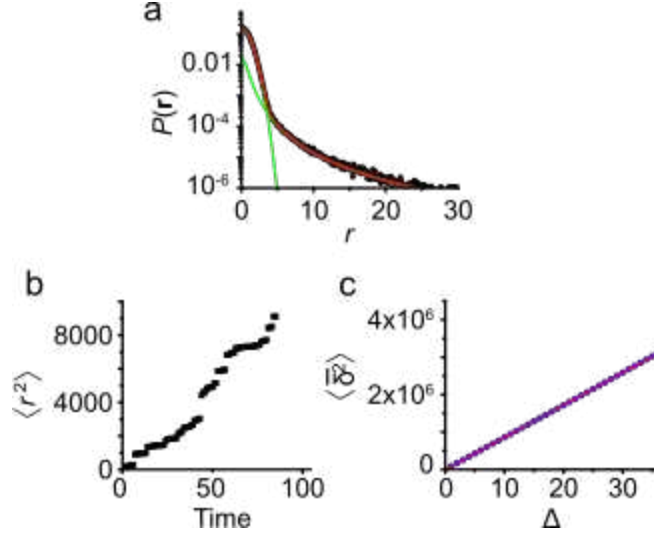


Figure 4.4: Numerical simulations of Lévy flights. 500 realizations were performed, in which a particle alternates between 2D random walks and bulk-mediated jumps. (a) Probability density of the tracer displacements. The density is well described by a theoretical model that includes a Gaussian central part and a Cauchy propagator of the form  $\gamma_0/(r^2 + \gamma_0^2)^{3/2}$ . (b) Ensemble-averaged MSD  $\langle r^2(t) \rangle$  as a function of time. The ensemble-averaged MSD is computed from the distance covered by the tracer in a time  $t$  from the start of the realization. (c) The time-averaged MSD  $\overline{\delta^2(\Delta)}$  is averaged over all realizations and plot against lag time  $\Delta$ .

### 4.3.3. MSD ANALYSIS

---

The dynamics of a particle with a Cauchy propagator are particularly interesting because the theoretical variance of the displacements diverges,

$$\langle r^2(t) \rangle = \int_0^{\infty} (2\pi r) r^2 P(r) dr = \infty \quad (4.6)$$

In practice, a diverging second moment implies that there is a non-negligible probability for the occurrence of extremely long jumps and this phenomenon has direct implications in the measured MSD. Figure 4b shows the ensemble-averaged MSD computed from the numerical simulations. The MSD increases in a superlinear fashion, i.e. by employing equation (4.1), we have  $\alpha > 1$ , which implies the process is

superdiffusive. Let us now analyze the unexpected MSD behavior, starting from the time-averaged MSD of individual trajectories. We can show that the time-averaged MSD is linear in lag time for any random walk with independent increments  $u_i = r_i + 1 - r_i$ , such that  $\langle u_i \cdot u_j \rangle = 0$  when  $i \neq j$ . From the definition of the time averaged MSD (equation (4.2))<sup>276</sup>,

$$\overline{\delta^2(\Delta)} = \frac{1}{N-n} \sum_{i=0}^{N-n} \left( \sum_{k=i}^{i+n} u_k \right)^2 \quad (4.7)$$

$$\approx \frac{1}{N-n} \sum_{i=0}^{N-n} \sum_{k=i}^{i+n} u_k^2 \quad (4.8)$$

$$\approx \frac{\Delta}{t} \sum_{i=0}^{N-n} u_i^2 \quad (4.9)$$

where we have used the approximation that  $t \gg \Delta$ , we omitted the term  $\sum_i \sum_{j \neq i} u_i \cdot u_j$  because it is zero on average, and again we have used the parameter  $n = \Delta/\tau$ . Therefore, we see that for symmetric random walks with independent increments, the time-averaged MSD is linear as observed in Figs. 3c and 4c. Although the time-averaged MSD for individual trajectories is linear, the ensemble averaged MSD  $\langle r^2(t) \rangle$  is not. We can understand the superdiffusive behaviour by assuming we can define the motion in terms of two independent processes  $r(t) = b(t) + y(t)$ , where  $b(t)$  is a two-dimensional Brownian motion and  $y(t)$  is a Lévy process with a probability density defined by equation (4.5). Then the MSD is  $\langle r^2 \rangle = \langle b^2 \rangle + \langle y^2 \rangle$ . The first term is linear in time, but the second term has a superdiffusive nature.<sup>273,275,277</sup>

#### 4.4. DISCUSSION

---

The propagator for surface diffusion in the presence of bulk-mediated jumps (equation (4.4)) depends on the surface diffusion coefficient  $D_s$  and the parameter  $\gamma$  that reflects the transition between the surface and the bulk phase. Namely,  $\gamma \sim a/\tau_{des}$ , where  $\tau_{des}$  is the mean desorption time and  $a$  is a dimensional factor. Bulk-mediated diffusion thus predicts  $\gamma_{dimer} < \gamma_{monomer}$ , in agreement with the values we find for C2A and GST- C2A.

The surface motion of these membrane-targeting domains is well described by Lévy flights, a random walk where the step displacements have a heavy-tailed distribution. The heavy tail arises from the dissociation of molecules from the membrane, which then perform a three-dimensional random walk until they reach the surface again at another location. The process involves the first return to a surface and it converges to a power law according to the Sparre-Andersen theorem.<sup>274</sup> This type of Lévy flight dynamics is fundamentally different from Lévy walks induced by molecular motors in the cytoplasm because periods of active motion require an energy input, typically in the form of ATP hydrolysis, while bulk excursions occur spontaneously.

One of the most interesting effects of the observed bulk-mediated diffusion statistics is that the ensemble-averaged MSD exhibit superdiffusive behavior, whereas the temporal averages suggest normal diffusion. This nonergodic behavior is similar to that of continuous time random walks (CTRW) where the sojourn time distribution between steps has a probability distribution that is heavy-tailed. Also, in

the CTRW,  $\overline{\delta^2(\Delta)} \sim \Delta$  and  $\langle r^2(t) \rangle \sim t_\alpha$ , albeit the CTRW is subdiffusive with  $\alpha < 1$ . The difference in the behavior of temporal and ensemble averages is the key signature of weak ergodicity breaking in the process.<sup>278</sup>

To date, different groups have observed normal diffusion for membrane proteins in supported lipid bilayers, which appear to contradict our findings.<sup>279-282</sup> There are several reasons for this apparent discrepancy. Single-particle tracking in lipid bilayers often focuses on time-averaged MSD, which does not show any non-linearity in lag time. Thus, it would be reasonable to reach the conclusion that diffusion is not anomalous. Furthermore, anomalous diffusion in supported bilayers is known to develop as a result of packing and crowding. These mechanisms are modelled by a fractional Langevin equation, which is ergodic in nature, with anomalies that show up in the time averages. The distribution of displacements has also been previously reported as exhibiting Gaussian behavior. Here we report on the motion of surface-bound membrane domains that exhibit desorption from the membrane within the experimental observation time. The behavior of transmembrane proteins or lipids is very different because the free energy barrier for release from the membrane is too high to be observed within the constraints of experimental observations.<sup>279-281</sup> Previous works dealing with membrane-targeting domains such as C2 have generally been limited to short displacements in order to exclude the effect of long bulk-mediated jumps in diffusion measurements.<sup>44,282</sup>

What are the biological implications of surface superdiffusion for peripheral membrane proteins? Search processes are ubiquitous in cell biology and it is feasible

to assume that evolution has optimized search parameters. For signaling molecules delivered to the plasma membrane during a specific stimulus, the target molecule is often scarce in a sea of other lipids and proteins. Thus, we can envision that if a molecule does not find its target in a given time, it becomes more efficient to start searching at a different location. Is it appropriate then to assume Lévy flights yield the optimal search for sparse targets when compared to Brownian motion? For one-dimensional intermittent processes that switch between Brownian motion and ballistic relocation phases, it has been shown that the search process is significantly more efficient when relocation times are power-law distributed, resulting in a Lévy walk.<sup>283</sup> Notably, when Lévy dynamics are employed, the search is less sensitive to the target density.<sup>283</sup> In general, the optimal strategy depends on the average target distance from the starting point.<sup>284</sup> However, blind searches inside a living cell are very different from a search in an unobstructed environment. Several aspects provide additional complexities in the plasma membrane, in particular.<sup>243</sup> Experimental measurements show that the plasma membrane is compartmentalized in a way that proteins and lipids have the tendency to remain transiently confined within small regions.<sup>285</sup> Further, membrane proteins typically exhibit subdiffusion with anti-persistent increments where molecules drift towards the locations that they visited in the past. While this subdiffusive behavior provides the opportunity for a thorough and compact search, it is definitely not the optimum situation to find sparse targets. A superdiffusive Lévy flight provides a mechanism to overcome the effects of anti-

persistent correlated sub- diffusive motion. Thus, we expect Lévy flight dynamics to often outperform a Brownian search.

The obstruction to the diffusion of membrane molecules has two different sources, both of them causing anti-persistent correlations in the random walk. On one hand, obstacles can be introduced by immobile transmembrane proteins which affect all lipids and membrane proteins. On the other hand, a more severe obstruction can be caused by cytoskeleton components that may not be in direct contact with the plasma membrane.<sup>286</sup> The effect of these barriers is not equal for all membrane proteins. Proteins that have large intracellular complexes are blocked much more efficiently than small molecules. In cases where a large signaling molecule adheres to the membrane via phospholipid-binding domains, bulk excursions allow for the exploration of larger areas. Otherwise, the molecule would remain confined for long times within cytoskeleton-formed corrals, even when no substrate target is found within this region.

In summary, we have observed the nonergodic, superdiffusive motion of membrane-targeting peptide domains in supported lipid bilayers. The motion is well-described by Lévy flights with jumps that have a heavy- tail distribution. The long jumps are caused by excursions into the liquid bulk. After dissociating from the membrane, the molecules diffuse in three dimensions until they reach the membrane again and bind at a new location. Diffusion in the liquid bulk is much faster than diffusion in the membrane, therefore we do not consider the delay time between dissociation and readsorption. The surface distances covered by jumps have a Cauchy

distribution, which is responsible for the heavy tail in the superdiffusive Lévy flights. Model membranes provide an elegant system to study the effect of superdiffusive Lévy flights because they are not subjected to the interactions with other cell components that would mask its experimental observation. However, hopping was already observed on the surface of live cells<sup>239</sup> and we foresee these processes have broad physiological relevance in the surface diffusion of signaling molecules.

## 5. CHAPTER 5: CONCLUSION

---

The work described in the previous chapters highlights mechanisms related to different cellular signaling events that can be characterized by a random walk. In all of the work described, particle diffusion is occurring in what can be considered a trapping potential. The optical trap presents a 3-dimensional harmonic trapping potential, whereas the supported lipid bilayers represents a weak 1-dimensional trapping potential. In both cases, if an external force is strong enough, the particle will exit the trap and undergo Brownian motion within a bulk fluid, potentially being trapped again. In the case of the lipid bilayers, this presents an evolutionarily optimized method for search and capture of signaling particles.

The optical tweezers measurements, however, use the trapping potential to directly measure forces indirectly providing understanding of cellular signaling processes. Measurements of membrane tethering forces and viscoelasticity describe the biomechanical properties of the cellular membrane as well as the propensity for memory of previous stressing events. Stressing events can even directly induce a cellular response that was seen in the form of tugging and potential cleaving of tethers. Membrane blebbing is also a cellular response that produces direct force changes that have also been measured providing an indication of the subsequent stress placed on the nuclear membrane. Measurements under flow in the bloodstream provide insight into the biomechanical shearing and stretching forces that work

cohesively to produce a normal vessel architecture as well as providing insight into disease-based processes.

Overall, this body of work illustrates the development of novel tools to track single particles and extract useful information from biased and unbiased random walk processes. An optical tweezers setup was built, validated, and used to directly measure static and dynamic forces. Image based particle tracking algorithms were developed/improved to extract the information needed to make the measurements. A TIRFM setup was completely reworked, realigned, and adapted to accommodate the synthetic lipid bilayer experiments. The methods and experiments developed yielded valuable information on membrane biophysical properties and the dynamics associated on, in, or around the membrane itself. The work further shows that which is already known: the cellular membrane is key to the functional processes related to life as we know it and there is much more that we can learn by studying it and its biophysical properties that may lead or correlate to disease processes.

## WORKS CITED

---

1. Simons, G. F. and C. D. F. in *Ethnologue: Languages of the World, Twentieth edition* (SIL International, 2017).
2. Evans, D. A. & Green, C. L. Insect attractants of natural origin. *Chem. Soc. Rev.* **2**, 75 (1973).
3. Porter, S. L., Wadhams, G. H. & Armitage, J. P. Signal processing in complex chemotaxis pathways. *Nat. Rev. Microbiol.* **9**, 153–165 (2011).
4. Hazelbauer, G. L. Bacterial Chemotaxis: The Early Years of Molecular Studies. *Annu. Rev. Microbiol.* **66**, 285–303 (2012).
5. Hodgkin, A. L. & Katz, B. The effect of sodium ions on the electrical activity of the giant axon of the squid. *J. Physiol.* **108**, 37–77 (1949).
6. Enver, T. *et al.* Cellular differentiation hierarchies in normal and culture-adapted human embryonic stem cells. *Hum. Mol. Genet.* **14**, 3129–3140 (2005).
7. Chamberlain, G., Fox, J., Ashton, B. & Middleton, J. Concise Review: Mesenchymal Stem Cells: Their Phenotype, Differentiation Capacity, Immunological Features, and Potential for Homing. *Stem Cells* **25**, 2739–2749 (2007).
8. Streuli, C. Extracellular matrix remodelling and cellular differentiation. *Curr. Opin. Cell Biol.* **11**, 634–640 (1999).
9. Gattazzo, F., Urciuolo, A. & Bonaldo, P. Extracellular matrix: A dynamic microenvironment for stem cell niche. *Biochim. Biophys. Acta - Gen. Subj.*

- 1840, 2506–2519 (2014).
10. Wolpert, L. Positional information and the spatial pattern of cellular differentiation. *J. Theor. Biol.* **25**, 1–47 (1969).
  11. Henkel, A. W. *et al.* Light-induced exocytosis in cell development and differentiation. *J. Cell. Biochem.* **97**, 1393–1406 (2006).
  12. Zou, G.-M., Chen, J.-J. & Ni, J. LIGHT induces differentiation of mouse embryonic stem cells associated with activation of ERK5. *Oncogene* **5**, 463–469 (2005).
  13. Tsien, R. Y. THE GREEN FLUORESCENT PROTEIN. *Annu. Rev. Biochem.* **67**, 509–544 (1998).
  14. Chudakov, D., Matz, M., Lukyanov, S. & Lukyanov, K. Fluorescent Proteins and Their Applications in Imaging Living Cells and Tissues. *Physiol. Rev.* **90**, 1103–1163 (2010).
  15. Snapp, E. in *Current Protocols in Cell Biology* (John Wiley & Sons, Inc., 2005). doi:10.1002/0471143030.cb2104s27
  16. Mehrer, H. & Stolwijk, N. Heroes and Highlights in the History of Diffusion. *Diffus. Fundam.* **11**, 1–32 (2009).
  17. Bray, D. Signaling complexes: biophysical constraints on intracellular communication. *Annu. Rev. Biophys. Biomol. Struct.* **27**, 59–75 (1998).
  18. Lippincott-Schwartz, J., Snapp, E. & Kenworthy, A. Studying protein dynamics in living cells. *Nat. Rev. Mol. Cell Biol.* **2**, 444–456 (2001).
  19. Elf, J., Doncic, A. & Ehrenberg, M. Mesoscopic reaction-diffusion in

- intracellular signaling. in (eds. Bezrukov, S. M., Frauenfelder, H. & Moss, F.)  
**5110**, 114 (2003).
20. Lajoie, P., Goetz, J. G., Dennis, J. W. & Nabi, I. R. Lattices, rafts, and scaffolds: domain regulation of receptor signaling at the plasma membrane. *J. Cell Biol.* **185**, 381–385 (2009).
  21. Kholodenko, B. N. Four-dimensional organization of protein kinase signaling cascades: the roles of diffusion, endocytosis and molecular motors. *J. Exp. Biol.* **206**, 2073–2082 (2003).
  22. States, U. Roles of Diffusion Dynamics and Molecular Concentration Gradients in Cellular Differentiation and Three- Dimensional Tissue Development Richard J. McMurtrey, MD, MSc. 1–21
  23. Verkman, A. S. Solute and macromolecule diffusion in cellular aqueous compartments. *Trends Biochem. Sci.* **27**, 27–33 (2002).
  24. Bhalla, U. S. Signaling in small subcellular volumes. {II.} Stochastic and diffusion effects on synaptic network properties. *Biophys. J.* **87**, 745–753 (2004).
  25. Brown, R. XXVII. *A brief account of microscopical observations made in the months of June, July and August 1827, on the particles contained in the pollen of plants; and on the general existence of active molecules in organic and inorganic bodies.* *Philos. Mag. Ser. 2* **4**, 161–173 (1828).
  26. Society, R. Additional Observations on the Diffusion of Liquids . [ Abstract ]  
 Author ( s ): Thomas Graham Source : Abstracts of the Papers Communicated

to the Royal Society of London , Vol . 6 Published by : Royal Society Stable  
URL : <http://www.jstor.org/stable/111>. **6**, 70–72 (2017).

27. Fick, A. V. On liquid diffusion. *Philos. Mag.* **10**, 30–39 (1855).
28. Fick, A. On liquid diffusion. *J. Memb. Sci.* **100**, 33–38 (1995).
29. Philibert, J. One and a half century of diffusion: Fick, Einstein, before and beyond. *Diffus. Fundam.* **4**, 1–19 (2005).
30. Gouy. Note sur le mouvement brownien. *J. Phys. Théorique Appliquée* **7**, 561–564 (1888).
31. Nelson, P. *Biological Physics. Energy, Information, Life.* (2008).
32. Everitt, B. *Chance rules: An informal guide to probability, risk and statistics.* *Chance Rules: An Informal Guide to Probability, Risk and Statistics* (Springer Science+Business Media, LLC, 2008). doi:10.1007/978-0-387-77415-2
33. Codling, E. A., Plank, M. J. & Benhamou, S. Random walk models in biology. *J. R. Soc. Interface* **5**, 813–834 (2008).
34. Smoluchowski, M. von. Zur kinetischen Theorie der Brownschen Molekularbewegung und der Suspension. *Ann. Phys.* **21**, 756–780 (1906).
35. Fulinski, A. On Marian Smoluchowski 's Life and Contribution To Physics. *Acta Phys. Pol. B* **29**, 1523–1537 (1998).
36. Einstein, A. On the Motion of Small Particles Suspended in a Stationary Liquid, as Required by the Molecular Kinetic Theory of Heat. *Ann. Phys.* **322**, 549–560 (1905).
37. Vlahos, L., Isliker, H., Kominis, Y. & Hizanidis, K. Normal and Anomalous

- Diffusion: A Tutorial. 1–39 (2008). at <<http://arxiv.org/abs/0805.0419>>
38. Seol, Y., Li, J., Nelson, P. C., Perkins, T. T. & Betterton, M. D. Elasticity of short DNA molecules: Theory and experiment for contour lengths of 0.6–7  $\mu\text{m}$ . *Biophys. J.* **93**, 4360–4373 (2007).
  39. Richardson, A. C., Reihani, S. N. S. & Oddershede, L. B. Non-harmonic potential of a single beam optical trap. *Opt. Express* **16**, 15709–15717 (2008).
  40. Kuo, S. & Sheetz, M. Force of single kinesin molecules measured with optical tweezers. *Science (80-. )*. **260**, 232–234 (1993).
  41. Lindner, M., Nir, G., Vivante, A., Young, I. T. & Garini, Y. Dynamic analysis of a diffusing particle in a trapping potential. *Phys. Rev. E* **87**, 022716 (2013).
  42. Smoluchowski, M. von & von Smoluchowski, M. Zur kinetischen Theorie der Brownschen Molekularbewegung und der Suspensionen. *Ann. Phys.* **326**, 756–780 (1906).
  43. Schulten, K. & Kosztin, I. *Lectures in Theoretical Biophysics. Lectures in Theoretical Biophysics* (2000). at <<http://www.ks.uiuc.edu/Services/Class/NSM.pdf>>
  44. Knight, J. D., Lerner, M. G., Marcano-Velázquez, J. G., Pastor, R. W. & Falke, J. J. Single Molecule Diffusion of Membrane-Bound Proteins: Window into Lipid Contacts and Bilayer Dynamics. *Biophys. J.* **99**, 2879–2887 (2010).
  45. Ziemba, B. P., Knight, J. D. & Falke, J. J. Assembly of Membrane-Bound Protein Complexes: Detection and Analysis by Single Molecule Diffusion. *Biochemistry* **51**, 1638–1647 (2012).

46. Walsh, D. a & Doolittle, W. F. The real ‘domains’ of life. *Curr. Biol.* **15**, R237–R240 (2005).
47. Berg, T. Inhibition of transcription factors with small organic molecules. *Curr. Opin. Chem. Biol.* **12**, 464–471 (2008).
48. Liyanage, V. *et al.* DNA Modifications: Function and Applications in Normal and Disease States. *Biology (Basel)*. **3**, 670–723 (2014).
49. Kim, T. K. & Eberwine, J. H. Mammalian cell transfection: The present and the future. *Anal. Bioanal. Chem.* **397**, 3173–3178 (2010).
50. Houseley, J. & Tollervey, D. The Many Pathways of RNA Degradation. *Cell* **136**, 763–776 (2009).
51. Ghildiyal, M. & Zamore, P. D. Small silencing RNAs: An expanding universe. *Nat. Rev. Genet.* **10**, 94–108 (2009).
52. Wan Makhtar, W. R. *et al.* Short stretches of rare codons regulate translation of the transcription factor ZEB2 in cancer cells. *Oncogene* **36**, 6640–6648 (2017).
53. Popis, M. C., Blanco, S. & Frye, M. Posttranscriptional methylation of transfer and ribosomal RNA in stress response pathways, cell differentiation, and cancer. *Curr. Opin. Oncol.* **28**, 65–71 (2016).
54. Fustin, J. M. *et al.* XRNA-methylation-dependent RNA processing controls the speed of the circadian clock. *Cell* **155**, 793–806 (2013).
55. Weiss, W. A., Taylor, S. S. & Shokat, K. M. Recognizing and exploiting differences between RNAi and small-molecule inhibitors. *Nat. Chem. Biol.* **3**,

- 739–744 (2007).
56. Seidler, J., McGovern, S. L., Doman, T. N. & Shoichet, B. K. Identification and prediction of promiscuous aggregating inhibitors among known drugs. *J. Med. Chem.* **46**, 4477–4486 (2003).
  57. Frye, S. V. The art of the chemical probe. *Nat. Chem. Biol.* **6**, 159–161 (2010).
  58. Smith, M. H., Ploegh, H. L. & Weissman, J. S. Road to Ruin: Targeting Proteins for Degradation in the Endoplasmic Reticulum. *Science (80-. )*. **334**, 1086–1090 (2011).
  59. Shimomura, O., Johnson, F. H. & Saiga, Y. Extraction, Purification and Properties of Aequorin, a Bioluminescent Protein from the Luminous Hydromedusan, Aequorea. *J. Cell. Comp. Physiol.* **59**, 223–239 (1962).
  60. Prasher, D. C., Eckenrode, V. K., Ward, W. W., Prendergast, F. G. & Cormier, M. J. Primary structure of the Aequorea victoria green-fluorescent protein. *Gene* **111**, 229–233 (1992).
  61. Kikuchi, K. Design, synthesis and biological application of chemical probes for bio-imaging. *Chem. Soc. Rev.* **39**, 2048–2053 (2010).
  62. Lavis, L. D. & Raines, R. T. Bright Ideas for Chemical Biology. *ACS Chem. Biol.* **3**, 142–155 (2008).
  63. Guo, T. & Fang, Y. Functional organization and dynamics of the cell nucleus. *Front. Plant Sci.* **5**, 1–12 (2014).
  64. Fletcher, D. A. & Mullins, R. D. Cell mechanics and the cytoskeleton. *Nature* **463**, 485–492 (2010).

65. Lombard, J. Once upon a time the cell membranes: 175 years of cell boundary research. *Biol. Direct* **9**, 32 (2014).
66. Schafer, K. A. The Cell Cycle: A Review. *Vet. Pathol.* **35**, 461–478 (1998).
67. CHARRAS, G. T. A short history of blebbing. *J. Microsc.* **231**, 466–478 (2008).
68. Tinevez, J.-Y. *et al.* Role of cortical tension in bleb growth. *Proc. Natl. Acad. Sci.* **106**, 18581–18586 (2009).
69. Charras, G. T., Hu, C.-K., Coughlin, M. & Mitchison, T. J. Reassembly of contractile actin cortex in cell blebs. *J. Cell Biol.* **175**, 477–490 (2006).
70. Sekyrova, P., Östblom, J. & Andäng, M. Blebbing as a physical force in cancer EMT – Parallels with mitosis. *Semin. Cancer Biol.* **22**, 369–373 (2012).
71. Fackler, O. T. & Grosse, R. Cell motility through plasma membrane blebbing. *J. Cell Biol.* **181**, 879–884 (2008).
72. Discher, D. E., Mooney, D. J. & Zandstra, P. W. Growth Factors, Matrices, and Forces Combine and Control Stem Cells. *Science (80-. ).* **324**, 1673–1677 (2009).
73. Freund, J. B., Goetz, J. G., Hill, K. L. & Vermot, J. Fluid flows and forces in development: functions, features and biophysical principles. *Development* **139**, 3063–3063 (2012).
74. Pedersen, J. A., Lichter, S. & Swartz, M. A. Cells in 3D matrices under interstitial flow: Effects of extracellular matrix alignment on cell shear stress and drag forces. *J. Biomech.* **43**, 900–905 (2010).
75. Heng, B. C. *et al.* An overview and synopsis of techniques for directing stem

- cell differentiation in vitro. *Cell Tissue Res.* **315**, 291–303 (2004).
76. Obradovic, B., Radisic, M. & Vunjak-Novakovic, G. in (eds. Shastri, V. P., Altankov, G. & Lendlein, A.) 115–129 (Springer Netherlands, 2010).  
doi:10.1007/978-90-481-8790-4\_7
77. Singer, A. S. J. & Nicolson, G. L. The Fluid Mosaic Model of the Structure of Cell Membranes Published by : American Association for the Advancement of Science Stable URL : <http://www.jstor.org/stable/1733071> REFERENCES  
Linked references are available on JSTOR for this article : You may ne. **175**, 720–731 (2017).
78. Przystalski, S. *et al.* Influence of amphiphilic compounds on membranes. *Acta Biochim. Pol.* **47**, 627–638 (2000).
79. Gorter, E. & Grendel, F. on Bimolecular Layers of Lipoids on the Chromocytes of the Blood. *J. Exp. Med.* **41**, 439–443 (1925).
80. Pohorille, A., Schweighofer, K. & Wilson, M. A. The origin and early evolution of membrane channels. *Astrobiology* **5**, 1–17 (2005).
81. Hong, M., Zhang, Y. & Hu, F. Membrane Protein Structure and Dynamics from NMR Spectroscopy. *Annu. Rev. Phys. Chem.* **63**, 1–24 (2012).
82. Cournia, Z. *et al.* Membrane Protein Structure, Function, and Dynamics: a Perspective from Experiments and Theory. *J. Membr. Biol.* **248**, 611–640 (2015).
83. Muller, D. J., Wu, N. & Palczewski, K. Vertebrate Membrane Proteins: Structure, Function, and Insights from Biophysical Approaches. *Pharmacol.*

- Rev.* **60**, 43–78 (2008).
84. Engel, A. & Gaub, H. E. Structure and Mechanics of Membrane Proteins. *Annu. Rev. Biochem.* **77**, 127–148 (2008).
85. Salbreux, G., Charras, G. & Paluch, E. Actin cortex mechanics and cellular morphogenesis. *Trends Cell Biol.* **22**, 536–545 (2012).
86. Nawaz, S. *et al.* Cell Visco-Elasticity Measured with AFM and Optical Trapping at Sub-Micrometer Deformations. *PLoS One* **7**, e45297 (2012).
87. Karcher, H. *et al.* A Three-Dimensional Viscoelastic Model for Cell Deformation with Experimental Verification. *Biophys. J.* **85**, 3336–3349 (2003).
88. Roh-Johnson, M., Sullivan-Brown, J. & Goldstein, B. in *Actin-based Motility* 187–209 (Springer Netherlands, 2010). doi:10.1007/978-90-481-9301-1\_8
89. Wang, J. H.-C. & Lin, J.-S. Cell traction force and measurement methods. *Biomech. Model. Mechanobiol.* **6**, 361–371 (2007).
90. Polio, S. R., Rothenberg, K. E., Stamenović, D. & Smith, M. L. A micropatterning and image processing approach to simplify measurement of cellular traction forces. *Acta Biomater.* **8**, 82–88 (2012).
91. Brizzi, M. F., Tarone, G. & Defilippi, P. Extracellular matrix, integrins, and growth factors as tailors of the stem cell niche. *Current Opinion in Cell Biology* **24**, 645–651 (2012).
92. Suresh, S. Biomechanics and biophysics of cancer cells. *Acta Biomater.* **3**, 413–38 (2007).

93. Potter, C. M. F., Lao, K. H., Zeng, L. & Xu, Q. Role of Biomechanical Forces in Stem Cell Vascular Lineage Differentiation. *Arterioscler. Thromb. Vasc. Biol.* **34**, 2184–2190 (2014).
94. Merkel, R., Kirchgeßner, N., Cesa, C. M. & Hoffmann, B. Cell Force Microscopy on Elastic Layers of Finite Thickness. *Biophys. J.* **93**, 3314–3323 (2007).
95. Kunitake, T. Synthetic Bilayer Membranes: Molecular Design, Self-Organization, and Application. *Angew. Chemie Int. Ed. English* **31**, 709–726 (1992).
96. Nikolova, G. & Lammert, E. Interdependent development of blood vessels and organs. *Cell Tissue Res.* **314**, 33–42 (2003).
97. Udan, R. S., Culver, J. C. & Dickinson, M. E. Understanding vascular development. *Wiley Interdiscip. Rev. Dev. Biol.* **2**, 327–346 (2013).
98. Bakkers, J. Zebrafish as a model to study cardiac development and human cardiac disease. *Cardiovasc. Res.* **91**, 279–288 (2011).
99. Potente, M. & Mäkinen, T. Vascular heterogeneity and specialization in development and disease. *Nat. Rev. Mol. Cell Biol.* **18**, 477–494 (2017).
100. Jones, E. A. V., le Noble, F. & Eichmann, A. What Determines Blood Vessel Structure? Genetic Preshpecification vs. Hemodynamics. *Physiology* **21**, 388–395 (2006).
101. Simons, M., Gordon, E. & Claesson-Welsh, L. Mechanisms and regulation of endothelial VEGF receptor signalling. *Nat. Rev. Mol. Cell Biol.* **17**, 611–625

- (2016).
102. Simons, M. An Inside View: VEGF Receptor Trafficking and Signaling. *Physiology* **27**, 213–222 (2012).
  103. Wasserman, S. M. *et al.* Gene expression profile of human endothelial cells exposed to sustained fluid shear stress. *Physiol. Genomics* **12**, 13–23 (2002).
  104. Huang, Y., Jia, X., Bai, K., Gong, X. & Fan, Y. Effect of Fluid Shear Stress on Cardiomyogenic Differentiation of Rat Bone Marrow Mesenchymal Stem Cells. *Arch. Med. Res.* **41**, 497–505 (2010).
  105. Glossop, J. R. & Cartmell, S. H. Effect of fluid flow-induced shear stress on human mesenchymal stem cells: Differential gene expression of IL1B and MAP3K8 in MAPK signaling. *Gene Expr. Patterns* **9**, 381–388 (2009).
  106. Hsiao, Y. F., Pan, H. J., Tung, Y. C., Chen, C. C. & Lee, C. H. Effects of hydraulic pressure on cardiomyoblasts in a microfluidic device. *Biomicrofluidics* **9**, 1–10 (2015).
  107. Brooks, A. R., Lelkes, P. I. & Rubanyi, G. M. Gene expression profiling of human aortic endothelial cells exposed to disturbed flow and steady laminar flow. *Physiol. Genomics* **9**, 27–41 (2002).
  108. Lesman, A., Blinder, Y. & Levenberg, S. Modeling of flow-induced shear stress applied on 3D cellular scaffolds: Implications for vascular tissue engineering. *Biotechnol. Bioeng.* **105**, 645–654 (2010).
  109. Phelps, E. A. & García, A. J. Engineering more than a cell: vascularization strategies in tissue engineering. *Curr. Opin. Biotechnol.* **21**, 704–709 (2010).

110. Friedman, M. H., Krams, R. & Chandran, K. B. Flow interactions with cells and tissues: Cardiovascular flows and fluid-structure interactions. *Ann. Biomed. Eng.* **38**, 1178–1187 (2010).
111. Egorova, A. D., van der Heiden, K., Poelmann, R. E. & Hierck, B. P. Primary cilia as biomechanical sensors in regulating endothelial function. *Differentiation* **83**, S56–S61 (2012).
112. Goetz, J. G. *et al.* Endothelial cilia mediate low flow sensing during zebrafish vascular development. *Cell Rep.* **6**, 799–808 (2014).
113. Radi, H. A. . & Rasmussen, J. O. *Principles of Physics. Undergraduate Lecture Notes in Physics* (Springer Berlin Heidelberg, 2013). doi:10.1007/978-3-642-23026-4
114. Renz, M. Fluorescence microscopy-A historical and technical perspective. *Cytom. Part A* **83**, 767–779 (2013).
115. Lebedev, P. N. Experimental Examination of Light Pressure. *Ann. Phys.* **6**, 1–26 (1901).
116. Sredniawa, B. CENTENARY OF FIVE FUNDAMENTAL EINSTEIN ' S PAPERS The juvenile Einstein ' s papers. *Concepts Phys.* **III**, 55–68 (2005).
117. Dimitrova, T. L. & Weis, A. The wave-particle duality of light: A demonstration experiment. *Am. J. Phys.* **76**, 137–142 (2008).
118. George, N. TIRF microscopy: The evanescent wave of the future. *Am. Lab.* **36**, 26–28 (2004).
119. Thompson, N. L. & Lagerholm, B. C. Total internal reflection fluorescence:

- applications in cellular biophysics. *Curr. Opin. Biotechnol.* **8**, 58–64 (1997).
120. Ashkin, A. Acceleration and Trapping of Particles by Radiation Pressure. *Phys. Rev. Lett.* **24**, 156–159 (1970).
  121. Ashkin, A., Dziedzic, J. M., Bjorkholm, J. E. & Chu, S. Observation of a single-beam gradient force optical trap for dielectric particles. *Opt. Lett.* **11**, 288 (1986).
  122. Woerdemann, M. in *Structured Light Fields* 5–26 (2012). doi:10.1007/978-3-642-29323-8\_2
  123. Neuman, K. C. & Block, S. M. Optical trapping. *Rev. Sci. Instrum.* **75**, 2787–809 (2004).
  124. Titushkin, I. & Cho, M. Distinct Membrane Mechanical Properties of Human Mesenchymal Stem Cells Determined Using Laser Optical Tweezers. *Biophys. J.* **90**, 2582–2591 (2006).
  125. Svoboda, K. & Block, S. M. Biological applications of optical forces. *Annu. Rev. Biophys. Biomol. Struct.* **23**, 247–85 (1994).
  126. Hansen, P. M., Tolic-Nørrelykke, I. M., Flyvbjerg, H. & Berg-Sørensen, K. tweezercalib 2.1: Faster version of MatLab package for precise calibration of optical tweezers. *Comput. Phys. Commun.* **175**, 572–573 (2006).
  127. Horst, A. van der & Forde, N. R. Power spectral analysis for optical trap stiffness calibration from high-speed camera position detection with limited bandwidth. *Opt. Express* **18**, 7670–7677 (2010).
  128. Sarshar, M., Wong, W. T. & Anvari, B. Comparative study of methods to

- calibrate the stiffness of a single-beam gradient-force optical tweezers over various laser trapping powers. *J. Biomed. Opt.* **19**, 115001 (2014).
129. Neuman, K. C. & Block, S. M. Optical trapping. *Rev. Sci. Instrum.* **75**, 2787–2809 (2004).
130. Alba, A., Viguera-Gomez, J. F., Arce-Santana, E. R. & Aguilar-Ponce, R. M. Phase correlation with sub-pixel accuracy: A comparative study in 1D and 2D. *Comput. Vis. Image Underst.* **137**, 76–87 (2015).
131. Mahmoudzadeh, A. P. & Kashou, N. H. Evaluation of Interpolation Effects on Upsampling and Accuracy of Cost Functions-Based Optimized Automatic Image Registration. *Int. J. Biomed. Imaging* **2013**, 1–19 (2013).
132. Sabass, B., Gardel, M. L., Waterman, C. M. & Schwarz, U. S. High Resolution Traction Force Microscopy Based on Experimental and Computational Advances. *Biophys. J.* **94**, 207–220 (2008).
133. Toprak, E., Kural, C. & Selvin, P. R. in *Methods in Enzymology* **475**, 1–26 (Elsevier Inc., 2010).
134. Dai, J. & Sheetz, M. P. Mechanical properties of neuronal growth cone membranes studied by tether formation with laser optical tweezers. *Biophys. J.* **68**, 988–996 (1995).
135. Oeckler, R. a *et al.* Determinants of plasma membrane wounding by deforming stress. *Am. J. Physiol. Lung Cell. Mol. Physiol.* **299**, L826-33 (2010).
136. Raucher, D. & Sheetz, M. P. Membrane Expansion Increases Endocytosis Rate

- during Mitosis. *J. Cell Biol.* **144**, 497–506 (1999).
137. Raucher, D. & Sheetz, M. P. Cell Spreading and Lamellipodial Extension Rate Is Regulated by Membrane Tension. *J. Cell Biol.* **148**, 127–136 (2000).
138. Pontes, B. *et al.* Cell Cytoskeleton and Tether Extraction. *Biophys. J.* **101**, 43–52 (2011).
139. Sleep, J., Wilson, D., Simmons, R. & Gratzner, W. Elasticity of the Red Cell Membrane and Its Relation to Hemolytic Disorders: An Optical Tweezers Study. *Biophys. J.* **77**, 3085–3095 (1999).
140. Li, Z. *et al.* Membrane tether formation from outer hair cells with optical tweezers. *Biophys. J.* **82**, 1386–95 (2002).
141. Conroy, R. in *Handbook of Molecular Force Spectroscopy* 23–96 (Springer US, 2008). doi:10.1007/978-0-387-49989-5\_2
142. Guck, J. *et al.* Optical Deformability as an Inherent Cell Marker for Testing Malignant Transformation and Metastatic Competence. *Biophys. J.* **88**, 3689–3698 (2005).
143. Schwingel, M. & Bastmeyer, M. Force Mapping during the Formation and Maturation of Cell Adhesion Sites with Multiple Optical Tweezers. *PLoS One* **8**, e54850 (2013).
144. Suresh, S. Biomechanics and biophysica of cancer cells. *Mater. Sci.* **3**, 413–438 (2010).
145. Raucher, D. & Sheetz, M. P. Characteristics of a Membrane Reservoir Buffering Membrane Tension. *Biophys. J.* **77**, 1992–2002 (1999).

146. Zhang, H. & Liu, K.-K. Optical tweezers for single cells. *J. R. Soc. Interface* **5**, 671–690 (2008).
147. Dai, J. & Sheetz, M. P. Membrane tether formation from blebbing cells. *Biophys. J.* **77**, 3363–3370 (1999).
148. Ndoye, F. *et al.* The influence of lateral forces on the cell stiffness measurement by optical tweezers vertical indentation. *Int. J. Optomechatronics* **10**, 53–62 (2016).
149. Swaminathan, V. *et al.* Mechanical Stiffness Grades Metastatic Potential in Patient Tumor Cells and in Cancer Cell Lines. *Cancer Res.* **71**, 5075–5080 (2011).
150. Laurent, V. M. *et al.* Assessment of Mechanical Properties of Adherent Living Cells by Bead Micromanipulation: Comparison of Magnetic Twisting Cytometry vs Optical Tweezers. *J. Biomech. Eng.* **124**, 408 (2002).
151. Sirbuly, D. J., Friddle, R. W., Villanueva, J. & Huang, Q. Nanomechanical force transducers for biomolecular and intracellular measurements: is there room to shrink and why do it? *Reports Prog. Phys.* **78**, 024101 (2015).
152. Neuman, K. C. & Nagy, A. Single-molecule force spectroscopy: optical tweezers, magnetic tweezers and atomic force microscopy. *Nat. Methods* **5**, 491–505 (2008).
153. Fabry, B. *et al.* Scaling the microrheology of living cells. *Phys. Rev. Lett.* **87**, 1–4 (2001).
154. Kamgoué, A., Ohayon, J. & Tracqui, P. Estimation of Cell Young's Modulus of

- Adherent Cells Probed by Optical and Magnetic Tweezers: Influence of Cell Thickness and Bead Immersion. *J. Biomech. Eng.* **129**, 523 (2007).
155. Bausch, A. R., Ziemann, F., Boulbitch, A. A., Jacobson, K. & Sackmann, E. Local measurements of viscoelastic parameters of adherent cell surfaces by magnetic bead microrheometry. *Biophys. J.* **75**, 2038–2049 (1998).
156. Radmacher, M., Fritz, M., Kacher, C. M., Cleveland, J. P. & Hansma, P. K. Measuring the viscoelastic properties of human platelets with the atomic force microscope. *Biophys. J.* **70**, 556–567 (1996).
157. Brunner, C., Niendorf, A. & Käs, J. A. Passive and active single-cell biomechanics: a new perspective in cancer diagnosis. *Soft Matter* **5**, 2171 (2009).
158. Lekka, M. *et al.* Elasticity of normal and cancerous human bladder cells studied by scanning force microscopy. *Eur. Biophys. J.* **28**, 312–316 (1999).
159. Cross, S. E., Jin, Y. S., Rao, J. & Gimzewski, J. K. Nanomechanical analysis of cells from cancer patients. *Nat. Nanotechnol.* **2**, 780–783 (2007).
160. Sánchez, D. *et al.* Noncontact measurement of the local mechanical properties of living cells using pressure applied via a pipette. *Biophys. J.* **95**, 3017–3027 (2008).
161. Buys, A. V *et al.* Changes in red blood cell membrane structure in type 2 diabetes: a scanning electron and atomic force microscopy study. *Cardiovasc. Diabetol.* **12**, 25 (2013).
162. Savigny, P., Evans, J. & McGrath, K. M. Cell membrane structures during

- exocytosis. *Endocrinology* **148**, 3863–3874 (2007).
163. Muratore, M., Mitchell, S. & Waterfall, M. Plasma membrane characterization, by scanning electron microscopy, of multipotent myoblasts-derived populations sorted using dielectrophoresis. *Biochem. Biophys. Res. Commun.* **438**, 666–672 (2013).
164. Usami, S., Chen, H.-H., Zhao, Y., Chien, S. & Skalak, R. Design and construction of a linear shear stress flow chamber. *Ann. Biomed. Eng.* **21**, 77–83 (1993).
165. Gomez, F. a. Bioanalytical applications in microfluidics. *Bioanalysis* **2**, 1661–1662 (2010).
166. Kim, S., Kim, H. J. & Jeon, N. L. Biological applications of microfluidic gradient devices. *Integr. Biol.* **2**, 584 (2010).
167. Lee, K., Kinnunen, M., Lugovtsov, A. E., Priezhev, A. V. & Karmenyan, A. V. Optical study of the dynamics and deformation of erythrocytes in the flow. *Optoelectron. Instrum. Data Process.* **50**, 519–524 (2014).
168. Otten, M. Microfluidic and microrheological studies of protein interactions at the single-molecule and single-cell level. (Ludwig Maximilian University of Munich, 2014).
169. Pemberton, R. *et al.* Fabrication and Evaluation of a Micro(Bio)Sensor Array Chip for Multiple Parallel Measurements of Important Cell Biomarkers. *Sensors* **14**, 20519–20532 (2014).
170. Streets, A. M. & Huang, Y. Microfluidics for biological measurements with

- single-molecule resolution. *Curr. Opin. Biotechnol.* **25**, 69–77 (2014).
171. Mathew, M. *et al.* Pick it up with light! An advanced summer program for secondary school students. in *Proceedings of SPIE* (eds. Martins Costa, M. F. P. C. & Zghal, M.) **9289**, 92892U (2014).
172. Ashkin, A. Acceleration and Trapping of Particles by Radiation Pressure. **1**, 1–10 (2006).
173. Nicholas, M. P. *et al.* Control of cytoplasmic dynein force production and processivity by its C-terminal domain. *Nat. Commun.* **6**, (2015).
174. Block, S. M., Goldstein, L. S. B. & Schnapp, B. J. Bead movement by single kinesin molecules studied with optical tweezers. *Nature* **348**, 348–352 (1990).
175. Watanabe, T. M., Iwane, A. H., Tanaka, H., Ikebe, M. & Yanagida, T. Mechanical characterization of one-headed Myosin-V using optical tweezers. *PLoS One* **5**, (2010).
176. Kuo, S. C. & Sheetz, M. P. Force of Single Kinesin Molecules Measured With Optical Tweezers Author ( s ): Scot C . Kuo and Michael P . Sheetz Published by : American Association for the Advancement of Science Stable URL : <http://www.jstor.org/stable/2881316> JSTOR is a not-for-profi. **260**, 232–234 (2017).
177. Larson, M. H., Landick, R. & Block, S. M. Single-Molecule Studies of RNA Polymerase: One Singular Sensation, Every Little Step It Takes. *Mol. Cell* **41**, 249–262 (2011).
178. Block, S. M. *et al.* Molecule by molecule, the physics and chemistry of life:

- SMB 2007. *Nat. Chem. Biol.* **3**, 193–197 (2007).
179. Williams, M. C. Optical Tweezers : Measuring Piconewton Forces. *Physics (College. Park. Md)*. 1–14 (2002). at  
<<http://scholar.google.com/scholar?hl=en&btnG=Search&q=intitle:Optical+Tweezers+:+Measuring+Piconewton+Forces#0>>
180. Courson, D. S. & Rock, R. S. Fast Benchtop Fabrication of Laminar Flow Chambers for Advanced Microscopy Techniques. *PLoS One* **4**, e6479 (2009).
181. Tsai, J.-W. *et al.* Applications of Optical Tweezers and an Integrated Force Measurement Module for Biomedical Research. in *Proceedings of SPIE* (eds. Alfano, R. R., Ho, P.-P. & Chiou, A. E. T.) 213–221 (2000). doi:ADP010487
182. Koster, G., Cacciuto, A., Derényi, I., Frenkel, D. & Dogterom, M. Force Barriers for Membrane Tube Formation. *Phys. Rev. Lett.* **94**, 068101 (2005).
183. Ashok, P. C. & Dholakia, K. Optical trapping for analytical biotechnology. *Curr. Opin. Biotechnol.* **23**, 16–21 (2012).
184. Lenormand, G., Hénon, S., Richert, A., Siméon, J. & Gallet, F. Direct Measurement of the Area Expansion and Shear Moduli of the Human Red Blood Cell Membrane Skeleton. *Biophys. J.* **81**, 43–56 (2001).
185. Mizuno, D., Bacabac, R., Tardin, C., Head, D. & Schmidt, C. F. High-resolution probing of cellular force transmission. *Phys. Rev. Lett.* **102**, 1–4 (2009).
186. Chen, K., Qin, Y., Zheng, F., Sun, M. & Shi, D. Diagnosis of colorectal cancer using Raman spectroscopy of laser-trapped single living epithelial cells. *Opt.*

- Lett.* **31**, 2015–2017 (2006).
187. Zhang, Y. *et al.* Engineered tumor cell apoptosis monitoring method based on dynamic laser tweezers. *Biomed Res. Int.* **2014**, (2014).
188. Wang, D. C., Wun, S. J., Chen, K. Y., Chen, G. Y. & Chen, S. H. Apoptosis study of the macrophage via near-field scanning optical microscope. *J. Phys. Conf. Ser.* **100**, 24–27 (2008).
189. Yu, F. *et al.* let-7 Regulates Self Renewal and Tumorigenicity of Breast Cancer Cells. *Cell* **131**, 1109–1123 (2007).
190. Wiggan, O., Shaw, A. E., DeLuca, J. G. & Bamburg, J. R. ADF/Cofilin Regulates Actomyosin Assembly through Competitive Inhibition of Myosin II Binding to F-Actin. *Dev. Cell* **22**, 530–543 (2012).
191. Wiggan, O., Schroder, B., Krapf, D., Bamburg, J. R. & DeLuca, J. G. Cofilin Regulates Nuclear Architecture through a Myosin-II Dependent Mechanotransduction Module. *Sci. Rep.* **7**, 40953 (2017).
192. Yadav, V. K., Batham, S., Acharya, A. K. & Paul, R. Approach to accurate circle detection: Circular Hough Transform and Local Maxima concept. *2014 Int. Conf. Electron. Commun. Syst. ICECS 2014* 3–7 (2014).  
doi:10.1109/ECS.2014.6892577
193. van Loenhout, M. T. J., Kerssemakers, J. W. J., De Vlaminck, I. & Dekker, C. Non-Bias-Limited Tracking of Spherical Particles, Enabling Nanometer Resolution at Low Magnification. *Biophys. J.* **102**, 2362–2371 (2012).
194. Schafer, K. A. The Cell Cycle: A Review. *Vet. Pathol.* **35**, 461–478 (1998).

195. Raucher, D. *et al.* Phosphatidylinositol 4,5-Bisphosphate Functions as a Second Messenger that Regulates Cytoskeleton–Plasma Membrane Adhesion. *Cell* **100**, 221–228 (2000).
196. Janmey, P. A. & McCulloch, C. A. Cell Mechanics: Integrating Cell Responses to Mechanical Stimuli. *Annu. Rev. Biomed. Eng.* **9**, 1–34 (2007).
197. Geudens, I. & Gerhardt, H. Coordinating cell behaviour during blood vessel formation. *Development* **138**, 4569–4583 (2011).
198. Risau, W. *et al.* Vasculogenesis and angiogenesis in embryonic-stem-cell-derived embryoid bodies. *Development* **102**, 471–8 (1988).
199. Davies, P. F., Remuzzi, A., Gordon, E. J., Dewey, C. F. & Gimbrone, M. A. Turbulent fluid shear stress induces vascular endothelial cell turnover in vitro. *Proc. Natl. Acad. Sci. U. S. A.* **83**, 2114–7 (1986).
200. Katritsis, D. *et al.* Wall Shear Stress: Theoretical Considerations and Methods of Measurement. *Prog. Cardiovasc. Dis.* **49**, 307–329 (2007).
201. River, G. Zebrafish : A model for heart development. *Microsc. Imaging Stn.* 1–3 (2008). at  
<[http://www.exploratorium.edu/imaging\\_station/research/zebrafish/story\\_zebrafish1.php](http://www.exploratorium.edu/imaging_station/research/zebrafish/story_zebrafish1.php)>
202. Ungos, J. & Weinstein, B. M. Vascular Development in the Zebrafish. 301–332 (2007). doi:10.1016/S1574-3349(07)18012-1
203. Goishi, K. & Klagsbrun, M. in *Current Topics in Developmental Biology* **62**, 127–152 (2004).

204. Craig, M. P., Gilday, S. D., Dabiri, D. & Hove, J. R. An Optimized Method for Delivering Flow Tracer Particles to Intravital Fluid Environments in the Developing Zebrafish. *Zebrafish* **9**, 108–119 (2012).
205. Zeng, Y. *et al.* In vivo micro-vascular imaging and flow cytometry in zebrafish using two-photon excited endogenous fluorescence. *Biomed. Opt. Express* **5**, 653 (2014).
206. Jamison, R. A., Samarage, C. R., Bryson-Richardson, R. J. & Fouras, A. In Vivo Wall Shear Measurements within the Developing Zebrafish Heart. *PLoS One* **8**, e75722 (2013).
207. Brown, D., Samsa, L., Qian, L. & Liu, J. Advances in the Study of Heart Development and Disease Using Zebrafish. *J. Cardiovasc. Dev. Dis.* **3**, 13 (2016).
208. Bennett, C. *et al.* Myelopoiesis in the zebrafish, *Danio rerio*. *Blood* **98**, 643–651 (2001).
209. Asnani, A. & Peterson, R. T. The zebrafish as a tool to identify novel therapies for human cardiovascular disease. *Dis. Model. Mech.* **7**, 763–767 (2014).
210. Ellertsdóttir, E. *et al.* Vascular morphogenesis in the zebrafish embryo. *Dev. Biol.* **341**, 56–65 (2010).
211. Wang, X. *et al.* Enhanced cell sorting and manipulation with combined optical tweezer and microfluidic chip technologies. *Lab Chip* **11**, 3656 (2011).
212. Mushfique, H. *et al.* 3D Mapping of Microfluidic Flow in Laboratory-on-a-Chip Structures Using Optical Tweezers. *Anal. Chem.* **80**, 4237–4240 (2008).

213. Lincoln, B. *et al.* Deformability-based flow cytometry. *Cytometry* **59A**, 203–209 (2004).
214. Ayano, S., Wakamoto, Y., Yamashita, S. & Yasuda, K. Quantitative measurement of damage caused by 1064-nm wavelength optical trapping of *Escherichia coli* cells using on-chip single cell cultivation system. *Biochem. Biophys. Res. Commun.* **350**, 678–684 (2006).
215. Hansen, P. M. & Oddershede, L. B. Optical trapping inside living organisms. in *Proceedings of SPIE* (eds. Dholakia, K. & Spalding, G. C.) 593003 (2005). doi:10.1117/12.616879
216. Zhong, M.-C., Wei, X.-B., Zhou, J.-H., Wang, Z.-Q. & Li, Y.-M. Trapping red blood cells in living animals using optical tweezers. *Nat. Commun.* **4**, 1768 (2013).
217. Schroder, B. W., Johnson, B. M., Garrity, D. M., Dasi, L. P. & Krapf, D. Force Spectroscopy in the Bloodstream of Live Embryonic Zebrafish with Optical Tweezers. in *Frontiers in Optics 2014 FTu1F.5* (OSA, 2014). doi:10.1364/FIO.2014.FTu1F.5
218. Westerfield, M. *The Zebrafish Book. A Guide for The Laboratory Use of Zebrafish (Danio rerio)*. *Eugene* **385**, (2000).
219. Sabeh, M. K., Kekhia, H. & MacRae, C. A. Optical Mapping in the Developing Zebrafish Heart. *Pediatr. Cardiol.* **33**, 916–922 (2012).
220. Johnson, B., M. Garrity, D. & Dasi, L. *The Transitional Cardiac Pumping Mechanics in the Embryonic Heart. Cardiovascular Engineering and*

- Technology* 4, (2013).
221. Guizar-Sicairos, M., Thurman, S. T. & Fienup, J. R. Efficient subpixel image registration algorithms. *Opt. Lett.* **33**, 156 (2008).
  222. Graham, M. S., Fletcher, G. L. & Haedrich, R. L. Blood viscosity in arctic fishes. *J. Exp. Zool.* **234**, 157–160 (1985).
  223. N.W., P. & R, W. Effects of Stress on Plasma Cortisol Levels and Blood Viscosity in Blue Mao Mao, *Scorpius Violaceus* (Hutton), a Marine Teleost. *Comp. Biochem. Physiol. Part A Mol. Integr. Physiol.* **101A**, 335–339 (1992).
  224. Wells, R. M. G. & Baldwin, J. Oxygen transport potential in tropical reef fish with special reference to blood viscosity and haematocrit. *J. Exp. Mar. Bio. Ecol.* **141**, 131–143 (1990).
  225. Wells, R. M. G. & Forster, M. E. Dependence of blood viscosity on haematocrit and shear rate in a primitive vertebrate. *J. Exp. Biol.* **145**, 483–487 (1989).
  226. Castellini, M. A., Baskurt, O., Castellini, J. M. & Meiselman, H. J. Blood rheology in marine mammals. *Front. Physiol.* **1 DEC**, (2010).
  227. Graham, M. S. & Fletcher, G. L. On the low viscosity blood of two cold water, marine sculpins. *J. Comp. Physiol. B* **155**, 455–459 (1985).
  228. Berns, M. W. *et al.* Use of a laser-induced optical force trap to study chromosome movement on the mitotic spindle. *Proc. Natl. Acad. Sci.* **86**, 4539–4543 (1989).
  229. Sparkes, I. A., Ketelaar, T., De Ruijter, N. C. A. & Hawes, C. Grab a golgi: Laser trapping of golgi bodies reveals in vivo interactions with the

- endoplasmic reticulum. *Traffic* **10**, 567–571 (2009).
230. Ashkin, A. & Dziedzic, J. M. Internal cell manipulation using infrared laser traps. *Proc. Natl. Acad. Sci.* **86**, 7914–8 (1989).
231. Chan, P. K., Lin, C. C. & Cheng, S. H. Noninvasive technique for measurement of heartbeat regularity in zebrafish (*Danio rerio*) embryos. *BMC Biotechnol.* **9**, 1–10 (2009).
232. Ibrahim, M., Balakrishnan, A., Seppan, P. & Lee, H.-J. Effect of Ethanol Exposure on Heart Development in Zebra Fish (*Danio rerio*) Embryos. *Int. J. Anat. Sci.* **5**, 26–33 (2014).
233. Hurley, J. H. Membrane binding domains. *Biochim. Biophys. Acta - Mol. Cell Biol. Lipids* **1761**, 805–811 (2006).
234. Lemmon, M. A. Membrane recognition by phospholipid-binding domains. *Nat. Rev. Mol. Cell Biol.* **9**, 99–111 (2008).
235. LEMMON, M. A. & FERGUSON, K. M. Signal-dependent membrane targeting by pleckstrin homology (PH) domains. *Biochem. J.* **350**, 1–18 (2000).
236. Cho, W. & Stahelin, R. V. Membrane binding and subcellular targeting of C2 domains. *Biochim. Biophys. Acta - Mol. Cell Biol. Lipids* **1761**, 838–849 (2006).
237. Letunic, I., Doerks, T. & Bork, P. SMART 7: Recent updates to the protein domain annotation resource. *Nucleic Acids Res.* **40**, 302–305 (2012).
238. Knight, J. D. & Falke, J. J. Single-Molecule Fluorescence Studies of a PH Domain: New Insights into the Membrane Docking Reaction. *Biophys. J.* **96**,

- 566–582 (2009).
239. Yasui, M., Matsuoka, S. & Ueda, M. PTEN Hopping on the Cell Membrane Is Regulated via a Positively-Charged C2 Domain. *PLoS Comput. Biol.* **10**, (2014).
240. Barkai, E., Garini, Y. & Metzler, R. Strange kinetics of single molecules in living cells. *Phys. Today* **65**, 29–35 (2012).
241. Höfling, F. & Franosch, T. Anomalous transport in the crowded world of biological cells. *Reports Prog. Phys.* **76**, (2013).
242. Metzler, R., Jeon, J. H., Cherstvy, A. G. & Barkai, E. Anomalous diffusion models and their properties: Non-stationarity, non-ergodicity, and ageing at the centenary of single particle tracking. *Phys. Chem. Chem. Phys.* **16**, 24128–24164 (2014).
243. Krapf, D. Mechanisms Underlying Anomalous Diffusion in the Plasma Membrane. *Current Topics in Membranes* **75**, 167–207 (2015).
244. Golding, I. & Cox, E. C. Physical nature of bacterial cytoplasm. *Phys. Rev. Lett.* **96**, 14–17 (2006).
245. Tolić-Nørrelykke, I. M., Munteanu, E. L., Thon, G., Oddershede, L. & Berg-Sørensen, K. Anomalous diffusion in living yeast cells. *Phys. Rev. Lett.* **93**, 1–4 (2004).
246. Jeon, J. H. *et al.* In vivo anomalous diffusion and weak ergodicity breaking of lipid granules. *Phys. Rev. Lett.* **106**, 2–5 (2011).
247. Bronstein, I. *et al.* Transient anomalous diffusion of telomeres in the nucleus

- of mammalian cells. *Phys. Rev. Lett.* **103**, 1–4 (2009).
248. Weigel, A. V., Tamkun, M. M. & Krapf, D. Quantifying the dynamic interactions between a clathrin-coated pit and cargo molecules. *Proc. Natl. Acad. Sci.* **110**, E4591–E4600 (2013).
249. Heinemann, F., Vogel, S. K. & Schwille, P. Lateral membrane diffusion modulated by a minimal actin cortex. *Biophys. J.* **104**, 1465–1475 (2013).
250. Torreno-Pina, J. A. *et al.* Enhanced receptor-clathrin interactions induced by N-glycan-mediated membrane micropatterning. *Proc. Natl. Acad. Sci.* **111**, 11037–11042 (2014).
251. Banks, D. S. & Fradin, C. Anomalous diffusion of proteins due to molecular crowding. *Biophys. J.* **89**, 2960–2971 (2005).
252. Szymanski, J. & Weiss, M. Elucidating the origin of anomalous diffusion in crowded fluids. *Phys. Rev. Lett.* **103**, 1–4 (2009).
253. Horton, M. R., Höfling, F., Rädler, J. O. & Franosch, T. Development of anomalous diffusion among crowding proteins. *Soft Matter* **6**, 2648–2656 (2010).
254. Jeon, J. H., Monne, H. M. S., Javanainen, M. & Metzler, R. Anomalous diffusion of phospholipids and cholesterol in a lipid bilayer and its origins. *Phys. Rev. Lett.* **109**, 1–5 (2012).
255. Bursac, P. *et al.* Cytoskeleton dynamics: Fluctuations within the network. *Biochem. Biophys. Res. Commun.* **355**, 324–330 (2007).
256. Kahana, A., Kenan, G., Feingold, M., Elbaum, M. & Granek, R. Active

- transport on disordered microtubule networks: The generalized random velocity model. *Phys. Rev. E - Stat. Nonlinear, Soft Matter Phys.* **78**, 1–15 (2008).
257. Bruno, L., Levi, V., Brunstein, M. & Despósito, M. A. Transition to superdiffusive behavior in intracellular actin-based transport mediated by molecular motors. *Phys. Rev. E - Stat. Nonlinear, Soft Matter Phys.* **80**, 1–7 (2009).
258. Akimoto, T. Distributional response to biases in deterministic superdiffusion. *Phys. Rev. Lett.* **108**, 1–5 (2012).
259. Skaug, M. J., Mabry, J. & Schwartz, D. K. Intermittent molecular hopping at the solid-liquid interface. *Phys. Rev. Lett.* **110**, 1–5 (2013).
260. Yu, C., Guan, J., Chen, K., Bae, S. C. & Granick, S. Single-molecule observation of long jumps in polymer adsorption. *ACS Nano* **7**, 9735–9742 (2013).
261. Bouchaud, J. P. Weak ergodicity breaking and aging in disordered systems. *J. Phys. I* **2**, 1705–1713 (1992).
262. Bel, G. & Barkai, E. Weak ergodicity breaking in the continuous-time random walk. *Phys. Rev. Lett.* **94**, 7–10 (2005).
263. Krapf, D. Nonergodicity in nanoscale electrodes. *Phys. Chem. Chem. Phys.* **15**, 459–465 (2013).
264. Weigel, A. V., Simon, B., Tamkun, M. M. & Krapf, D. Ergodic and nonergodic processes coexist in the plasma membrane as observed by single-molecule

- tracking. *Proc. Natl. Acad. Sci.* **108**, 6438–6443 (2011).
265. Manzo, C. *et al.* Weak ergodicity breaking of receptor motion in living cells stemming from random diffusivity. *Phys. Rev. X* **5**, 1–12 (2015).
266. Tabei, S. M. A. *et al.* Intracellular transport of insulin granules is a subordinated random walk. *Proc. Natl. Acad. Sci.* **110**, 4911–4916 (2013).
267. Brokmann, X. *et al.* Statistical Aging and Nonergodicity in the Fluorescence of Single Nanocrystals. *Phys. Rev. Lett.* **90**, 4 (2003).
268. Stefani, F. D., Hoogenboom, J. P. & Barkai, E. Beyond quantum jumps: Blinking nanoscale light emitters. *Phys. Today* **62**, 34–39 (2009).
269. Yin, J., Lin, A. J., Golan, D. E. & Walsh, C. T. Site-specific protein labeling by Sfp phosphopantetheinyl transferase. *Nat. Protoc.* **1**, 280–285 (2006).
270. Jaqaman, K. *et al.* Robust single-particle tracking in live-cell time-lapse sequences. *Nat. Methods* **5**, 695–702 (2008).
271. Sugita, S., Shin, O. H., Han, W., Lao, Y. & Sudhof, T. C. Synaptotagmins form a hierarchy of exocytotic Ca(2+) sensors with distinct Ca(2+) affinities. *Embo J* **21**, 270–280 (2002).
272. Ziemba, B. P. & Falke, J. J. Lateral diffusion of peripheral membrane proteins on supported lipid bilayers is controlled by the additive frictional drags of (1) bound lipids and (2) protein domains penetrating into the bilayer hydrocarbon core. *Chem. Phys. Lipids* **172–173**, 67–77 (2013).
273. Bychuk, O. & O’Shaughnessy, B. Anomalous Diffusion at Liquid Surfaces. *Phys. Rev. Lett.* **74**, 1795–1798 (1995).

274. Sidney Redner. *A Guide to First-Passage Processes*. (2001).
275. Chechkin, A. V., Zaid, I. M., Lomholt, M. A., Sokolov, I. M. & Metzler, R. Bulk-mediated diffusion on a planar surface: Full solution. *Phys. Rev. E - Stat. Nonlinear, Soft Matter Phys.* **86**, 1–11 (2012).
276. Froemberg, D. & Barkai, E. Random time averaged diffusivities for Lévy walks. *Eur. Phys. J. B* **86**, 331 (2013).
277. Valiullin, R., Kimmich, R. & Fatkullin, N. Lévy walks of strong adsorbates on surfaces: Computer simulation and spin-lattice relaxation. *Phys. Rev. E - Stat. Physics, Plasmas, Fluids, Relat. Interdiscip. Top.* **56**, 4371–4375 (1997).
278. Margolin, G. & Barkai, E. Nonergodicity of a time series obeying lévy statistics. *J. Stat. Phys.* **122**, 137–167 (2006).
279. Tamm, L. K. Lateral Diffusion and Fluorescence Microscope Studies on a Monoclonal Antibody Specifically Bound to Supported Phospholipid Bilayers. *Biochemistry* **27**, 1450–1457 (1988).
280. Gambin, Y. *et al.* Lateral mobility of proteins in liquid membranes revisited. *Proc. Natl. Acad. Sci.* **103**, 2098–2102 (2006).
281. Ramadurai, S. *et al.* Influence of hydrophobic mismatch and amino acid composition on the lateral diffusion of transmembrane peptides. *Biophys. J.* **99**, 1447–1454 (2010).
282. Ziemba, B. P., Knight, J. D. & Falke, J. J. Assembly of membrane-bound protein complexes: Detection and analysis by single molecule diffusion. *Biochemistry* **51**, 1638–1647 (2012).

283. Lomholt, M. A. *et al.* Lévy strategies in intermittent search processes are advantageous. *Proc. Natl. Acad. Sci.* **105**, 11055–11059 (2008).
284. Palyulin, V. V., Chechkin, A. V. & Metzler, R. Levy flights do not always optimize random blind search for sparse targets. *Proc. Natl. Acad. Sci.* **111**, 2931–2936 (2014).
285. Ritchie, K., Iino, R., Fujiwara, T., Murase, K. & Kusumi, A. The fence and picket structure of the plasma membrane of live cells as revealed by single molecule techniques (Review). *Mol. Membr. Biol.* **20**, 13–18 (2003).
286. Andrews, N. L. *et al.* Actin restricts FcεRI diffusion and facilitates antigen-induced receptor immobilization. *Nat. Cell Biol.* **10**, 955–963 (2008).
287. Campagnola, G., Nepal, K., Schroder, B. W., Peersen, O. B. & Krapf, D. Superdiffusive motion of membrane-targeting C2 domains. *Sci. Rep.* **5**, 17721 (2016).

## APPENDICES

---

### APPENDICES A-1.      PROTOCOLS

---

List of Protocols:

- A-1.1 Polystyrene Bead Cleaning Protocol
- A-1.2 Cell Freeze Down Procedure
- A-1.3 Cell Planting/Passage Procedure
- A-1.4 Chamber Preparation for Lipid Bilayers
- A-1.5 Coverslip Cleaning/Preparation of Glass/Siliconized Surfaces
- A-1.6 Surface Preparation for HeLa Cell Culture
- A-1.7 Laser Alignment Protocol
- A-1.8 Tracking Algorithm & Image Enhancement Protocol
- A-1.9 Zebrafish Preparation Protocol

### General Notes

**-This protocol is aimed at generic cleaning of polystyrene beads. There are multiple ways to accomplish cleaning of the beads. A good overview can be found in the TechNote 203: Washing Microspheres protocol provided by Bang Laboratories**

**(<https://www.bangslabs.com/sites/default/files/imce/docs/TechNote%20203%20Web.pdf>).**

**-The buffers used in this protocol to wash and store the beads can be varied per the surface of the beads you are working with. Coated beads may need extra stabilization not found necessary with plain polystyrene beads. Refer to the manufacturer's suggestion for appropriate buffers.**

### Generic Bead Cleaning by Centrifugation

- 1. Turn on the oven to 80°C. (Check the thermometer before actually placing the acid solution in the oven.)
- 2. During the temperature rise time, get out the appropriate number of microcentrifuge tubes that you want to prepare for the bead cleaning procedure. Rinse briefly with isopropyl alcohol (IPA).
- 3. Once the oven is at temp, add an appropriate volume of acetone to the tubes being used. (0.6 ml = 500 µl, 1.5 ml = 1.3 ml, etc.)
- 4. Let the acetone sit for 30-60 seconds to clean the surface and quickly etch them.
- 5. Remove the acetone from the tubes and place in the oven to dry. This process helps to prevent the beads from adhering to the surface during cleaning.
- 6. Once the tubes are dried, place the appropriate volume of beads within the tube that you would like to wash. Typically, 1.0 ml will suffice for a 1.5 ml tube, but less can be used if you intend to dilute the bead solution as part of the process.
- 7. Place the microcentrifuge tube in the desktop centrifuge with a balance across from it and centrifuge at the rate per the following table taken from the Bang Laboratories TechNote referenced above:

**Table 1:** Sample protocols for benchtop (7.3 cm rotation radius) centrifuge, all – 5 min.

<b>Bead Type</b>	<b>Diameter Range</b>	<b>Relative Centrifugal Force Range (xG)</b>	<b>Speed Range (rpm)</b>
polymer	> 0.5µm	6500 - 14000	8925 - 13100
	> 1.0µm	3000 - 5500	6060 - 8210
	> 5µm	1300 - 3000	3990 - 6060
silica	> 0.5µm	3000 - 5500	6060 - 8210
	> 1.0µm	1300 - 3000	3990 - 6060
	> 5.0µm	750 - 1300	3030 - 3990
protein/Ab-coated	> 0.5µm	8000 - 11000	9900 - 11610
	> 1.0µm	5500 - 8000	8210 - 9900
	> 5.0µm	2000 - 5500	4950 - 8210

- 8. Remove from centrifuge and carefully aspirate remaining liquid with either a micropipette or vacuum aspiration.
- 9. Add 1.0 ml of buffer (typically 1X PBS) to the tube and repeat centrifugation.
- 10. Repeat step 8 and 9 for 2-3X total.
- 11. Add 1.0 ml of storage buffer (typically 20mM Tris- HCL pH=7.5 can add 2mM EDTA, 50 mM NaCl, 1% w/v BSA, or 0.05% Tween 20 to help prevent bead aggregation).
- 12. Store beads per manufacturer’s suggested temperatures until use.

### General Notes

- The hood should always be maintained as contaminant-free as possible so:
  - Spray and/or wipe gloves and materials before going under the hood.
  - Try not to reach over materials, especially ones that are open or exposed.
- When using disposable pipettes from wrappers: try and peel the wrapper halfway down and keep it to one side to dispose of the pipette in it later to help against contamination.
- You can always turn pipettes when placing them in the dispenser so you can easily see the numbers.

### Preparation:

*Note: Before performing a pass, dishes should be checked under microscope for proper confluency as per table 2 below.*

- 1. The following materials should be placed in the water bath and calibrated to 37°C:
  - Freeze-Down Media (40% DMEM, 50% FBS, 10% DMSO), DMEM + 10%FBS, 1X Trypsin-EDTA, & 1X PBS
- 2. While above materials equilibrate, gather all necessary supplies (i.e. culture dishes, pipettes, conicals), spray/wipe with alcohol (70% IPA), place in hood, and UV for at least 3-5 min.

### Freeze Procedure:

- 3. Remove confluent dishes from incubator, and place in hood.
- 4. Wipe trypsin & PBS containers with IPA, and place in hood.
- 5. Aspirate remaining media from dish(es) (Keep glass pipette clean for use on step 7).
- 6. Rinse w/ PBS (Pour enough in dish to completely cover the bottom).
- 7. Aspirate PBS from dish(es).
- 8. Pipette 4.0 ml of trypsin into dish.
- 9. Transfer dish(es) to incubator (Skip this step if working w/ 10T1/2 Cells).
- 10. While cells are trypsinizing, remove freeze-down media and regular media from water bath and wipe with IPA.
- 11. Pipette 10 mls of fresh media (DMEM + 10% FBS) into the number of 15 ml conicals equaling the number of dishes you trypsinized.
- 12. Remove cells from incubator (Not necessary for 10T1/2).
- 13. Gently swirl dishes and pipette up cell suspension from dish(es).
- 14. Transfer cell suspension to 15 ml conicals and pipette up and down 10-25 times to re-suspend cells.
- 15. Centrifuge 15 ml conicals at 1000 RPMs for 5 min.

- ❑ 16. Remove conicals from centrifuge and aspirate the remaining media above the cellular pellet.
- ❑ 17. Add 2 mls of freeze down media to each conical and resuspend cellular pellet.
- ❑ 18. Label the conicals with the appropriate cellular information (Cell Line, Date, Passage #, etc.).
- ❑ 19. Place all conicals in the -80°C freezer for storage. (Cells can be removed to liquid nitrogen for longer storage with the use of different vials after 24 hours at -80°C.)
- ❑ 20. Aspirate any remaining fluids, discard any waste products (glass must be put in proper container), wipe hood with IPA, and UV sterilize for next person's use.

### General Notes

- The hood should always be maintained as contaminant-free as possible so:
  - Spray and/or wipe gloves and materials before going under the hood.
  - Try not to reach over materials, especially ones that are open or exposed.
- When using disposable pipettes from wrappers: try and peel the wrapper halfway down and keep it to one side to dispose of the pipette in it later to help against contamination.
- You can always turn pipettes when placing them in the dispenser so you can easily see the numbers.

### Preparation:

*Note: Before performing a pass, dishes should be checked under microscope for proper confluency as per table below.*

- 1. The following materials should be placed in the water bath and calibrated to 37°C:
  - a. Plant: DMEM + 10% FBS.
  - b. Pass: DMEM + 10%FBS, 1X Trypsin-EDTA, & 1X PBS.
- 2. While above materials equilibrate, gather all necessary supplies (i.e. culture dishes, pipettes, conicals), spray/wipe with alcohol (70% IPA), place in hood, and UV for at least 3-5 min.

### Plant Procedure:

- 3. Remove cells from -70°C freezer, wipe away frost.
- 4. Thaw in water bath at 37°C.
- 5. After thawed, wipe down vial & media bottle with IPA, then place in hood.
- 6. Pipette 5 ml fresh media into the vial.
- 7. Remove from hood and place in centrifuge (counterbalance with proper volume of water).
- 8. Spin @ 1000 RPMs for 5 min.
- 9. While cells are spinning, add fresh media to dishes & conical (volumes in table 1 below).
- 10. Remove cells from centrifuge, wipe with IPA, and place in hood.

### Pass Procedure:

- 3. Remove confluent dishes from incubator, and place in hood.
- 4. Wipe trypsin & PBS containers with IPA, and place in hood.
- 5. Aspirate remaining media from dish(es) (Keep glass pipette clean for use on step 7).
- 6. Rinse w/ PBS (Pour enough in dish to completely cover the bottom).
- 7. Aspirate PBS from dish(es).
- 8. Pipette proper volume of trypsin into dish based on table 2 below.
- 9. Transfer dish(es) to incubator (Skip this step if working w/ 10T1/2 Cells).

- 11. Aspirate supernatant (fluid above cell pellet) from the vial.
- 12. Pipette 5 ml fresh media into vial dislodging pellet, and then pipette back up.
- 10. While cells are trypsinizing, add fresh media to dishes & conical (volumes in table 1 below).
- 11. Remove cells from incubator (Not necessary for 10T1/2).
- 12. Gently swirl dishes and pipette up cell suspension from dish(es).
- 13. Transfer cell suspension to 50 ml conical and pipette up and down 10-25 times to re-suspend cells.
- 14. Pipette proper volumes into already prepared dishes based on table 2 below.
- 15. Place dishes in incubator at 37°C + 5% CO<sub>2</sub>.
- 16. Aspirate any remaining fluids, discard any waste products (glass must be put in proper container), wipe hood with IPA, and UV sterilize for next person's use.

### General Notes

**-Lipids should be prepared ahead of time, which is typically done by Grace Campagnola. (Please refer to her for lipid preparation protocols.)**

**-It is very important to work quickly and cleanly to ensure integrity of glass surface.**

#### Coverslip Preparation/Cleaning

- 1. Place coverslips to be cleaned in the Teflon holder making sure each coverslip has a separate slot.
- 2. Remove a clean 500ml beaker from the cabinet and place the Teflon slide holder and coverslips inside.
- 3. Add distilled (RO) water to the point it is covering the coverslips fully and add detergent to beaker.
- 4. Place beaker in sonicator in the fume hood and sonicate for 30 minutes. (make sure distilled water level is at operating level)
- 5. Rinse multiple times with miliQ water to displace the detergent from the solution and coverslips.
- 6. Remove holder to a beaker containing isopropyl alcohol (aka IPA or 2-Propanol) to remove any remaining detergent from the coverslips.
- 7. Remove holder to a fresh beaker of milliQ water for a quick rinse.
- 8. Using forceps/tweezers, remove coverslips one by one and blow dry with nitrogen gas.
- 9. Place dried slips in a sterile petri dish for longer term storage or use.

#### Chamber Attachment

(Note: Perfusion chambers are purchased from Grace Bio-Labs. Product is SA8R-2.0 SecureSeal™ Hybridization Chambers)

- 1. Remove coverslips to be used from sterile dish and place on a clean plastic surface for use with oxygen plasma etcher.
- 2. Place the plastic holder with coverslips in the oxygen plasma etch machine.
- 3. Turn on the oxygen at the bottle at the back of the hood by opening the valve on top of the gas cylinder.
- 4. Turn on the machine with the switch at the bottom right corner at the back of the machine.
- 5. When the machine comes on, press the enter button. The device will say “Commands Menu” on the screen. Press the right arrow button once and it should say “Setup Menu” on the screen.
- 6. Press the enter button to enter the setup menu.
- 7. The plasma time will be displayed and should be changed from 2 min to 10 min.

- ❑ 8. Once the change is made, press enter button followed by the up arrow button to exit the setup menu.
- ❑ 9. The screen should read “Setup Menu”. Press the right arrow button to get back to the “Commands Menu”.
- ❑ 10. Press the enter button to go into the commands menu. The screen should read “Commands PLASMA”.
- ❑ 11. Press enter to start the plasma cycle. The chamber will begin pumping down to 200 mTorr before creating the plasma.
- ❑ 12. Make sure that the gas 1 golumn in the top right corner reads 2.5 while it is pumping down.
- ❑ 13. Once the chamber has reached 200 mTorr, the plasma will start.
- ❑ 14. While the plasma is running, prepare the perfusion chambers that should have already been cut appart. Remove the backing for each of the chambers, so they may be placed on immediately after plasma oxygenation.
- ❑ 15. Once the 10 min. cycle has ended, the chamber will depressurize. Press the up arrow button to get back to the “Commands Menu” screen.
- ❑ 16. Press the enter button to enter the menu followed by pressing the right arrow button once to see “Commands CYCLE STOP”. Press the enter button again.
- ❑ 17. The chamber will ready itself to be opened, and once ready, quickly remove the slides with gloved hands.
- ❑ 18. Place the perfusion chambers on the coverslips as quickly as possible using tweezers/forceps to do so.
- ❑ 19. Allow the chambers and coverslips to sit for 30 min. for the glass surface to return to a less hydrophilic state.
- ❑ 20. During the 30 minute window, remove the lipids from the -80°C freezer and sonicate on ice in 30 second intervals until the lipids appear clear. (This creates the small unilamellar vesicles from larger vesicles that have merged over time.)
- ❑ 21. Once the chambers have sat for that length of time, the lipids can be introduced into the chamber via a pipette. Pipette the lipid solution into the chambers carefully to not introduce air bubbles if possible. Add a droplet of lipid suspension to both holes to ensure the chamber does not dry out during incubation.
- ❑ 22. Incubate chambers with lipid suspension for 1 hour at room temperature. During this time, the lipid bilayer should form on the surface.
- ❑ 23. During this incubation period, it is important to prepare the protein/enzyme solutions to be used in the experiment. Remove the protein solutions from the -80°C freezer and dilute to a 75 pM concentration with imaging buffer (0.2 micron filtered 50 mM Hepes + 75 mM NaCl + 1 mM MgCl<sub>2</sub> + 2 mM TCEP + 200 μM CaCl<sub>2</sub>). (Do this closer to the end of the incubation period to minimize time proteins are at room temperature before experiments.)
- ❑ 24. After 1 hour incubation period, pipette multiple volumes of imaging buffer through the perfusion chambers to rinse the surface and prepare for the experiment.

- 25. Remove the chambers to the TIRF microscope setup that should have been aligned and made ready the previous day or earlier in the day of experimentation.
- 26. Turn on the camera and prepare for experiments.
- 27. Introduce protein solution to the lipid chamber slowly.
- 28. Begin imaging experiment.

## APPENDIX A-1.5 PREPARATION OF COVERSIP SURFACES

---

### GDA & SDA Slide Preparation

**(Note: GDA = Glass Detergent cleaned Air dried; SDA= Siliconized Detergent cleaned Air Dried; GAA= Glass Acid etched Air dried. Air used is compressed nitrogen. GAA slides are also subject to the detergent cleaning prior to acid etching. These processes are used to create a gradation in hydrophilicity for cellular growth on the varying surfaces and the effects upon their shape.)**

- 1. Place coverslips to be cleaned in the Teflon holder making sure each coverslip has a separate slot.
- 2. Remove a clean 500ml beaker from the cabinet and place the Teflon slide holder and coverslips inside.
- 3. Add distilled (RO) water to the point it is covering the coverslips fully and add detergent to beaker.
- 4. Place beaker in sonicator in the fume hood and sonicate for 30 minutes. ( make sure distilled water level is at operating level)
- 5. Rinse multiple times with miliQ water to displace the detergent from the solution and coverslips.
- 6. Remove holder to a beaker containing isopropyl alcohol (aka IPA or 2-Propanol) to remove any remaining detergent from the coverslips.
- 7. Remove holder to a fresh beaker of milliQ water for storage.
- 8. For use: remove coverslips with tweezers from the storage container and blow dry with nitrogen gas making sure to displace all of the water from the coverslips. Place the slips in a sterile petri dish for use.

Note: The GDA slides can be further processed into GAA slides as per the protocol below.

### GAA Slide Preparation

- 1. Turn on the oven to 50-60°C. (Check the thermometer before actually placing the acid solution in the oven.)
- 2. Follow protocol above to clean slides and prepare them for acid etching.
- 3. Upon completion of GDA/SDA protocol, remove the holder to a beaker containing 400ml of 1M hydrochloric acid (HCl).
- 4. Cover beaker with a clean watchglass to ensure minimal evaporation of the solution.
- 5. Place the beaker in the oven for 6-18 hours to etch the surfaces.
- 6. Upon completion of etching, remove beaker from oven with a hot pad or glove and allow to cool to room temp.
- 7. Once cool, remove holder to a fresh beaker containing milliQ water for a quick rinse and removal of acid.
- 8. Remove holder to beaker with IPA for a quick rinse.

- 9. Remove holder to a fresh beaker of milliQ water for the last rinse.
- 10. Using forceps/tweezers, remove coverslips one by one and blow dry with nitrogen gas.
- 11. Place dried slips in a sterile petri dish for longer term storage or use.

## APPENDIX A-1.6 SURFACE PREPARATION FOR HELa CELL CULTURE

---

### Hydrophilic Glass Slide Preparation

- 1. Turn on the oven to 50-60°C. (Check the thermometer before actually placing the acid solution in the oven.)
- 2. Place coverslips to be cleaned in the Teflon holder making sure each coverslip has a separate slot.
- 3. Remove a clean 500ml beaker from the cabinet and place the Teflon slide holder and coverslips inside.
- 4. Add distilled (RO) water to the point it is covering the coverslips fully and add detergent to beaker.
- 5. Place beaker in sonicator in the fume hood and sonicate for 30 minutes. (make sure distilled water level is at operating level)
- 6. Rinse multiple times with milliQ water to displace the detergent from the solution and coverslips.
- 7. Remove holder to a beaker containing isopropyl alcohol (aka IPA or 2-Propanol) to remove any remaining detergent from the coverslips.
- 8. Remove holder to a fresh beaker of milliQ water for a quick rinse.
- 9. Remove the holder to a beaker containing 400ml of 1M hydrochloric acid (HCl).
- 10. Cover beaker with a clean watchglass to ensure minimal evaporation of the solution.
- 11. Place the beaker in the oven for 6-18 hours to etch the surfaces.
- 12. Upon completion of etching, remove beaker from oven with a hot pad or glove and allow to cool to room temp.
- 13. Once cool, remove holder to a fresh beaker containing milliQ water for a quick rinse and removal of acid.
- 14. Remove holder to beaker with IPA for a quick rinse.
- 15. Remove holder to a fresh beaker of milliQ water for the last rinse.
- 16. Using forceps/tweezers, remove coverslips one by one and blow dry with nitrogen gas.
- 17. Place dried slips in a sterile petri dish for longer term storage or use.

### Poly-L-Lysine Coating

(Note: A 0.1% w/v solution of Poly-L-Lysine should be prepared prior to this work and stored in 5 ml aliquots at -20°C for later use.)

- 1. Remove Poly-L-Lysine (PLL) aliquot from freezer and dilute 1:20 in water for the volume you need.
- 2. Remove dried slides from petri dish for coating procedure.
- 3. Place slides in a cell culture dish for the coating procedure.
- 4. Pipette PLL solution onto slides until they are completely covered with solution to all edges. (Note: Add a little extra after completely covered as the solution will evaporate a bit during the procedure.)

- 5. Carefully place the cell culture dish with the slides in the incubator at 37°C for 1 hour.
- 6. After incubation, remove the dish and aspirate the remaining liquid from the surface.
- 7. Allow the slide to dry completely in the hood.
- 8. Wrap the dishes with parafilm, mark the contents and date on the dish, and place in the refrigerator for long term storage. (Note: The slides may be stored in this manner for up to 3 months.)

### General Notes

- Laser alignment is key to good experimental outcomes whether it be with the tweezers or the TIRF setups.
- You will need a variety of colored sharpie style markers (fine point is better if possible), a combination square, a flat 24" blade/16" base square, and the beam star profile camera.
- It is good to draw out all laser paths and optics on a sheet of paper prior to laying out the lines on the table.
- This protocol should be shown to any new lab member prior to giving them the chance to implement it. The terminology and procedures need to be learned from someone who know them to really implement this protocol well.

### Laying out Laser Path

- 1. The laser path is determine by the start point, the telescope location, mirror locations, and dichroic locations. It is important to have these well determined prior to starting. You start at the output of the laser and draw a line from the laser position straight out to the first mirror or dichroic. This is done holding the flat square against the table with one edge running perpendicular to the table edge for the laser path.
- 2. At the location of the first mirror/dichroic, the combination square is use to draw the 45° line for the mirror. If the combination square isn't long enough, the flat square can be used as an extension against the combination square to draw the line.
- 3. The next line is added perpendicular to the original laser path reflecting off the diagonal line. The three lines should all intersect at the same point. This path is drawn until the next mirror/dichroic location.
- 4. Repeat step 2 at the second dichroic location.
- 5. Repeat step 3 reflecting perpendicular from original path at second location
- 6. Repeat steps 2 & 3 until the entire path is drawn out going into the back of the microscope.

### Laser Alignment

**(Note: This protocol assumes knowledge of how to use the beam star profiler camera. Maintenance of laser power at a low level is necessary not to damage the camera. Use ND filters as necessary to ensure laser power is minimized to a level where nothing will be damaged. ALWAYS WEAR SAFETY GLASSES APPROPRIATE FOR THE LASER YOU ARE USING... YOU CAN NEVER UNDO THE DAMAGE DONE BY A LASER TO YOUR EYES!!!!)**

- ❑ 1. Laser alignment is done at the height necessary to enter the microscope unless a periscope is to be used.
- ❑ 2. Place the laser at the appropriate height to enter the back of the microscope with the laser line following along the initial path drawn out. This is done by placing the flat edge of the combination square all the way to the edge so that it may stand on the table. The ruler edge of the combination square is then aligned with the marker edge on the table. The beam star camera is placed in line with the path and attached directly to the table. The combination square is placed on the line at the start of the path and the end of the path and the laser is aligned to the edge. Once the laser is shown as being halfway on the edge of the square at both the start and end locations of the path, that portion is aligned. Lock the laser in place, as necessary.
- ❑ 3. Place the first mirror with the edge aligning to the diagonal line drawn on the table. Move the camera to be in line with the next pathway needing alignment and affix it to the table.
- ❑ 4. Use the combination square in the same manner as described in Step 2 to align the next section of the path using the mirrors positioning knobs. Ensure the height is maintained based on the position in the camera screen as well as the path following the appropriate line. Once the camera displays half the laser profile at each the start and end position, it is aligned. Lock the mirror holder/dichroic in place. Make sure that the position of the beam does not move in the camera window while locking it down. If it does, adjust to where the position is maintain after locking down.
- ❑ 5. Repeat steps 3 and 4 for all remain angled pieces.
- ❑ 6. After all of the angled mirrors and dichroics have been placed, the beam expanding telescopes can be placed. (Note: This can be done in line also as long as the height and path of the beam is maintained throughout.)
- ❑ 7. The first lens is placed in path at the proper location and affixed to the table in a static position. This is done by placing the curved edge of the lens towards the laser. The reflection of the laser backward from the lens is then aligned until it directly reflects back upon itself into the laser and the path outward is maintained. I like to use an index card to cut the beam in half and reflect the other half of the beam back to lining up with the card edge.
- ❑ 8. The second lens is then added at the appropriate distance to collimate the beam. The beam size near the lens should be the exact same after the lens all the way until as far a distance as possible outward with no focal points in between, i.e. it should stay the same size the entire path. The lens is aligned curve edge outward as before with the back reflection reflecting back to the other lens.
- ❑ 9. Once this is done, the laser path should be established and aligned all the way until the back/side of the microscope.
- ❑ 10. The microscope is aligned using a tube attachment being placed where the objective goes on the microscope. The tube has two spiral irises placed on each end. The camera is place on the top of the tube to direct the path appropriately.

- 11. The laser beam is then walked into alignment using the last two mirrors in the optical path. This is done by aligning the path to the top and bottom irises until the laser passes through the center of both of them. This is similar to using the combination square to align the center to an edge, but in this case it is an opening. The beam has to be moved with the mirrors until this occurs. It is best to see this done before trying to do it yourself.

(Note: Stop here if you are aligning the tweezers system, as it is completely done.)

- 12. Once this has been done, a mark on the ceiling is made to mark the collimated position on a piece of paper. This will be used to align the last lens after the objective is put in place for the TIRF setup.
- 13. Place the objective in the TIRF setup.
- 14. Place a lens on the 3-axis positioner behind the microscope for moving the beams into TIRF.
- 15. Align the lens to where the back reflection occurs back on itself and the beam is centered on the mark on the ceiling for the original path.
- 16. Check to ensure the beam size coming out of the objective is the same all the way to the ceiling, or as close as possible. If it is not the same size, move the lens until it is collimated.

### General Notes

- This protocol is designed to work for both 2D and 3D tracking in line with the way the code was written to work in either manner.
- The image enhancement being performed happens as a simple upsampling algorithm that is innate to Labview. This upsampling algorithm is using bicubic spline interpolation on an image using the Image Resample VI. The user selects the level of resample as a factor of the resolution multiplier they want to use.
- A Hough circle transform has been included in the code as well that utilizes several blurs prior to a watershed of the image. This smooths the image and reduces the number of compartments found by the watershed while leaving the circular edges of a bead intact. The Hough transform draws circles around the watershed line points adding single intensity values to where the circle hits on the image. The highest number of intensity should correlate to the center of the circle, i.e. the bead center. This is used to find the bead center when the center of mass typically used fails.
- This protocol assumes a certain level of knowledge in Labview itself. If the user is not familiar with Labview, I highly suggest spending time to familiarize with simple Labview functions and wire colors correlating to data types first. It is extremely important to understand that the data types you are working with vary greatly, and this is reflected in the color, size, and shapes of the different wires being used. Ultimately, Labview is running C code at its most bare bones level, which is done through call library function nodes that require a lot more knowledge to manipulate. The reason data transfer understanding is so important is that the C code at the root of Labview will fail if the proper data types are not input into the functions/scripts. Thus, know what you are working with, look what you are trying to accomplish, and lay as much of it out on paper prior to trying to code it into Labview if you are a novice user. Utilize the help pages as much as possible, and don't be afraid to search for codes that someone else may have already written that does exactly what you want to do. Most likely, a code will exist if it is a general function that is used in multiple areas. You can use those generalized codes to create the complex codes you need to work with. This is just kind of general statement for Labview that will be helpful to your coding overall.
- Save your code regularly and often! It will save you a huge amount of headache redoing things when Labview hangs or crashes or anything along those lines!

## Implementing the Tracking Code:

- 1. The tracking code that is written and included as an image with this document has been designed as an all-in-one Subvi for use in any code that involves bead tracking. This code is named: 3D Tracking Subvi.vi. Although this code is designed to perform 3D tracking, it can perform standalone 2D tracking by conditionally turning off the 3D portion of the code.
- 2. This code needs several inputs wired to it to function properly, but has also been designed with default values for when certain areas are not connected. The major thing that needs to be wired for this code to work is the Image In. You need to pass an image coming from the code you are writing into this input for the code to work. This code is designed to detect the image type and function no matter what image is input into it. This code will function with no other inputs being wired.
  - Although the code functions without other inputs wired, it is important to know what the other inputs do:
    - Iterations: Wiring this input will allow the autocorrelation function to be run multiple times to find the bead center using the initial guess coordinates of the bead center from the previous iteration. I have found a single iteration to be adequate for almost all of my tracking experiments, which is the default value.
    - Resolution Multiplier: Wiring this input allows you to set the upsampling resolution for the Image Resample VI that is used as part of the autocorrelation function. The default value is 7. Lowering this value to 3 or higher will allow similar tracking enhancement at similar speeds. Increasing the value above 7 shows no benefit and leads to slower computation times.
    - Sub-ROI Width: This input sets the size of the window to be used after the Center of Mass or Hough Transform has found the center of the bead. Narrowing the window to a smaller size about the bead center enhances localization by the autocorrelation and decreases computation time. The default value is 76, which was found to be ideal with 1.7 micron beads and the Basler camera with a 37.5 nm pixel size. This will need to be adjusted with the use of another camera. I suggest using the ratio of pixels above to the pixel size of the camera above for a similar bead size. If the bead size is larger or smaller than this by a greater amount, then it is best to consider testing values to see what gives the best result.
    - ZLUT: This input is wired when you intend to track in 3D. A file containing a created Z-axis Look Up Table (ZLUT) must be opened and a 2D array from this file passed into this input. To track in Z, this must be wired. To track in 2D, this input is not necessary. The default value is an empty array.

- Track Z?: This is a binary true or false input. Wiring the value to be true will allow tracking in the third axis, Z-axis. The default value is false for simple 2D tracking.
  - Use Hough Circle Transform?: This is also a binary true or false input. Wiring the value to be true in this case will enable the Hough Transform Subvi to be used and will attempt to find circles of the radius you set with the Detection Radius Input. This will then replace a simple Center of Mass algorithm for finding the bead center. This is used when bead images are biased from the center of the bead by the presences of other structures such cells. The default value is false, which implements the Center of Mass algorithm.
  - Detection Radius: This is the radius of the circle you are trying to find with Hough Circle Detection algorithm. The default value is 7 currently, which is what was used to find a circle in an image I had created. The values were typically 18-22 when I was working with cells and the Basler camera with the smaller pixel size. You will have to determine what radius works best for you to find the center of the bead by this algorithm based on the beads you are using and the camera pixel size.
  - Circular Points: This is the number of points you want to draw in a circle around the points found in the watershed algorithm. The default value is 360 points for 360 degrees. This value can be decreased without issues, but should stay above 45 in my opinion. The less points you use to draw the circles around each point, the lower the probability of overlap and finding the center accurately.
    - The other inputs are simply designed to give you the options to modify my values that I found optimal for my experiments.
- 3. After wiring in the inputs you deem necessary for the tracking you wish to achieve, you must decide what outputs you also need. If you are simply doing a 2D tracking to find the XY position of bead center, the only output you need is the xy positions (pix) output. This gives you the xy positions in pixels with subpixel accuracy found from the autocorrelation algorithm. If you are tracking along the z-axis, you will also need to wire the output for the z positions (um). This is what gives you the z-axis localization from the ZLUT when the z-axis tracking is implemented. All the other outputs are for extra data.
- The extra outputs are described here in case you decide to use them:
    - Initial Coordinates: This outputs the initial guess coordinates from the COM or Hough algorithms that are used in the autocorrelation function. You can use these to determine if your initial guesses are fairly accurate and to compare the initial guess to the final values to determine if one of the algorithms might be failing. If the two values are extremely far off, you should determine which most highly correlates to the bead center and work to find why the other

- is being biased away from this value. If the autocorrelation is still finding the center accurately, this is less important to troubleshoot.
- Z profile: This outputs the radial z profile that is created when Z-axis tracking is implemented. The ZLUT is a stack of radial profiles correlating to a position in Z that has been defined by the piezoelectric stage. The radial profile is created based on the intensity values of the original bead image projected outward from the bead center coordinates. Thus, it finds the intensity average from each pixel location relative to the bead center location using the Pythagorean theorem. The Z profile reflects this averaged intensity value at each location outward from the center of the bead. You can look at this profile to determine if it accurately reflects what is seen in the bead intensity pattern if you like.
  - Frame rate: This is simply the inverse of the amount of time that it took to run the subvi code in its entirety. This allows you to see how fast the algorithm is running. The output is in Hz.
  - Total time: This the actual amount of time that it took to run the subvi code in its entirety. The output is in ms.
- 4. Once you know what the inputs and outputs do, it is simply wiring them to run your code appropriately with the 3D tracking code subvi inside it and getting the necessary outputs you need.
- To run a 2D tracking code to find a bead center without any influence from other refractive patterns, simply wire the image in, assuming you are using a camera and bead similar to what I used. If the camera and bead are different, adjust the Sub-ROI width to fit a similar bead area excluding the outer fringes of the airy disc pattern.
  - If you want to slightly decrease calculation time with a minor impact to resolution, change the resolution multiplier to decrease the time to resample the image.
  - If you have refractive patterns influencing the localization of your bead center, implement the Hough transform by wiring a true value to that input. Adjust your detection radius accordingly if using a different bead and camera. Adjust your circular points to a value of your choosing if you like as well.
  - If you need to track in Z, make sure you have already used my Create ZLUT code to create your table, and then open that file with the appropriate code and wire the 2D array from reading that file into the ZLUT of this code. Wire a true value to track Z, and make sure to collect the z positions from the output.
  - Overall, this is a multifunctional code that can be used in many different manners. For an example, look at my Create ZLUT Multiple Beads.vi code. It implements this subvi directly inside of it to create the look up table. Instead of tracking in Z, it simply collects the radial profiles output from the code and applies a piezo positional value to each of the profiles

from an image stack with increasing steps in Z. It is designed to do this for multiple beads, as the beads are not of a truly consistent radius, which is seen in the intensity profiles.

- 5. Most of working with this code is simply understanding the data transfer that is occurring. An image is being input with an intensity array. The intensity is used to find the center of mass, assuming the highest level of intensity correlates to the bead center. The center is used to narrow a window around the initial window for a smaller image that is easy to work with in the autocorrelation algorithm. The smaller image is then upsampled to artificially enhance the image resolution before applying the autocorrelation function. The autocorrelation function is simply the convolution of the upsampled image upon itself, which means a 2D Fast Fourier Transform is applied and multiplied upon itself followed by an inverse 2D Fast Fourier Transform. The intensity maximum of the resulting image correlates to the bead center position, which is found to higher subpixel resolution by a parabolic fit around the maximum point. The maxima locations are output as the XY positions that are then used with the Pythagorean theorem to create the radial profile for Z-axis tracking. Thus, the z-axis accuracy is totally dependent on the accuracy of the transverse localization. This is why it is crucial to find the center accurately, and is why the upsampling was originally implemented.
- 6. Once you have all of the inputs and outputs wired for use and understand the data transfer that is occurring, test your code. Hopefully it will run without issues.
  - If issues occur:
    - There is no output from the tracking code.
      - Check to ensure there is actually a visible image coming into the code by probing the image in input. If there is no image visible in your probe window, then you need to make sure your image type is compatible and that it is being opened properly in your code.
      - If there is an image coming in, you will need to probe more deeply into the code. You will need to check if there is a value coming out of the COM portion. Then check if there is a value coming out of the autocorr portion. If both of these are working properly, then there should be an output coming out. If not, you will have to probe into why either one isn't working.
    - You have data coming out, but it isn't showing up the way you wanted.
      - Double check to make sure that the array is not transposed and giving you the values backwards.
      - Make sure to check that you understood the data flow and what you were getting out of the code.

- Make sure your image is showing up properly in all areas and that the COM is finding the center of the airy disk pattern.
  - Try to localize where the problem might be occurring by creating extra indicators or using probes to find the issue. Almost all issues with data can be found typically by finding where the data is missing.
7. If your code functions without errors/issues, double-check to make sure the data you are getting out is correct and that it is being manipulated or saved in the manner you would like.
8. Make sure to save your code.

**General Notes**

**-This protocol is modified from a protocol generously provided by Dr. Deborah Garrity's lab.**

**-It is important to realize that you are working with a living entity. Thus, care and respect should be afforded to the organism as part of this research study. Please follow a level of ethical standards in your work.**

**-This procedure for breeding should be carried out around 2-3pm 2 days prior to the experimentation day.**

**Zebrafish Breeding:**

- 1. Set up breeding tanks, regular tanks with extra piece for eggs to settle inserted in them, for one female and one male per tank (can do two per tank, assuming you can differentiate sex easily). Place a divider in the tank (this is not always necessary, but was done every time be performed breeding).
- 2. Fill the tanks with appropriate water for the fish, i.e. not tap water.
- 3. Place the male and female fish in the tanks trying to target ones that have not been bred for a week or two. Make sure to use the same genotype/phenotype fish that is appropriate for your experiments. Leave the lids on the tanks where the fish were removed from off to ensure no food is added to them, assuming there are no fish remaining in them.
- 4. Place the lids on the breeding tanks and label them with your initials, the date, the phenotype, and the set number/letter.
- 5. Place the breeding tanks on the shelf for overnight incubation.
- 6. In the morning, approximately 24-28 hours prior to when you would like to run your experiments, remove the dividers to allow the fish to spawn.
- 7. Return later in the morning/afternoon to collect the eggs.
- 8. Fill an empty regular tank with water and remove the two fish to this tank using the liner with holes in it. Do this quickly to minimize the impact to the fish.
- 9. Using a tea strainer, collect the eggs from the original breeding tank by pouring the water with the eggs through the strainer.
- 10. Use a squirt bottle to rinse the embryos into a clean petri dish.
- 11. Label the dish and place aside for incubation until the following morning.
- 12. Put the fish away into the original tanks you removed them from and write the date on that tank. Writing the date prevents them from being used again right away, which will impact breeding potential.
- 13. Clean up all of the tanks that were used and stack in sets of 6 on shelf for later use.
- 14. Put the breeding tank lids away all facing the same direction.

### **Zebrafish Experiments:**

- 1. Return the following morning after embryo collection and transfer the embryos from the dish into a 50 ml conical for transport across campus.
- 2. Transport the embryos across campus and place the conicals in a water bath that has been equilibrated to 30°C for the fish to continue developing. Fish will continue to develop at room temperature, but at a slower pace. The fish can be separated into different conicals and placed at different temperatures to vary the development rate thereby varying the time of circulation onset.
- 3. Near the time 24 hours of when breeding was supposed to have occurred, remove the embryos to the stereomicroscope to check if circulation has started.
- 4. If circulation has started, the embryos will be dechorionated using two sets of tweezers. One will gently hold the embryo while the other is used to “nip” at the outer sack holding embryo. Once a hole is punctured in the sack. The two sets of tweezers are used to gently pull from the sides to completely tear the chorion away releasing the zebrafish embryo.
- 5. Setup of coverglass bottom dish with embryo water containing 2-3 mls 0.2 mg/ml tricaine.
- 6. Using a 1000 µl micropipette with a tip that has had the tip cut off to create a larger hole, pipette up the embryo and place it in the tricaine solution trying to minimize the amount of extra water introduced with the embryo to coverglass bottom dish.
- 7. Place the coverglass bottom dish on the optical tweezers setup.
- 8. Position the dish to where the fish is in the field of view and locate anatomically the position where you would like to measure.
- 9. Ensure that circulation is occurring, and then start the experiments.
- 10. Before turning on the laser, make sure you have on the appropriate glasses to prevent damage to your eyes.
- 11. Turn on the laser and allow it to warm up for a minute.
- 12. Once the laser is warm, start the experiment and turn on the camera. Unblock the beam and record images for the appropriate amount of time.
- 13. Once experiment is complete, block the laser and stop the recording. Make sure to record all of your settings, etc. in your notebook for later use in analysis.
- 14. Following the experimental times, place a solution of beads in the same dish and trap one at approximately the same height you were working in the fish. Record several images of this bead for localization of the trap center.

## APPENDICES A-2.SOFTWARE CODES

---

List of Labview and Matlab Codes:

A-2.1 3D Tracking Subvi

A-2.2 2D Autocorrelation Function Subvi

A-2.3 Compare Z Profile Subvi

A-2.4 Get Max of Autocorrelation Function Subvi

A-2.5 Get Z Index Subvi

A-2.6 Hough Circle Detection Subvi

A-2.7 Get Radial Z Profile Subvi

A-2.8 Create ZLUT VI

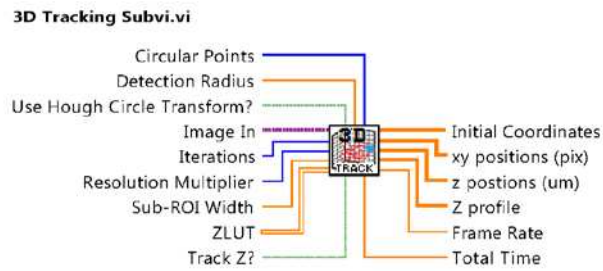
A-2.9 Smoluchowski Plot Creator VI

A-2.10 ST Plot Creator VI

A-2.11 ST Plot Overlay Lines on Image Subvi

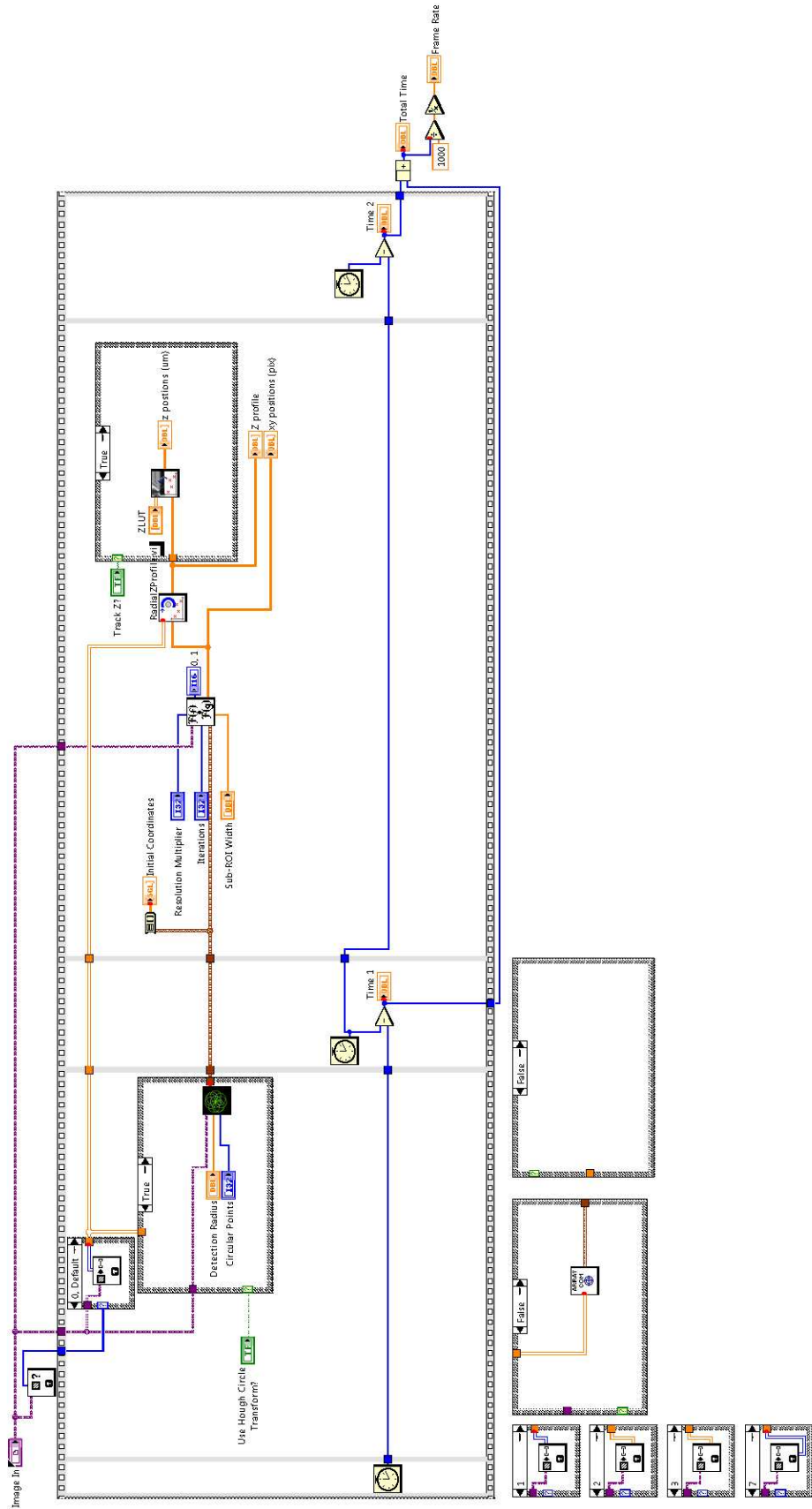
A-2.12 Efficient Subpixel Registration in 1-Dimension M File

## APPENDIX A-2.1 3D TRACKING SUBVI



Input Values	Output Values
<p><b>Image In</b></p> <p>Image In: <input type="text"/></p> <p>Iterations: <input type="text" value="1"/></p> <p>Resolution Multiplier: <input type="text" value="7"/></p> <p>Sub-ROI Width: <input type="text" value="76"/></p> <p><b>Hough Transform Inputs</b></p> <p>Use Hough Circle Transform?: <input checked="" type="checkbox"/></p> <p>Detection Radius: <input type="text" value="7"/></p> <p>Circular Points: <input type="text" value="360"/></p> <p><b>Z-Axis Tracking Inputs</b></p> <p>Track Z?: <input checked="" type="checkbox"/></p> <p>ZLUT: <input type="text" value="0"/></p>	<p><b>Tracked Data Outputs</b></p> <p>Initial Coordinates: <input type="text" value="0"/></p> <p>xy positions (pix): <input type="text" value="1"/></p> <p>z positions (um): <input type="text" value="0"/></p> <p>Z profile: <input type="text" value="255.00"/></p> <p><b>Timing Data Outputs</b></p> <p>Time 1: <input type="text" value="0"/></p> <p>Time 2: <input type="text" value="0"/></p> <p>Total Time: <input type="text" value="0"/></p> <p>Frame Rate: <input type="text" value="0"/></p>

This code is designed to take an input image, or a ROI (region of interest) of an image and perform multiple steps of a tracking algorithm. The code is designed to find the center of a bead refraction pattern with an initial center of mass (COM) followed by a 2D autocorrelation function on an unsampled sub-region of the initial image. The center of mass is either found by a median subtracted center of mass/intensity function or a Hough Circle Transform designed to find radial circles in an image. The Hough Transform is beneficial to images where the bead refraction pattern is imaged upon by other objects, such as cells. The 2D autocorrelation produces an output of highest probability of center location of the bead. This output is used to optionally track along the z-axis by creating a radial/polar profile of the initial image/ROI. This radial profile is then compared by a least squares regression algorithm against a z-axis Look Up Table (ZLUT) to find the most probable location of intersection with the axial pattern with a known locational value. Overall, this code provides a means of both 2D and 3D tracking of bead intensity patterns in the presence or absence of infringing objects. Note: The ZLUT is a 3D array input from another file. This array consists of an array of 2D radial bead intensity patterns across multiple beads at multiple z-axis values. This is done to provide a fit to multiple radial patterns that will represent the distribution of bead radii, which will more likely find a bead of common radius for accuracy in tracking.



## APPENDIX A-2.2 2D AUTOCORRELATION FUNCTION SUBVI

---

### 2D Autocorrelation v2.vi

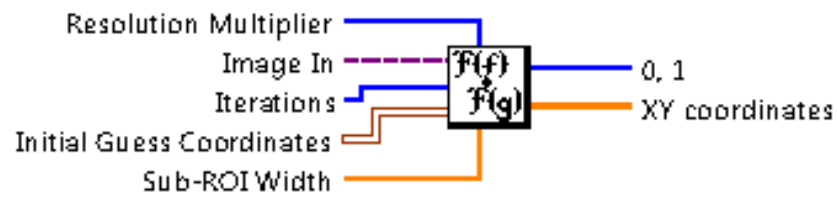


Image In

Initial Guess Coordinates

X Centroid  
0

Y Centroid  
0

Iterations  
1

Resolution Multiplier  
7

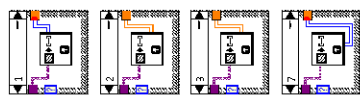
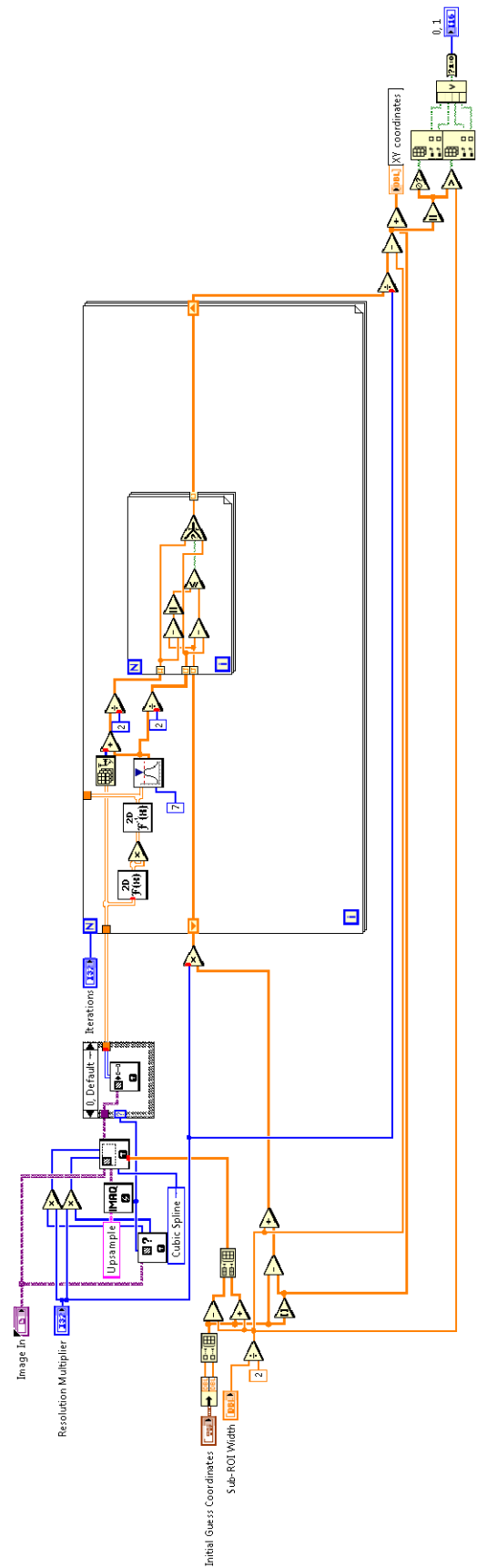
Sub-ROI Width  
76

XY coordinates

0.000  
0.000

0, 1  
0

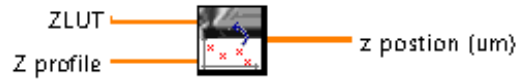
This code performs a 2D autocorrelation on an input image. The image input is upsampled within a square region of the user defined size (Sub-ROI Width). The upsampled image is converted to an array that is run through the 2D autocorrelation a user defined number of times (Iterations). The autocorrelation is a 2D cross-correlation, i.e. multiplication in the frequency domain after a Fast Fourier Transform (FFT) followed by an Inverse FFT and a fit to find the max intensity value correlating to the highest likelihood position of the center of the intensity distribution. This position is then output in the form of XY coordinates. Note: This code is designed to find the center position of an intensity distribution created by an imaged bead.



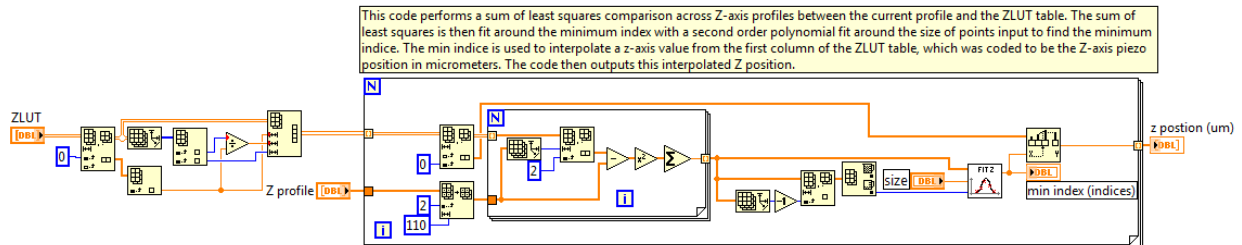
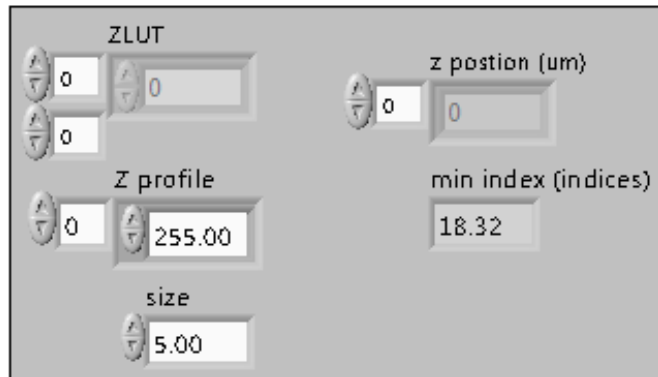
## APPENDIX A-2.3 COMPARE Z PROFILE SUBVI

Connector Pane

**CompareZProfile2-BWS v4.vi**



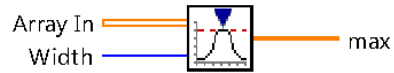
Front Panel



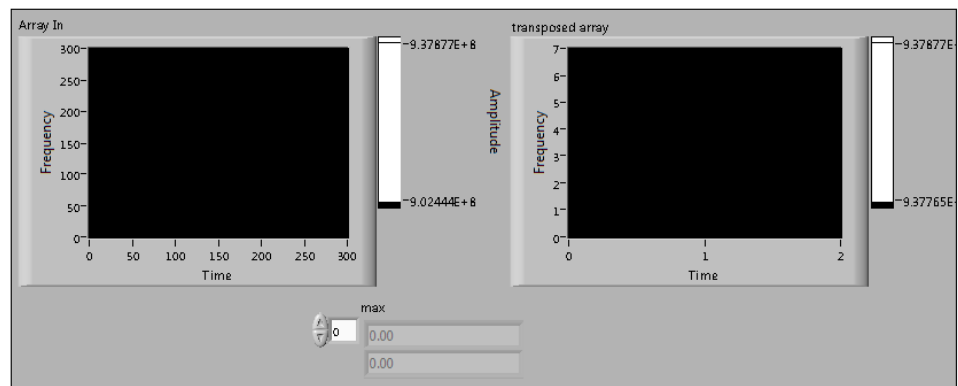
## APPENDIX A-2.4 GET MAX OF AUTOCORRELATION FUNCTION SUBVI

Connector Pane

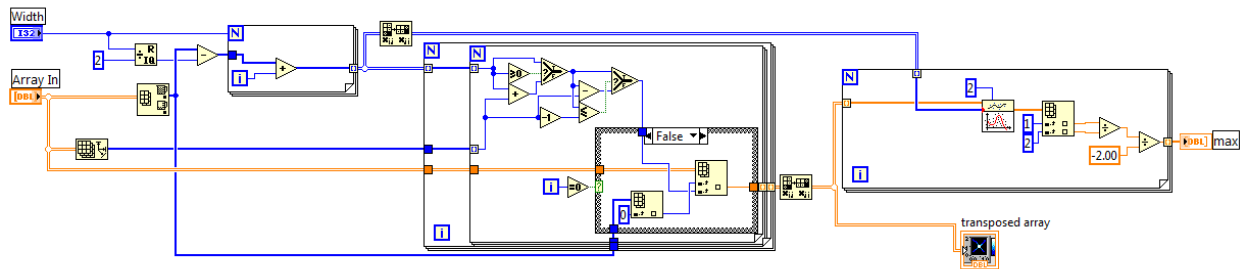
**Get Max of Autocorr.vi**



Front Panel



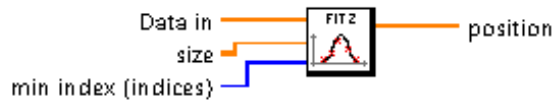
This code performs a polynomial fit to a certain width around a maximum intensity value to find the maximum position with subpixel accuracy.



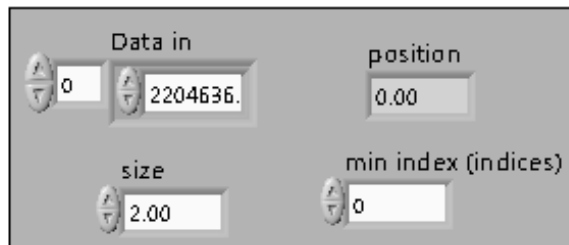
## APPENDIX A-2.5 GET Z INDEX SUBVI

Connector Pane

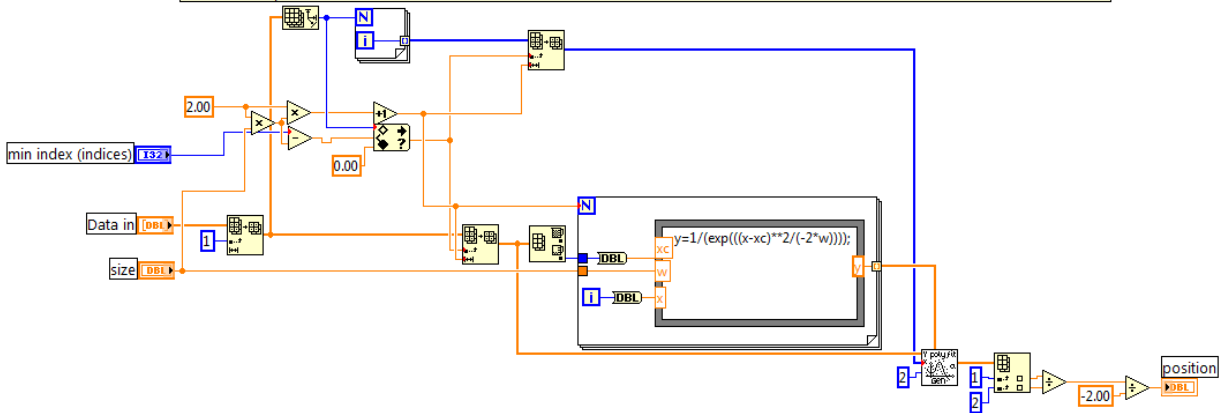
**Get Z Polyn fit-BWS.vi**



Front Panel



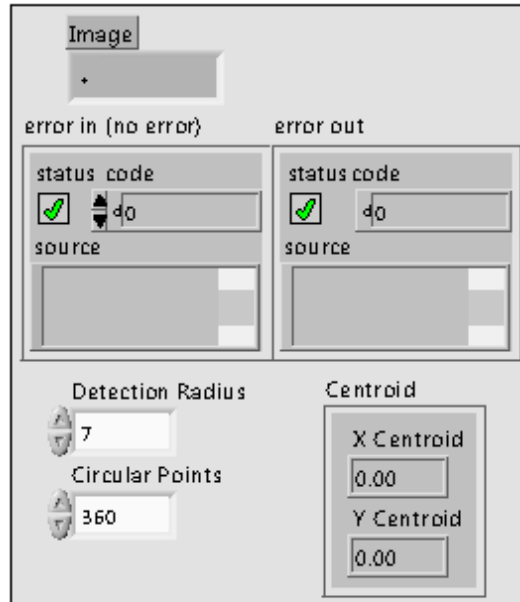
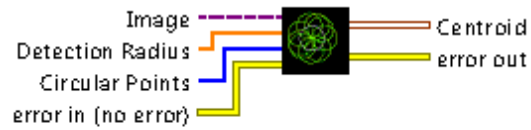
This code inputs an array of sum of least squares values along with the minimum indice. The min indice is then used as the value at the center of the fit. The size of the fit is used to create a profile of y values produced from a gaussian equation with the width of the gaussian correlating to the size input. This profile of y values is used as the standard deviation for the polynomial fit. The polynomial fit uses an array of x values and a subset of the sum of least squares data in to produce a fit with known coefficient values. The coefficient values are then used to calculate the positional index within the array that is then output.



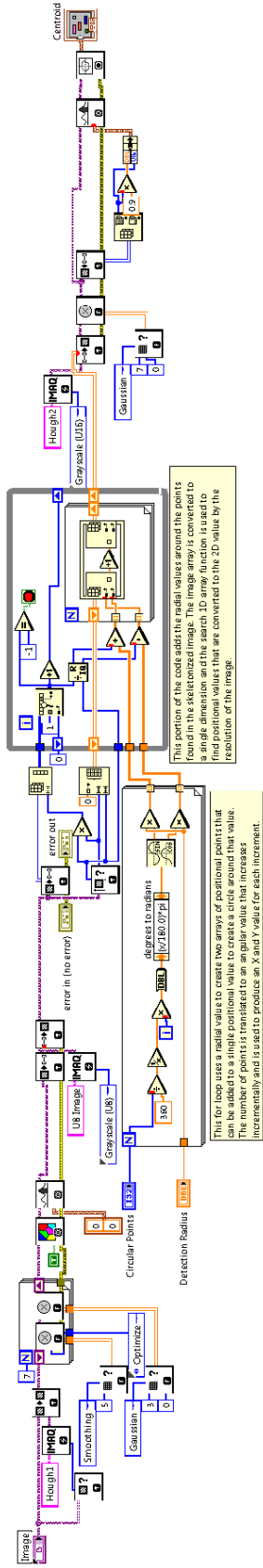
## APPENDIX A-2.6 HOUGH CIRCLE DETECTION SUBVI

---

### Hough Circle Detection Stand-alone.vi



This code is designed to find circular patterns within an image. The input image is initially smoothed and gaussian blurred to eliminate minor pixel differences that will create more sections within a watershed that follows. The watershed is thresholded to produce a skeletonized binary image of just the watershed boundaries. This image is then put through the Hough Circle Transform that draws a single circle containing a user defined number of points (Detection Radius) around each boundary point that equals 1. The transform adds a value of 1 to each point that a circle hits, which will create an intensity distribution created from the circles overlapping. If a circle of the appropriate radius is found, it will create a higher intensity point correlating to the center of that circle. The output array from the Hough Transform is converted to an image that is gaussian blurred to smooth the image slightly. The image is then thresholded to find the values within the top 10% of the maximum value. This theoretically should contain only the points within a round circle. This thresholded image is subjected to find the center of mass (centroid) that correlates to the center of the circle.



## APPENDIX A-2.7 GET RADIAL Z PROFILE SUBVI

---

Connector Pane

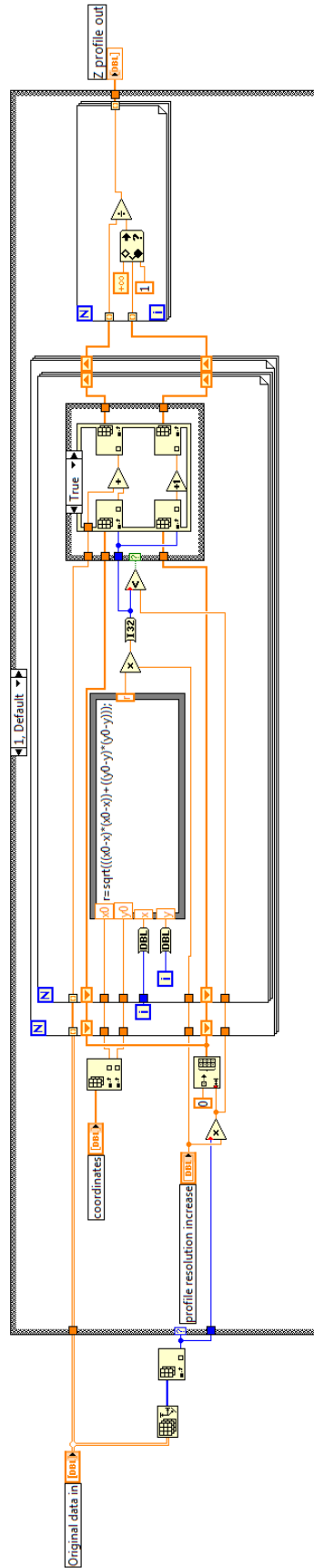
### RadialZProfile.vi



Front Panel

Original data in			Z profile out	
0	126	120	0	255.00
0	121	126		182.83
	124	122		76.92
	124	122		34.20
	coordinates			30.59
0	31.91			33.03
	34.51			37.89
	0.00			46.86
	profile resolution increase			59.21
	1			81.46

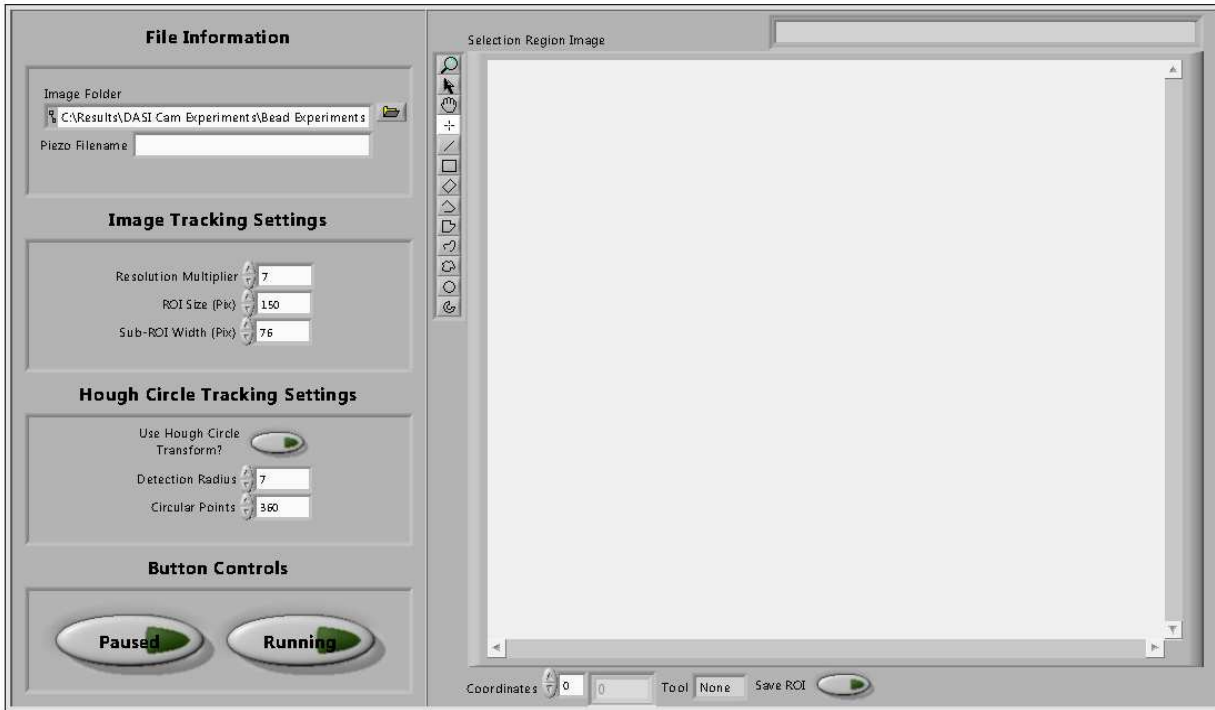
This code is designed to create a radial profile outward from a single point. The code inputs an array of image pixel data along with the center coordinates found from a cross-correlation algorithm. The code then iteratively goes through each pixel location in the image array, assigning a radial value to each pixel location. This intensity is added to the radial location in a 1D array. After adding intensity values from each radial location, each location is divided by the number of pixel counts that were added to that location to get an average radial intensity at that location. This is output as the Z profile in the end.

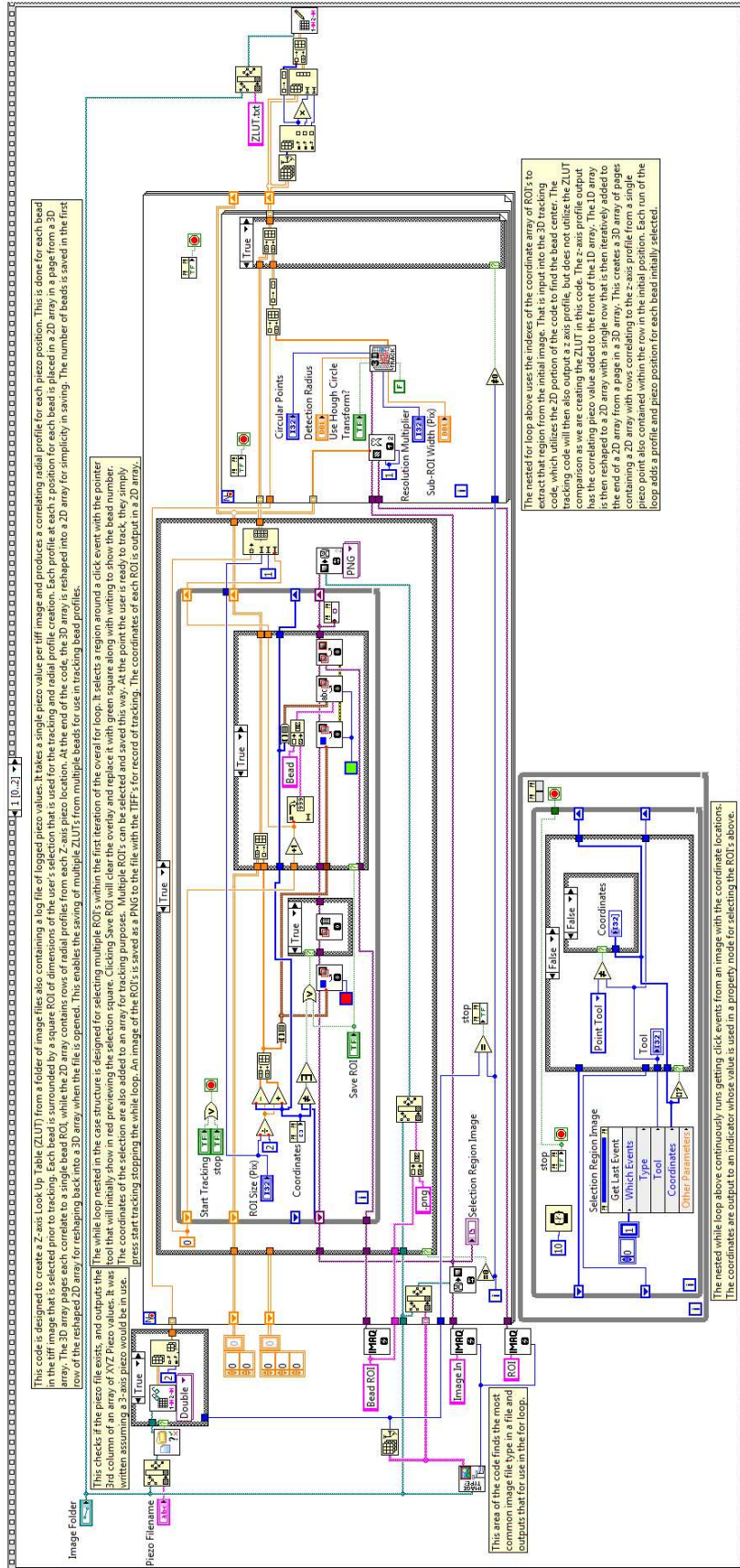


## APPENDIX A-2.8 CREATE ZLUT VI

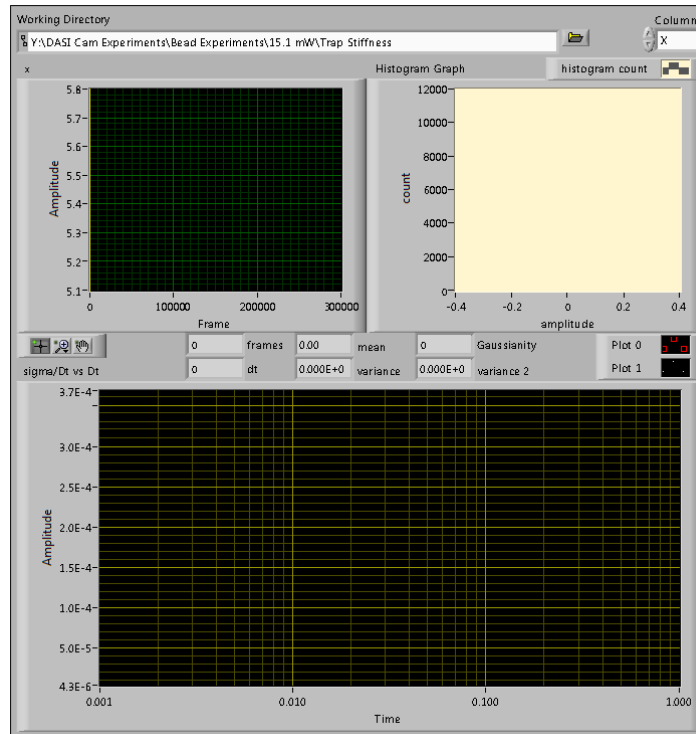
---

### Create ZLUT Multiple Beads.vi

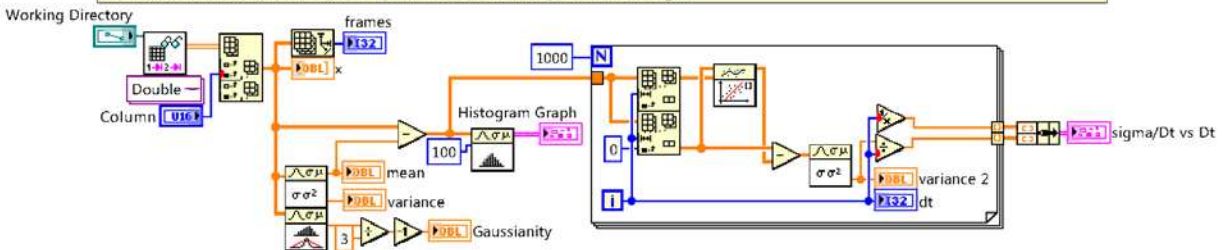




## APPENDIX A-2.9 SMOLUCHOWSKI PLOT CREATOR VI



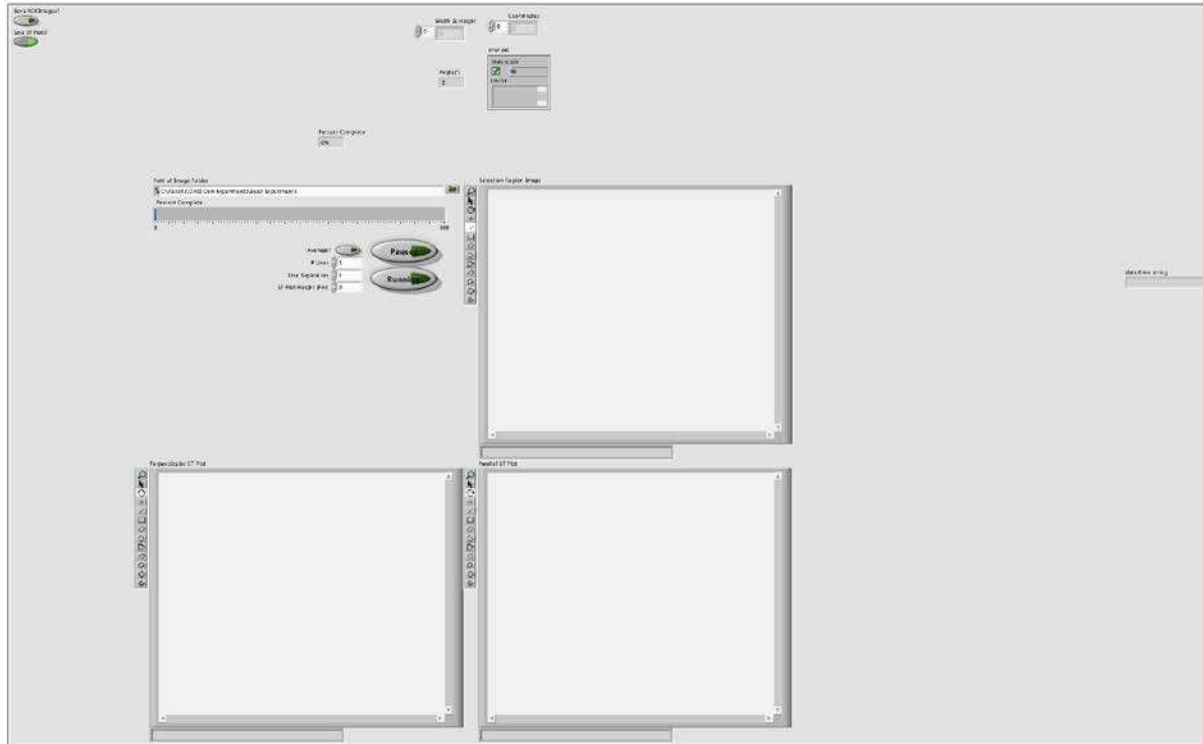
This code inputs a tracking data file consisting of XY values. The column to use is selected initial, and the Smoluchowski formalism is run off of that column of particle displacements. It uses a sliding window algorithm to subtract all values  $x$  from  $x+dt$  for all of the collected data as  $dt$  grows. It then creates a distribution of these subtracted values and calculates the variance of this distribution. The variance is normalized to the time window ( $dt$ ), or the frequency ( $1/dt$ ), and plotted against that frequency. This provides the distribution discussed in Lindner, M. Nir, G., Vivante, A., Young, I. T. & Garini, Y. Dynamic analysis of a diffusing particle in a trapping potential. Phys. Rev. E 87, 022716 (2013). This data can be saved and then is fit to find the trap stiffness and diffusion parameters in Origin.



# APPENDIX A-2.10 ST PLOT CREATOR VI

---

## ST Plot Creator v5.vi

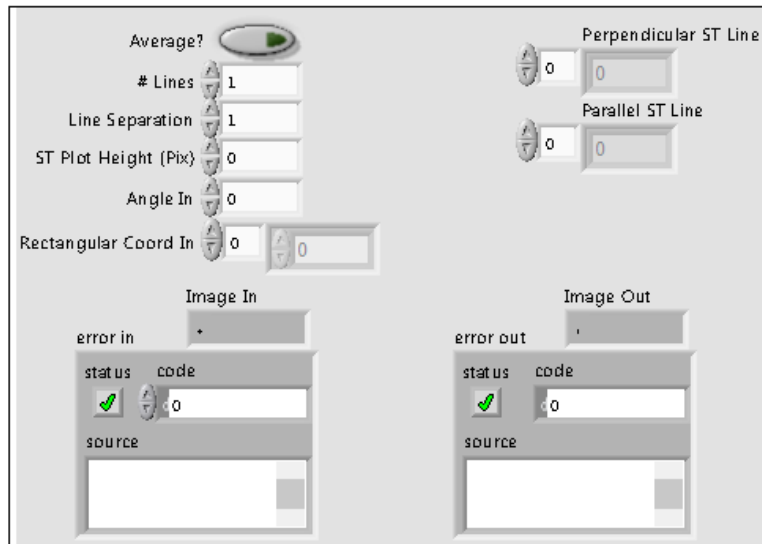
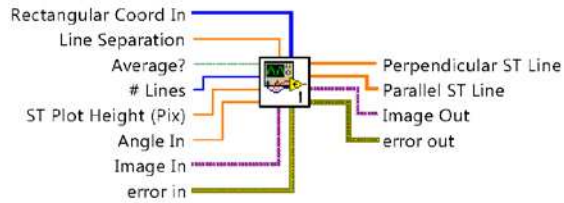




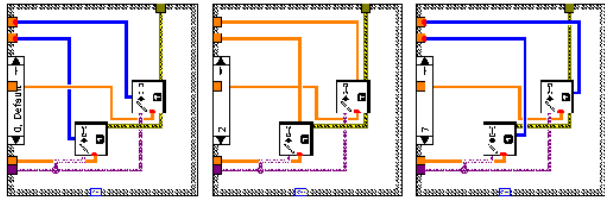
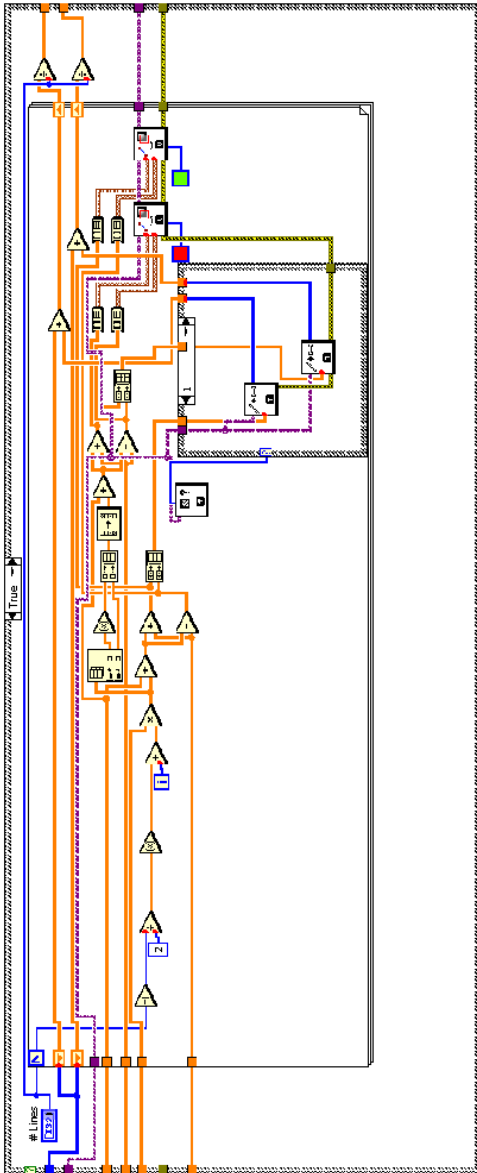
## APPENDIX A-2.11 ST PLOT OVERLAY LINES ON IMAGE SUBVI

---

**ST Plot Line Overlay Subvi.vi**







## APPENDIX A-2.12 REGISTRATION IN 1-DIMENSION M FILE

---

10/31/18 10:24 PM ...\\efficient\_subpixel\_registration\_1d.m 1 of 1

---

```
%% Efficient subpixel image registration 1D by cross-correlation.
% Registers single pixels lines (1-D rigid translation) within a fraction
% of a pixel specified by the user. Instead of computing a zero-padded FFT
% (fast Fourier transform), this code uses selective upsampling by a
% matrix-multiply DFT (discrete FT) to dramatically reduce computation time
% and memory without sacrificing accuracy. With this procedure all the
% image points are used to compute the upsampled cross-correlation in a
% very small neighborhood around its peak. This algorithm is referred to as
% the single-step DFT algorithm in [1].
%
% This code was modified from:
% [1] Manuel Guizar-Sicairos, Samuel T. Thurman, and James R. Fienup,
% "Efficient subpixel image registration algorithms," Opt. Lett. 33,
% 156-158 (2008).

% Note: This code was modified to use the existing code in
% dftregistration.m, no changes were made to any of the codes called in
% this code.

%% Obtain array of shift values from a 1D image kymograph.
% Select the filename of your kymograph and paste that into filename.
% The code compares the first column of pixels in the image against all
% other columns of pixels in the image and outputs the shift. The output is
% written to the same filename that has stripped the tif ending and
% replaced it with a txt file.
filename='filename.tif';
f = im2double(imread(filename));
[r,c]=size(f);
output=zeros(c,1);
h=waitbar(0,'1','Name','Running Image Registration Algorithm...');
for i=1:c;
    [outputa Greg] = dftregistration(fft(f(:,1)),fft(f(:,i)),1000);
    output(i)=outputa(3);
    waitbar(i/c,h,sprintf('%0.2f%%',round(i/c*100,2)))
end
filename2=strrep(filename, '.tif', '.txt');
dlmwrite(filename2,output,'\t');
plot (output)
```